POLITECNICO
MILANO 1863

Scuola di Ingegneria Industriale e dell'Informazione
Dipartimento di Energia

Master's Thesis in Chemical Engineering

New Insights on Pt Promotion of Co/γ-Al_2O_3 Catalysts for Fischer-Tropsch Synthesis

Supervisor: Prof. Luca **LIETTI**

Co-supervisors: Dott. Ing. Carlo Giorgio **VISCONTI**, Ph.D.
Dott. Ing. Laura **FRATALOCCHI**

Federico **SALZANI** matr. 837203

Pietro **SAVARE'** matr. 837188

Academic Year 2015-2016

«O ben finiti, o già spiriti eletti»,
Virgilio incominciò, «per quella pace
ch'i credo che per voi tutti s'aspetti,

ditene dove la montagna giace
sì che possibil sia l'andare in suso;
ché perder tempo a chi più sa più spiace».

Dante Alighieri, Purgatorio (III, 71-78)

Index

Abstract

In the last decade until the oil crisis of 2014, industries' interest in *Gas-to-Liquids* (GTL), *Coal-to-Liquids* (CTL) and *Biomass-to-Liquids* (BTL), capable of converting natural gas, coal and biomass into liquid fuels had grown considerably in a scenario which, due to a constant growth in energy demand, was experiencing a reduction in the availability of low price crude oil. At that time, XTL (*X-to-Liquids*, general acronym for these processes) technologies represented valid economic alternatives for fuels production, as they could exploit relatively cheap and widely available resources. The significant advantage offered by such processes is the manufacture of higher added value and performance products, with lower environmental impact compared to equivalent standards.

XTL technologies obey on the following fundamental steps:

1. Production of the syngas mixture, consisting of CO and H2, from the raw materials by consolidated processes such as gasification and *Steam Methane Reforming* (SMR).
2. Syngas conversion into liquid hydrocarbons at high molecular weight using Fischer-Tropsch synthesis (FTS).
3. Product upgrading, via standard refining processes, to obtain gasoline and diesel.

Conventional GTL plants are designed on a large scale, as they run Fischer-Tropsch synthesis within large fixed bed or slurry reactors. Therefore, these solutions are only suitable for processing huge quantities of raw materials.

Industries' interest in exploiting smaller and remote reservoirs, continuously growing in number in the recent years, has led to researching for reduced size of equipment, which can easily be transported on-site (*CompactGTL* technologies).

In the last three years, the LCCP (*Laboratory of Catalysis and Catalytic Processes*) group at *Politecnico di Milano* has studied these technologies, focusing on the development of innovative cobalt-based catalysts, capable of reaching high CO conversion and high selectivity towards desired Fischer-Tropsch products.

In this thesis attention has been given principally to performance improvement of such catalysts. To achieve this goal, the effect of a small addition of platinum, acknowledged promoter in the FT research, although very expensive, was thoroughly studied. Also, with the same objective unconventional catalysts were investigated: the latter are different from the conventional due to the

addition of an organic compound, namely diethylene glycol (DEG), in the usual impregnating solution of cobalt-nitrate salts which contain the active phase.

Further target was to demonstrate the validity of catalyst testing run at atmospheric pressure against that run at industrially relevant Fischer-Tropsch conditions (high pressure). While low pressure testing on conventional catalysts was valid, for the unconventional, discrepancies were observed between the results of the two tests.

Outline

This thesis is divided into 5 chapters:

1. ***Energy Scenario and Fischer-Tropsch Synthesis***. A brief overview of the world energy scenario and a report on the evolution in the years of the Fischer-Tropsch process are hereby reported.
2. ***State of the Art of Co/γ-alumina Catalysts***. This section provides an outline of the conventional and novel (compact) technologies. In particular, attention has been given principally to the main features that are necessary for the formulation of highly active catalysts for small scale applications.
3. ***Lab Scale Rig and Experimental Procedures***. In this chapter the lab scale rig employed for low pressure experiments is fully described. The procedures for catalyst characterization (BET, ICP-MS, XRD, TPR) and testing are reported later.
4. ***Influence of Pt Deposition Order on Conventional Co/γ-alumina Catalysts***. The effect of Pt deposition order is investigated on conventional catalysts at different cobalt loadings, both in terms of catalyst characterization and low pressure testing.
5. ***Unconventional Co/Pt/γ-alumina Catalysts: Characterization, Performances and Validity of Low-Pressure Screening Tests***. The effect of DEG addition to the impregnating solution is described in terms of catalyst characterization and testing. Furthermore, the effect of Pt deposition order on such unconventional catalysts is investigated. Finally, the reported performances on the low pressure rig for the investigated catalysts are compared to those observed at industrially relevant Fischer-Tropsch conditions.

Chapter 1 – Energy Scenario and Fischer-Tropsch Synthesis

1.1 Energy scenario

Up to the last decades of the XIX century, coal used to be the most important worldwide source of energy. It was used for both domestic and industrial purposes and as a fuel for the civil and military industry.

From the beginning of the XX century, oil has gradually replaced coal as the primary source of energy. Expansion and development in the transportation sector combined with industrial growth and increasing urbanization have created the need for an energy source characterized by a high specific energy content and a better environmental compatibility with respect to coal: liquid fuels. Today approximately 85% of the energy demand still comes from fossil fuels.

Due to multiple factors such as technological progress, population growth and middle class expansion, energy demand is expected to significantly increase in the coming years thus creating issues related to sources, efficiency and delivery of energy. Furthermore, this century has seen tremendous advances in energy technology, including those that unlocked North America's vast resources of unconventional oil and gas, thereby ushering an era of energy abundance and diversity. Along with these matters, other issues regard the environmental problems, with CO_2 emissions that will probably peak around 2030.

Therefore, additional energy provision and delivery in a global market with both economic and environmental sustainability is going to be one of the most crucial challenges of this century; since scientific development and technological skills as well as social and political matters play a crucial role, this challenge becomes a matter of interest for everyone on the planet.

1.1.1 Energy outlook to 2040

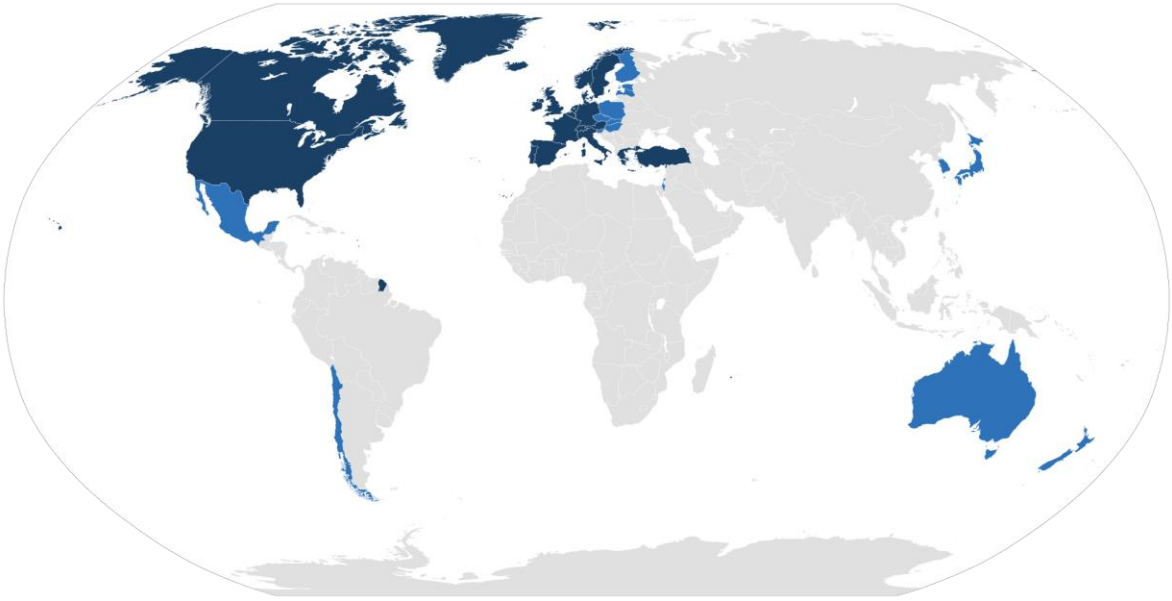

Figure 1.1: List of OEDC countries (blue: founding member countries, 1961; light blue: other member countries) [1]

In order to have better knowledge of the energy challenge, it is essential to understand ongoing scenarios and to predict, as closely as possible, future trends with an outlook on the next decades.

The period going from now to 2040 is expected to reflect a dramatic expansion of the world's population and the global middle class. Improvement in living conditions will give millions of people access to electricity and global demand is expected to rise by 25%: an equivalent increase to the total energy used in North America and Latin America today. It would have been far higher (exceeding 110%) if we had not foreseen significant improvements in energy efficiency across all sectors. Demand growth is expected to increase by 45 % in non-OECD (*Office of Economic Cooperation and Development*) countries while that in OECD countries will remain flat. As growth is strongly asymmetric, it implies considerable changes in market structure as well as in international policies.

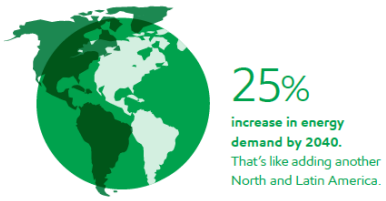

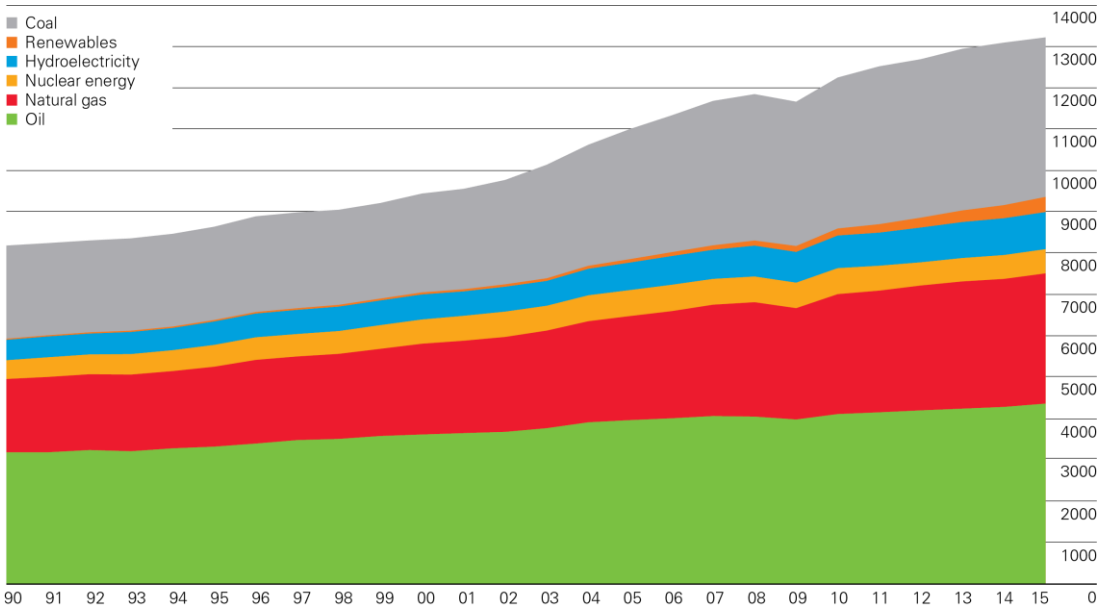

Figure 1.2: Primary energy world consumption 2015 (Million tonnes oil equivalent) [2]

By 2040 world population is expected to increase up to 9 billion (a 1.8 billion increase as compared to today's figures) and global GDP (*Gross Domestic Product*) more than double. Furthermore, in most regions, those aged under-14 will decrease in number due to declining birth rates and the over-65 population will increase, due to a rise in life expectancy. To keep pace with demand, the world will need to pursue all economic energy sources due to new technologies that will require policies to promote innovation, investment and free commerce.

The most important sectors in terms of energy demand are transportation, residential/commercial and industrial. Global energy demand for transportation is forecast to increase by about 30% from 2014 to 2040, essentially due to the contribution of non-OECD countries. Nowadays, there are about 1 billion *light-duty vehicles* (LDV) in the world, expected to rise to 1.8 billion in the next 25 years, with about 90% of this growth outside the 32 OECD countries. As a result of improved fuel economy, the energy demand for LDVs is expected to peak around 2020 and then decline to nearly 10% in the following 20 years along with the increase of hybrid car market share.

Even with an increase in efficiency, combined demand of residential and commercial energy is expected to rise by nearly 25% from 2014 to 2040. A high rise of households in Asia and other developing regions will drive such demand and, as incomes increase, so will the purchase of appliances and air conditioners. For instance, while in 1985 one out of fifty Chinese homes had refrigerators, today more than 80% do.

Globally, industrial activity accounts for 30% of primary energy and 50% of electricity demand and it is forecast to rise mostly in two sectors: heavy industry and chemicals, due to rising standards in developing countries. In particular, the production of chemicals is the fastest growing use of energy in the industrial sector.

1.1.2 Fulfilling the need for future supplies

Oil, natural gas and coal are expected to cover almost 80% of the world's energy demand throughout the next 25 years due to their reliability, affordability, versatility, transportability and capability of providing a lot of energy within a relatively low volume. Among them, oil will remain the most used fuel with gas moving into second place ahead of coal.

The latter, currently the second-largest fossil fuel resource, is expected to see global demand peak around 2025 and then begin to decline, owing to improved energy efficiency and environmental sustainability in the power generation sector and a switch to fuels with lower CO_2 emissions. By 2040, coal will account for 20% of the global energy demand, down from about 25% in 2014. Natural gas, on the other hand, is expected to rise to 50% and meet around 40% of the global demand in the same period.

Nuclear energy is a pillar of the electricity production in many countries and accounts for about 10% of today's world electricity. As nuclear plants provide electricity with low CO_2 emissions and expanding nuclear capacity would enable nations to diversify their energy supplies, the nuclear sector will see strong gains in the coming decades. The figures have more than doubled since 2014 with China accounting for nearly half of this growth.

Modern renewable energy sources - wind, solar and biofuels – are also growing rapidly and will more than triple from now to 2040. The largest volume growth will come from wind, which by 2040 is expected to supply about 2% of the world's energy and around 10% of electricity. Together nuclear and renewables are likely to account for almost 40% of the growth in the global energy demand up to 2025.

In addition to expanding its supplies, the world is also continuing to enhance its ability of trading energy among different regions. Much of this growth is related to the expanding global LNG (*Liquefied Natural Gas*) network - the liquefaction plants, tankers and re-gasification terminals which enable abundant natural gas to reach markets around the world.

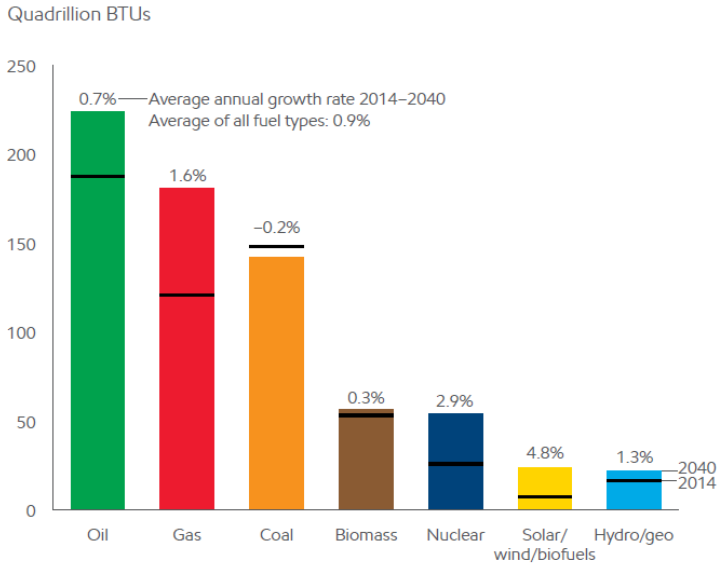

Figure 1.3: Projections of global duel demand in 2040 [3]

Liquids

Global liquid output is seen as rising to 112 MBD (*Million Barrels per Day*) in 2040, up from 93 MBD in 2014. Most of the growth is expected to come from technology-driven supplies including tight oil, *Natural Gas Liquids* (NGL), oil sands and deep-water production, reaching 40% of global liquid supply up from 25% today. Despite a decade ago tight oil, dispersed in shale and other tight rock formation, was barely seen on the radar screen, it will probably account for 10% of the world's liquid production by 2040. Most of this oil will come from North America, the birthplace of the tight oil industry, where crude output has risen by about 75% since then and in 2014 tight liquid production overcame the total production of any other OPEC country except Saudi Arabia. The past few years have seen considerable improvement in the performance of tight oil wells and drilling efficiency; tight oil is now an established and globally competitive source of liquid fuels. Unlike some conventional or more complex projects, its production can also adjust relatively quickly to changes in demand. The spread of this new technology did and will change the role of North America, once a massive importer and great exporter in few years.

By 2040, the number of resources yet to be exploited will still be far higher than the total demand before 2040, even if this rises more than 20%.

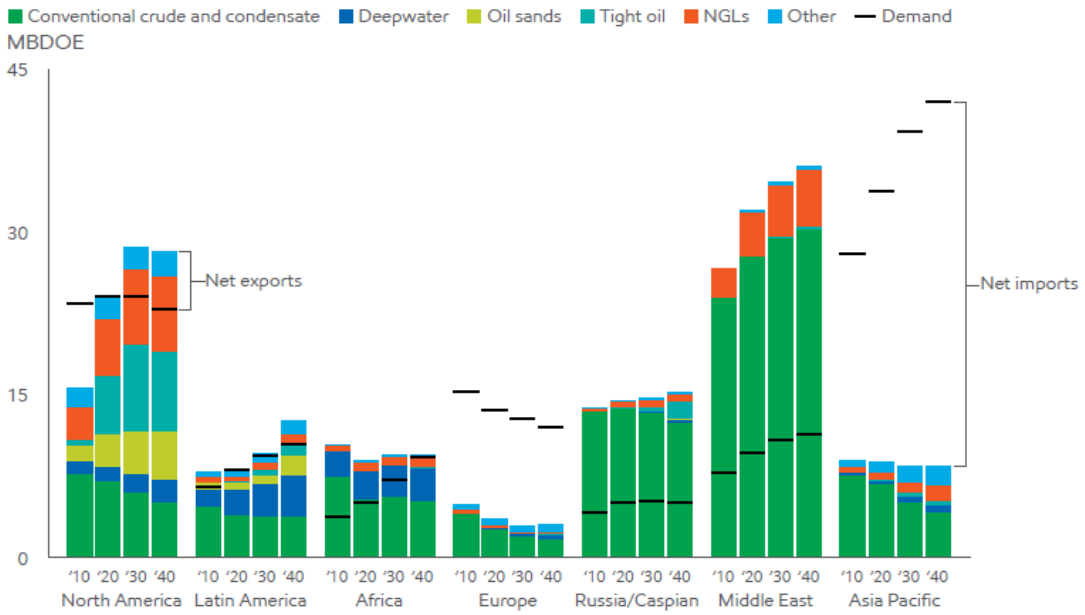

Figure 1.4: Liquid trade balance by region [3]

Natural Gas

Global demand for natural gas (NG) is seen as rising by 50% in the next 25 years, faster than any other fossil fuels. The most important reasons are versatility, reduced environmental impact and geographically scattered reservoirs. Natural gas can run generators to produce electricity or it can be directly used in homes, offices and factories simply as a fuel; its very low carbon content makes it an effective and proven tool for curbing CO_2 emissions, particularly in the electricity generation sector. It emits up to 60% less CO_2 than coal and is geographically diverse: North America, Latin America, Russia/Caspian, Asia Pacific, the Middle East and Africa each hold 10% or more of the resources.

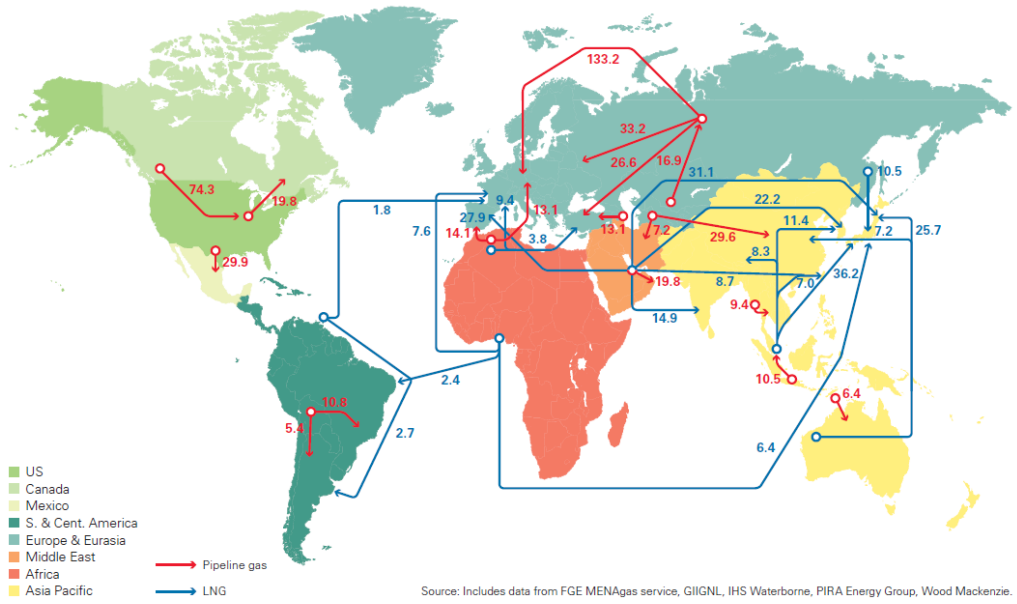

Figure 1.5: Natural gas trade movements 2015 – trade flows worldwide in billion cubic meters [2]

Nearly half of the growth in global gas demand through 2040 is expected to be met through inter-regional trade, most using LNG (*Liquefied Natural Gas*) technology. Until the first LNG shipping and receiving terminals opened in 1964, inter-regional gas trading was confined to areas connected by pipeline. With LNG technology, natural gas can be super-cooled to liquid and safely shipped via tanker to receiving terminals anywhere in the world. LNG exports are expected to triple in the next years and most of which will go to competitive markets in Asia Pacific, followed by United States, East Africa and Australia.

Today, around 70% of NG consumption is delivered through pipelines operating at pressures around 80 [MPa] and flow rates of 10^6 [$Nm^3\ h^{-1}$]; shipping becomes convenient when distances make the pipeline costs higher than that of liquefaction, transportation and regasification.

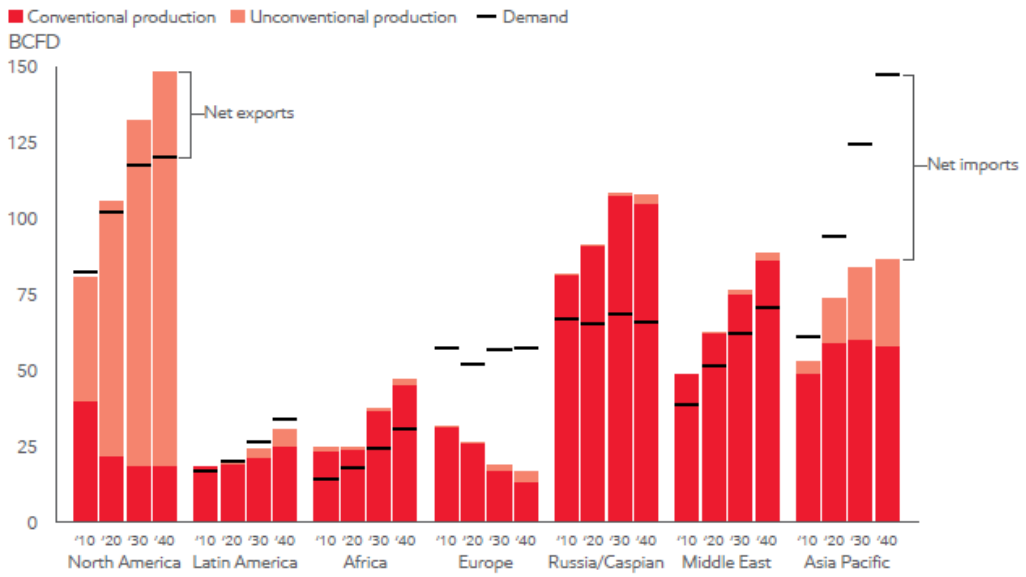

Figure 1.6: Gas trade balance by region [3]

One further solution to the problem of complete exploitation of NG resources and related transportation is the so-called GTL (*Gas-to-Liquids*) technology. Particularly suitable for small gas reserves, GTL consists of a chemical liquefaction of natural gas which significantly upgrades the economic value of the latter and eases its access to the transportation fuels market. Additionally, it could mitigate some environmental concerns by displacing higher-sulfur fuels, obtained from crude oil, with essentially sulfur-free fuels. Additionally, GTL technology could allow refineries to convert some of their gaseous waste products (*flare gas*) into valuable transportation fuels and lubricants.

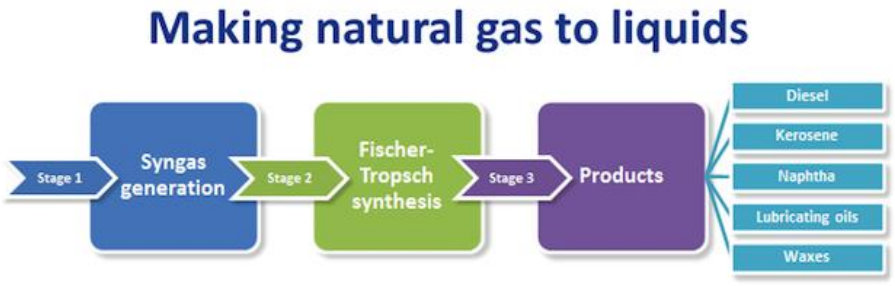

Figure 1.7: Flow scheme of the GTL technology [4]

Three are the fundamental steps that make up the GTL technology. First natural gas is catalytically converted into a mixture of carbon monoxide and hydrogen, known as *syngas*, via processes as

Partial Oxidation (POX), *Autothermal Reforming* (ATR) or *Steam Methane Reforming* (SMR). Syngas is then converted, in a catalytic reactor, into a mixture of valuable hydrocarbon products. The last stage is cracking or isomerization, which "tailors" the molecule chain into products with desired properties.

Depending on the reaction involved in the second step, four main families can be accounted under the name of GTL technologies:

a. *Gas to Methanol*
b. *Gas to Olefins*
c. *Gas to Dimethyl-Ether (DME)*
d. *Gas to Hydrocarbons*

Fischer-Tropsch synthesis is the core of the Gas to Hydrocarbon technology.

1.2 Fischer-Tropsch synthesis

Fischer-Tropsch synthesis (FTS) is one of the most important and complex processes in the chemical industry. This technology allows indirect liquefaction of carbon sources as coal, natural gas and biomass via syngas production and it is mainly used to synthetize clean (sulfur-free) diesels with high-cetane number (NC_{FTS} = 75 vs NC_{STD} = 50).

It consists of a catalytic reaction between H_2 and CO (*syngas*) giving liquid long chain hydrocarbons. The general stoichiometry is the following:

$$nCO + 2nH_2 \rightarrow (-CH_2) + nH_2O \qquad (1.1)$$

Main products are n-paraffins in a range between C_1 and C_{60+} (waxes) and n-olefins. The product mixture is triphasic at ambient temperature as it consists of light gases, liquid hydrocarbons and waxes.

1.2.1 History

The first decades of the XX century have seen the transition from coal to oil as primary source of energy for the global energy market. Both the development in the transportation sector and the industrial growth has led to the need of cheap, easy transportable and high density source of energy. In such environment, especially in countries rich in coal fields as Germany, the interest for the production of liquid synthetic fuels started to grow. Amongst many routes proposed to achieve this goal, the most important ones are ascribed to three German scientists: Friedrich Bergius (Nobel Prize in Chemistry, 1931), Franz Fischer and Hans Tropsch. The first one found a way for the liquefaction of coal via hydrogenation at high pressures. A couple of years later Bergius himself, together with Fischer and Tropsch, used coal to produce a mixture of hydrocarbons [5].

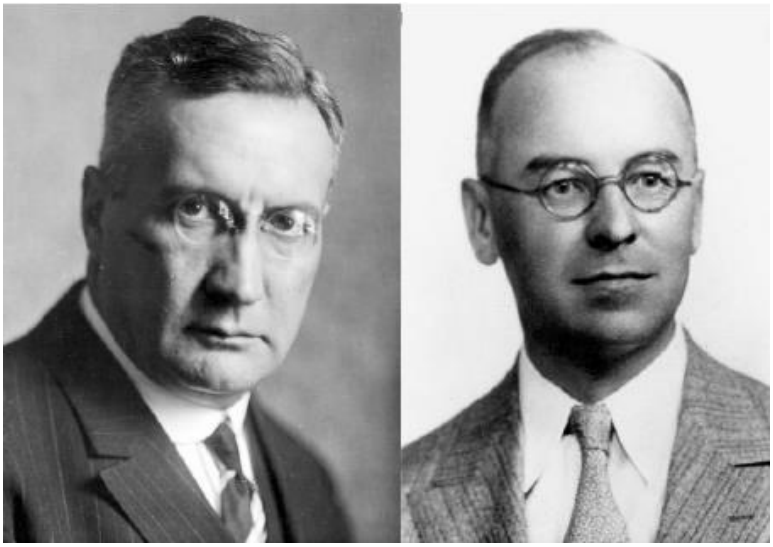

Figure 1.8: Franz Fischer (left) and Hans Tropsch (right) [6]

Production of liquid hydrocarbons over a cobalt catalyst was first reported in 1913 on a patent granted to *BASF*, related to a catalytic hydrogenation of CO at 300-400 [°C] and 120 [atm] with ceria-, cobalt-, molybdenum-based catalysts giving a mixture of hydrocarbons, alcohols, chetons and acids. During the following years, until *World War I* (WWI), many studies had been performed on reduction of CO in an iron based catalytic environment at high temperatures (400-450 [°C]) and pressures (100-150 [atm]).

With the goal of increasing the alkane content, Fischer and Tropsch observed that oxygenated product fraction could have been lowered by performing the reaction at lower pressures, around 7 [atm]. In the attempt of solving the problem of decreasing catalytic activity at lower pressures, the two German scientists developed a new cobalt-iron catalyst; this first way of obtaining a mixture with high hydrocarbon content led to the origin of the Fischer-Tropsch Synthesis. In the subsequent decades, catalyst technology has advanced from a simple cobalt oxide supported on asbestos to sophisticated, high-activity, highly-optimized cobalt catalyst supported on carefully-modified alumina, silica or titania and promoted with noble metals and basic oxides. With outstanding improvements in the experimental layout, catalyst design has evolved from a trivial trial and error procedure to a scientific, nanoscale design founded on activity-structure relationship.

Advances in cobalt catalyst design can be conveniently subdivided in six historical periods [7]:

1. ***Discovery (1902-1928)***. Cobalt catalysts were established as the most active and selective for FTS.
2. ***Commercial development of cobalt and iron catalysts (1929-1949)***. Mostly developed by the Nazis in Germany by *Ruhrchemie* and *IG Farben* (group including *BASF* at that time), where it contributed to gasoline and chemical production from coal during WWII and subsequently in USA. In 1928 the US company *Kellogg* made a first scale up of the reactor, building a 13 [m], high-circulating fluidized bed (CFB) reactor, soon shut down due to rising costs of natural gas. In these years, also 9 German plants were closed for the same reasons.
3. ***The "iron age" (1950-1974)***. Apartheid forced South Africa to take the lead in the field with its company *Sasol*, which in 1955 started performing FTS in the famous *Sasol I* plant. This employed three reactors in parallel, two CFB (with the same technology developed by *Kellogg*) and a FB (fixed bed). During the 1960's, oil price decreased thus leading to a partial abandoning of GTL technologies.
4. ***Rediscovery of cobalt (1975-1990)***. In 1973 OPEC embargo and the following energetic crisis renewed the interest in synthetic fuels, with Sasol playing a leading role with the construction of *Sasol II* plant in 1974, consisting of a CFB reactor three times bigger than those in *Sasol I*. Few years later the production was doubled with *Sasol III* plant (1980).

5. ***GTL and return to cobalt (1991-2014)***. After a new phase of stagnation, interest in FTS was raised again starting from the 90's with a renewed focus on conversion of natural gas to clean liquid fuels, both due to increasing oil prices and stricter environmental legislations. In 1993 *Shell*'s first plant in Bintulu started operating with a production of 12500 [bpd], followed in 2006 by *Sasol-Oryx* GTL plant, which produces 34000 [bpd].
6. ***Economic and oil crisis (2014-present day)***. From the second half of 2014, oil prices dropped 100$ per barrel to less than 30$ in a few weeks, thus strongly limiting the economic interest of FTS, which it is estimated to require to be competitive, with current technologies, values around 90$ per barrel [8].

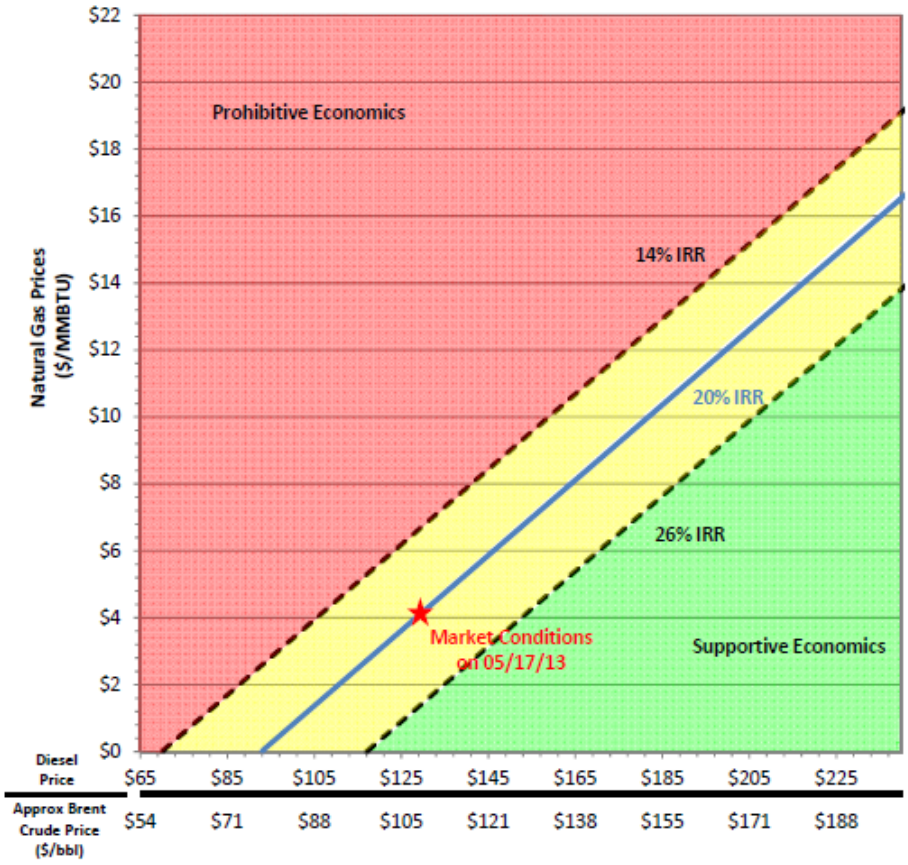

Figure 1.9: Viability envelope for GTL projects [8]

1.2.2 Active catalysts

It is well known that all Group VIII transition metals are active in FT synthesis. However, the only catalysts that have sufficient hydrogenation activity for commercial applications have Ni, Co, Fe or Ru as the active metal phase [9]. A common feature of these materials is their strong interaction with CO and the ability to dissociate adsorbed carbon monoxide. It should be noticed that CO adsorption should be neither too strong nor too weak, since this would lead to methanation rather than chain growth [10]. Coupling of partially hydrogenated surface intermediates leads to the formation of long-chain surface species, which upon desorption form a mixture of organic product compounds.

The exact choice of the metal to be used in a particular catalyst formulation depends on a number of parameters including the source of carbon used for making syngas (i.e. the syngas H_2/CO ratio), price and end product desired. Industrially, only Co-based and Fe-based catalysts are employed due to their optimal compromise between activity and costs. Ni has too high hydrogenation activity resulting in high yields of methane while Ru usage in industrial FT applications is questionable due to its prohibitive cost. Cobalt is 3 times more active than iron: however, its price is almost 250 times higher.

It has to be considered that FTS is always accompanied by the secondary *Water Gas Shift (WGS)* reaction, the relevance of which cannot be neglected for the catalyst choice. Catalysts for the conversion of syngas obtained from a carbon-rich source, such as coal, are usually Fe-based due to the high WGS activity of iron, which tends to re-equilibrate the H_2/CO ratio to the stoichiometric value needed for FTS.

Co-based catalysts are preferred for the production of heavy paraffins, due to their high selectivity towards hydrocarbons with high molecular weight. They require a relatively clean feedstock and produce much less oxygenates than Fe catalysts, due higher hydrogenation activity of Co compared to that of Fe. On the other hand, if linear olefins are wanted as end product, Fe-based catalysts are the best choice because hydrogenation of the primary formed olefins is less favored. However, Fe-based catalysts have the disadvantage of producing aromatics and oxygenates as by-products.

Another difference between Co and Fe is related to their sensitivity towards impurities in the gas feed, such as H_2S: Fe-catalysts are by far more resistant than cobalt catalysts. On the other hand, Co-based catalysts are known to be more resistant towards oxidation and more stable against deactivation by water.

Table 1.1: Overview of some features of Ni-, Fe-, Co- and Ru-based FT catalysts

Active Metal	Price	FT activity	WGS activity	Hydrogenation activity
Ni	++++	+	+/-	+++++
Fe	+	+	+++	+
Co	+++	+++	+/-	+++
Re	+++++	+++++	+/-	+++

It is remarkable that, despite the large body of papers and patents published in the last decades about possible improvements of Co-based catalysts, the modern FT catalysts are still very similar to the early ones prepared by Fischer and co-workers, consisting of promoted cobalt particles supported on a metal oxide.

Most of Co-based catalysts consist of the following components:

i. Metallic cobalt (Co^0) as the active phase;

ii. High surface area support: typically, alumina (Al_2O_3), titania (TiO_2) and silica (SiO_2). Its function is to provide mechanical strength and thermal stability while contributing to a high Co dispersion;

iii. Promoter metals (typically noble metals such as Ru, Re, Pd Pt, Rh): their roles may vary a lot, depending on the metal employed. For instance, platinum and ruthenium facilitate reduction of cobalt clusters thus increasing the number of cobalt active sites during reaction.

1.2.3 Chemistry

Although the chemistry of the Fischer-Tropsch synthesis is quite complex, the fundamental features can be represented with the overall stoichiometry:

Alkanes formation:

$$nCO + (2n + 1)H_2 \rightarrow C_nH_{2n+2} + nH_2O \qquad (1.2)$$

Alkenes formation:

$$nCO + 2nH_n \rightarrow C_nH_{2n} + nH_2O \quad (1.3)$$

The production of a specific hydrocarbon, other than methane, has not yet been achieved: what is formed is always a mixture of hydrocarbons with different chain lengths and so different molecular weights. Characteristic of the Fischer-Tropsch reactions is their high exothermicity: the formation of one mole of -CH_2- is accompanied by a significant heat release of about 40 [kcal].

1.2.3.1 Main Side Reactions

Along with the main reactions, some side reactions also occur:

Alcohols formation:

$$nCO + 2nH_n \rightarrow \mathrm{H}(CH_2)_n\mathrm{OH} + (n-1)H_2O \qquad \Delta H_{r,298} < 0\ [kcal/mol] \quad (1.4)$$

Water gas shift (WGS) reaction:

$$CO + H_2O \leftrightarrow CO_2 + H_2 \qquad \Delta H_{r,298} = -10\ [kcal/mol] \quad (1.5)$$

Bouduard reaction:

$$2CO \leftrightarrow CO_2 + C \qquad \Delta H_{r,298} = -41\ [kcal/mol] \quad (1.6)$$

Methanation reaction:

$$CO + 3H_2 \leftrightarrow CH_4 + H_2O \qquad \Delta H_{r,298} = -49\ [kcal/mol] \quad (1.7)$$

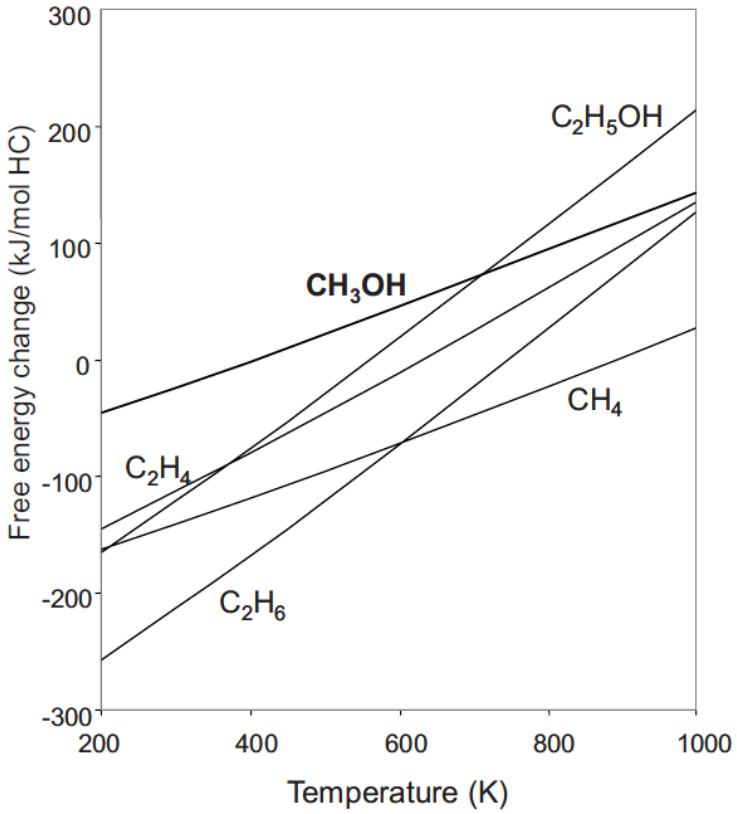

Figure 1.10: Products from CO and H_2, standard free energy of formation [11]

From the Francis diagram, reported in Figure 1.10, it is clear that thermodynamically both hydrocarbons and alcohols can be formed starting from syngas: for this reason, the choice of proper catalyst and operating conditions is very important.

The WGS reaction is responsible both for the production on CO_2 and the adjustment of the H_2/CO ratio. For example, in the Fe-catalyzed Fischer-Tropsch synthesis, the reverse-WGS, favored by the metal function, helps to bring the reactant ratio of a usually H_2-poor syngas (produced from biomass or coal) towards the stoichiometric value.

The *Bouduard* reaction is undesired as it produces CO_2 and coke; the latter covers the catalyst surface, leading to deactivation. Problems linked to the methanation reaction are the high exothermicity and the production of CH_4, a hydrocarbon of little value in the product distribution.

1.2.3.2 Mechanism

What really occurs on the surface of the catalyst during Fischer-Tropsch synthesis is still much debated among scientists. Many theories have been formulated to describe the evolution of the system during the reaction: although differences occur between them, the common element is the concept of a stepwise addition of monomeric C_1 units to a growing chain. The parallelism of a poly-addition mechanism is not far from the concept at issue, as in fact the product distribution is modeled from this similarity. The usual steps involved in the mechanism are the following ($*$ is referred to as the catalyst active site):

Reactant adsorption:

$$CO + * \rightarrow CO^* \quad (1.8)$$

$$H_2 + 2* \rightarrow 2H^* \quad (1.9)$$

In situ monomer formation:

$$CO + aH^* \rightarrow C_1^* + oxygenate\ species \quad (1.10)$$

Chain initiation:

$$C_1^* \rightarrow R_1^* \quad (1.11)$$

Chain propagation:

$$R_n^* + C_1^* \rightarrow R_{n+1}^* + * \quad (1.12)$$

Chain termination:

$$R_{n+1}^* \rightarrow paraffin\_A_n^* \quad (1.13)$$

Product desorption:

$$paraffin\_A_n^* \rightarrow paraffin\_A_n + * \quad (1.14)$$

Product re-adsorption and secondary reactions:

$$paraffin\_A_n + * \rightarrow paraffin\_A_n^* \quad (1.15)$$

$$paraffin\_A_n^* \rightarrow olefin\_A_n^* \quad (1.16)$$

The earliest hypothesis for the FTS mechanism was proposed by Fischer and Tropsch themselves in 1926 and is known as the "carbide theory". The first step is suggested to be the CO dissociative adsorption leaving an oxide and a carbide site, which would then both react with H_2 forming water and an adsorbed methylene species, respectively:

$$CO + 2* \rightarrow C^* + O^* \quad (1.17)$$

$$O^* + H_2 \rightarrow H_2O + * \quad (1.18)$$

$$C^* + H_2 \rightarrow CH_2{}^* \quad (1.19)$$

The methylene species, assumed as the $C_1{}^*$ monomer, is then inserted into a C_n growing chain, leaving an adsorbed C_{n+1} hydrocarbon species and a free active site:

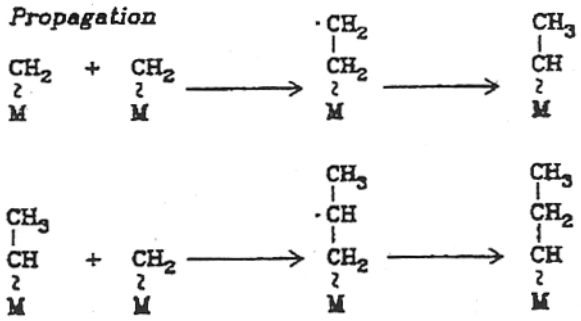

Figure 1.11: Propagation in the carbide theory [12]

Finally, the alkyl desorption proceeds via either dissociative β-H-abstraction or associative α-H-addition, leaving an α-olefin or a paraffin respectively:

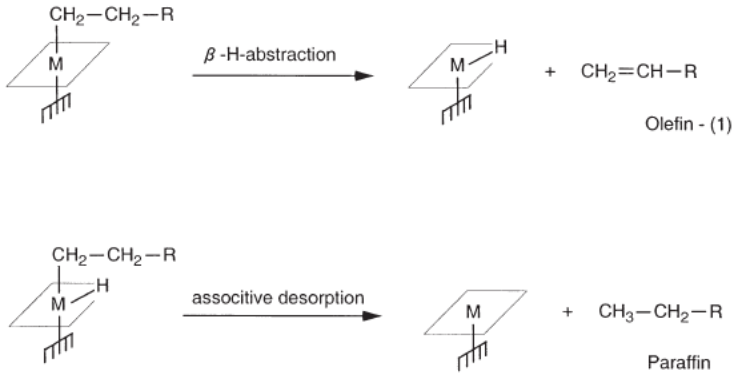

Figure 1.12: Termination in the carbide theory [13]

The main limitation of this theory is the impossibility of predicting the formation of oxygenate species, which are always present in the product mixture in rather small amounts. Nevertheless, experimental studies [14-15] which involved application of sophisticated surface analysis techniques are in accordance with the carbide theory. In fact, the general agreement is that carbenes (CH_2^*) are actually involved in the chain growth mechanism with CO insertion accounting for the formation of oxygenate compounds [16].

In the 1950s a new mechanism proposed by *Eiidus* [16], acknowledged as the "enol theory", gained widespread acceptance. It involves the chemisorption of CO which is then partially hydrogenated generating the C_1^* monomer unit (enol) active in the chain growth mechanism.

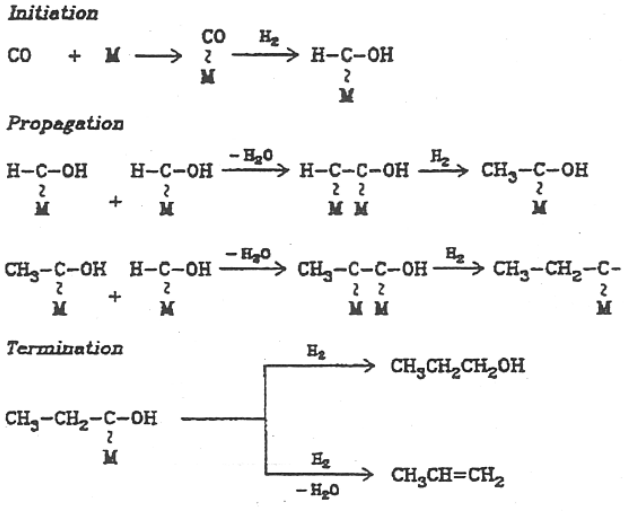

Figure 1.13: Scheme of the enol mechanism [12]

The propagation occurs via subsequent condensation of monomer units with the growing chain. Main benefit of this mechanism is the possibility of forecasting all the species produced during FTS: in fact, alcohols are generated by hydrogenation of the hydroxyl-carbene units, aldehydes by direct desorption and hydrocarbons by a double step of hydrogenation and condensation.

Another important theory is known as the "direct insertion theory", proposed by *Pichler et al.* [17] and later taken up by *Wender et al.* [18]. It proposes the insertion of the adsorbed CO molecule between the catalyst active site and the C atom of the adsorbed alkyl species, as per the reaction. The acyl group RnCO* is later hydrogenated forming an adsorbed alkyl chain with an additional methylene unit:

$$R_n^* + CO^* \rightarrow R_nCO^* + * \quad (1.20)$$

$$R_nCO^* + 2H_2 \rightarrow R_{n+1}^* + H_2O \quad (1.21)$$

The advantage of this theory is the same as the enolic, because it is capable of foreseeing formation of both hydrocarbon and oxygenate species.

Some alternative theories aim to couple the early hypothesis proposed by Fischer and Tropsch with the experimentally observed formation of oxygenate compounds. For example, *Dry* [16] proposed an additional chain growth mechanism, parallel to the carbide mechanism, leading to the formation of alcohols, aldehydes and carboxylic acids:

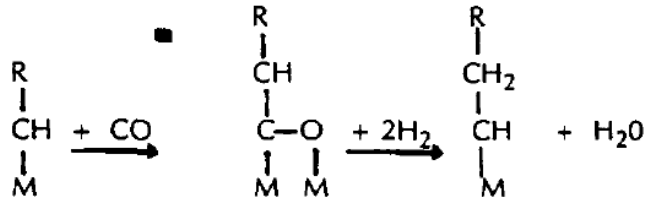

Figure 1.14: Chain growth proposed by Dry [16]

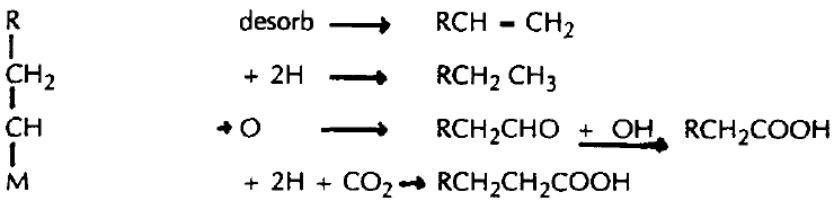

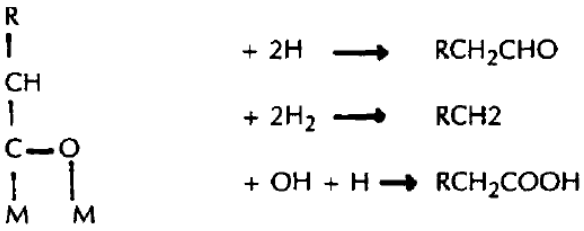

Figure 1.15: Termination proposed by Dry [16]

Although it may seem difficult that all of the above termination reactions do actually occur, the author defends his hypothesis ascribing it to the heterogeneity of the working surface of a FT catalyst, over which many different intermediates are likely to present.

An alternative mechanism that accounts for the oxygenates formation is the one proposed by *Schulz and Van Steen* [19]. Differently from *Dry* [16], a second series of reactions that lead to the solely formation of hydrocarbons is assumed to occur: in this way the larger presence of hydrocarbons against that of oxygenates is explained.

$$CO + * \rightarrow CO^* \quad (1.22)$$

$$CO^* \rightarrow C^* + O^* \quad (1.23)$$

$$H_2 + * \rightarrow 2H^* \quad (1.24)$$

$$C^* + H^* \rightarrow CH^* + * \quad (1.25)$$

$$CH^* + H^* \rightarrow CH_2^* + * \quad (1.26)$$

$$CH_2^* + R^* \rightarrow RCH_2^* + * \quad (1.27)$$

The incapacity of the theory of predicting the formation of alcohols, aldehydes and carboxylic acids is ascribed to the exclusive O^* desorption in the form of CO_2 and water. In addition, more recent studies seem in contrast with this mechanism as they suggest, instead of a simple molecular adsorption, an hydrogen assisted CO dissociation to form the active monomer [20].

The difficulty of some of the theories in describing the whole product range and the different catalytic behaviour of the metals industrially employed has led some scientists to speculate on the presence multiple key intermediates in FT synthesis [21].
In particular, it has been proposed that the direct CO insertion mechanism is responsible of the oxygenates formation, while the hydrocarbons are formed as stated by the carbide theory.

More recent studies [22] have led to the definition of an innovative kinetic mechanism in which the adsorbed CO can follow two reaction pathways, depending on the hydrogen role in its activation.

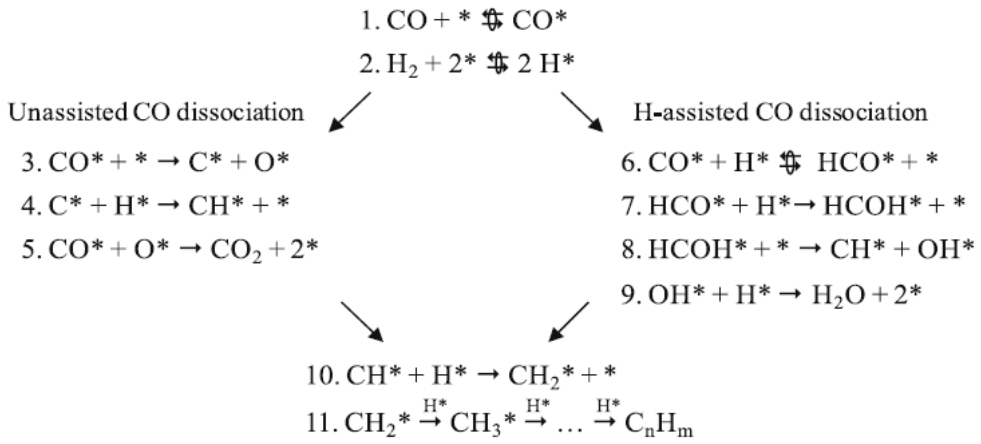

Figure 1.16: Chain growth mechanism according to *Iglesia et al.* [22]

The unassisted dissociation leads to the formation of two intermediates, C^* and O^*, from an adsorbed CO molecule. C^* further reacts with hydrogen forming the active monomer, whereas O^* reacts with another CO^* molecule forming carbon dioxide. In the parallel mechanism, referred to as the "H-assisted CO dissociation", a formyl (HCO^*) intermediate is formed: it is then hydrogenated forming an hydroxylmethylene ($HCOH^*$) species which subsequently dissociates forming CH^* and

OH^*. The latter are then hydrogenated forming, respectively, the active monomer and water. In addition, Iglesia et al. [22] could prove, through theoretical and kinetic studies, that the CO dissociation mechanisms are different depending on the catalyst employed. Iron is known to be more selective towards CO_2: the reason of this behaviour is ascribed to a lower activation energy for the unassisted CO dissociation pathway. On the other hand, the H-assisted CO dissociation is predominant when using cobalt catalysts: this is perfectly in line with the much lower CO_2 productivity compared to that obtained using iron.

1.2.4 Product distribution

Various mechanisms have been proposed to describe the product distribution of the FT synthesis. However, no matter what the exact mechanism is, the growth of a hydrocarbon chain is assumed to occur by a stepwise addition of a C1 unit derived from CO to the end of the growing chain. The widely recognized statistical distribution model is the one formulated by Flory [23] and then developed by Anderson and Schulz [24], known as the ASF distribution. The theory is based on the parallelism between the chain growth mechanism of the FT synthesis and that of a poly-addition reaction. In addition, some simplifications are also taken into account:

- Absence of branched products
- No difference between the growth of olefins and paraffins
- Absence of secondary reactions
- Relative probability of chain growth and termination independent of the carbon number

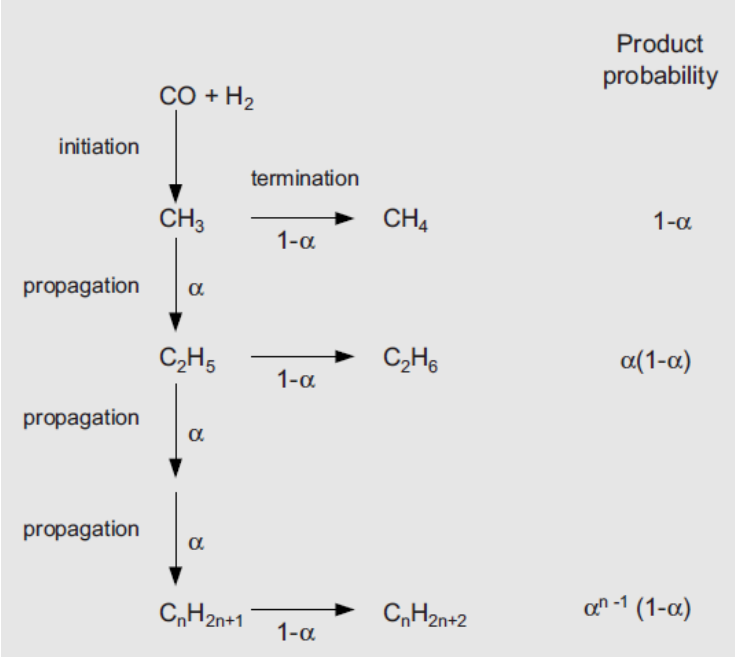

Figure 1.17: Chain growth mechanism for FT synthesis: ASF [11]

The relative probability of chain growth is identified in the ASF model with the greek letter α. It is defined by:

$$\alpha = \frac{R_P}{R_P + R_T} \qquad (1.28)$$

Where R_P and R_T correspond to the propagation and termination rate, respectively. α is a dimensionless parameter, independent of the carbon number, which assumes values in the range 0 ÷ 1. Typical values [25] for Co and Fe catalysts are around 0.5 ÷ 0.85.

As shown in the Figure 1.17, a single chain growth step has a probability α, whereas the termination reaction has a probability (1- α). The null value of α corresponds to a 100% termination probability, whereas the unity value corresponds to a 100% propagation probability. Therefore, the probability of obtaining a hydrocarbon with *N* carbon atoms in its chain (P_N) is given by the achievement of *(N-1)* polymerization steps followed by a termination step. As each step is regarded as a statistically independent event, the probability of obtaining P_N is given by the probability product of the events associated to the formation of P_N:

$$P_N = \alpha^{N-1} \cdot (1 - \alpha) \tag{1.29}$$

The probability P_N can be referred to as a molar fraction of the C_N species. It is possible to switch to mass fractions by means of a constant denoted with *A*:

$$\omega_n = A \cdot P_N \cdot n \tag{1.30}$$

The constant *A* can be found by imposing the stoichiometric balance in the reaction:

$$\int_0^\infty \omega_n dn = 1 \tag{1.31}$$

$$\int_0^\infty (A \cdot P_N \cdot n)\, dn = 1 \tag{1.32}$$

By substituting the expression of P_N and solving the integral, the expression assumed by A is the following:

$$A = \frac{\alpha \cdot log^2 \alpha}{1-\alpha} \tag{1.33}$$

Substituting the value of A into the mass fraction expression (Eq. 1.30) and rearranging the terms the final equation of the ASF model is obtained:

$$\log\left(\frac{\omega_n}{n}\right) = \log(log^2 \alpha) + n \log \alpha \tag{1.34}$$

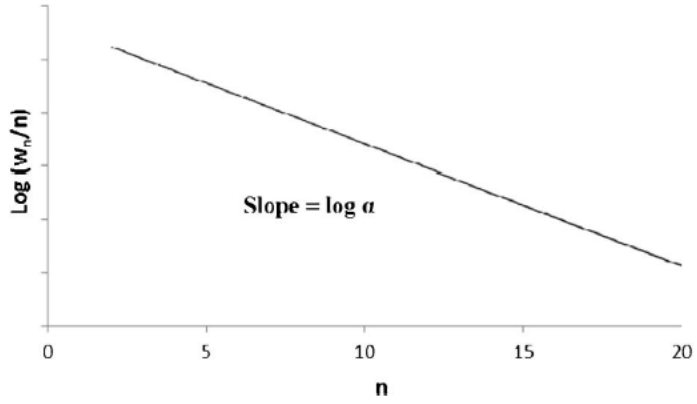

Figure 1.18: Classical ASF product distribution [26]

Being α between 0 and 1, and thus negative the slope, a decreasing profile is obtained. The closer is α to one, the richer will be the product mixture of heavy hydrocarbons. With the ASF equation, all the complexity of the FTS kinetics governing the product distribution is conveniently lumped into the single parameter α.

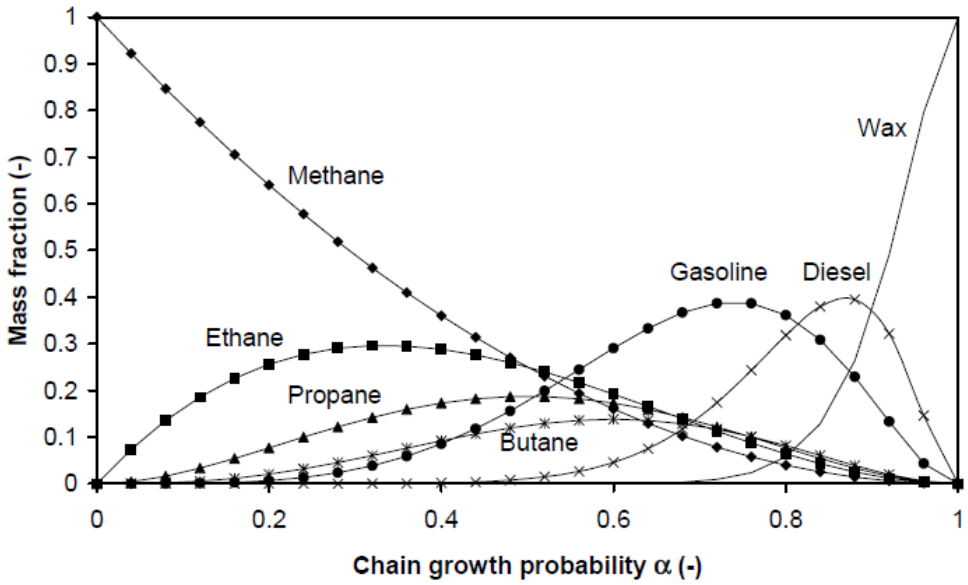

Figure 1.19: Product mass fraction profiles as a function of α [27]

Industrially, as diesel and waxes are the desired products, the catalyst and process conditions are tailored to obtain α values around 0.8 ÷ 0.9. More recently the aim has shifted towards maximum yield just in waxes (α ≈ 0.95), which can be obtained with higher selectivity than diesel and can then be further converted into valuable products [11].

At the expenses of its high simplicity, the ASF model unfortunately presents some discrepancies when compared to the experimental data obtained in FT conditions.

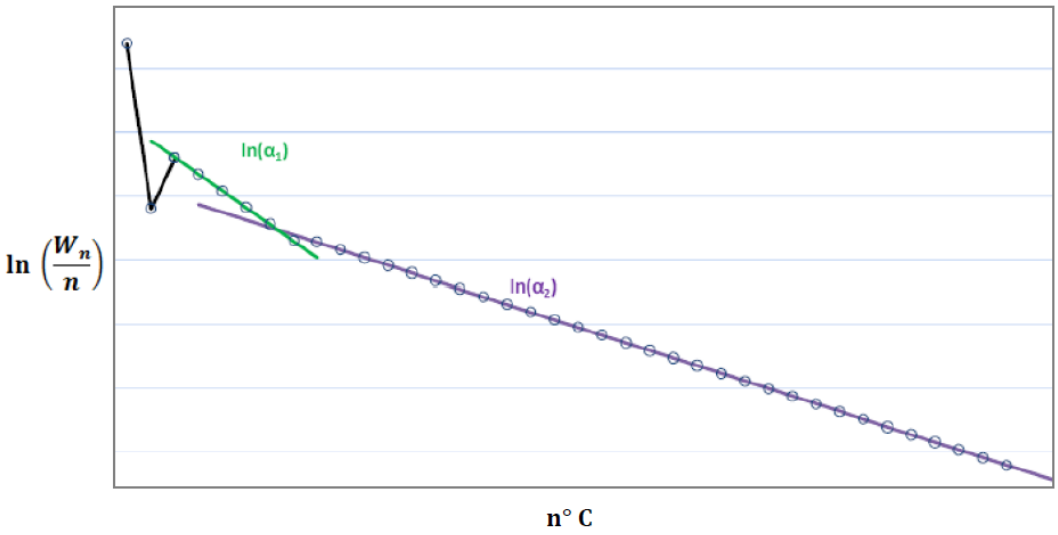

Figure 1.20: Typical experimental distribution of FT products [28]

In particular:

- The methane yield is underestimated
- The ethylene yield is overestimated
- The value of α increases when increasing the carbon number

An addition, neglecting the assumptions made concerning olefins and paraffins, one would observe a decreasing trend in their ratio when increasing the carbon number. The following paragraphs focus on the main reasons for which the ASF theory lacks in correctly describing the whole hydrocarbon yield.

Deviation of C_1

It is clear from Figure 1.20 that the ASF model underestimates the experimental methane production. This behaviour can be at first ascribed to the possible activity of FT catalysts towards hydrogenolysis reactions of paraffins and olefins. In addition, also diffusive limitations can play an important role: as H_2 molecular diffusivity is way higher than that of CO, deep in the catalyst pores the H_2/CO ratio may lie above the optimal one, thus favouring the methanation reaction. Other theories attribute the excessive methane production to the formation of local hot-spots on the catalyst.

Deviation of C_2

The experimental data on the C_2 selectivity are instead overvalued by the ASF model. This overestimation is ascribed to re-adsorption mechanisms of ethylene which is then reintroduced into the polymerization pathway. Alternatively, the deviation can be attributed to the high reactivity and surface mobility of the C_2 precursors.

Variation of chain growth probability and olefin to paraffin ratio

The main lumped kinetic approaches dealing with deviations from the ASF distribution can be divided into two schools of thought: the first asserts the presence of a bimodal distribution of α in the ASF (double-α chain growth models), the second ascribes the discrepancy of the olefin to paraffin ratio to n-olefin readsorption mechanisms which would favour paraffin formation (olefin-readsorption models).

Double-α models

Since experimentally an increase of the chain growth probability was often observed at carbon numbers around 10, some authors decided to describe the total hydrocarbon yield by means of two ASF distributions. In particular, *Madon and Taylor* [29] credited the double-α behaviour to the presence of structurally different active sites on the catalyst surface: one over which the C_1-C_{10} production dominates (α_1), another where heavier products are more likely formed (α_2). The same hypothesis was made by *Wojciechowski* [30]: each active site has its own chain growth probability and, depending on the termination reaction by adding either hydrogen or a methyl group, different product distributions are obtained.

Other authors [31] associated the double-α behaviour to different chain growth mechanisms. Nevertheless, it is worth noticing that, even though these theories can explain the change of α in the ASF distribution, they are unable to predict the related drop in the olefin to paraffin ratio.

Olefin-readsorption models

A more likely explanation of the deviation from the ASF distribution involves secondary reactions (reinsertion, hydrogenation, hydrogenolysis and isomerization) of olefins. The olefin-readsorption models could in this way fill the lack of the double-α models, predicting both the increase of the chain growth probability and the decrease of the olefin to paraffin ratio. The qualitative profile of the latter can be expressed with the empiric law formulated by *Kuipers et al.* [32]:

$$\frac{O_N}{P_N} \propto e^{-C \cdot N} \qquad (1.35)$$

Where C is a constant while O_N and P_N are the molar fractions of an olefin and a paraffin, respectively, with N carbon atoms in its chain. This theory is strengthened by experimental evidence of olefin readsorption on the active sites, which results in a heavier and more paraffinic product mixture.

These secondary reactions that cause the deviations in the ASF distribution are generally accepted to be chain-length dependent. Three different phenomena influenced by the chain length have been proposed by *Kuipers et al.* [32]:

- The diffusion of olefins within the catalyst pores filled with liquid product
- The solubility of olefins into the liquid product
- The physisorption of olefins in the proximity of the catalyst surface

It is evident from these phenomena the importance of the interfacial effects of the reactive olefins with the gas-liquid and the liquid-catalyst surface interfaces.

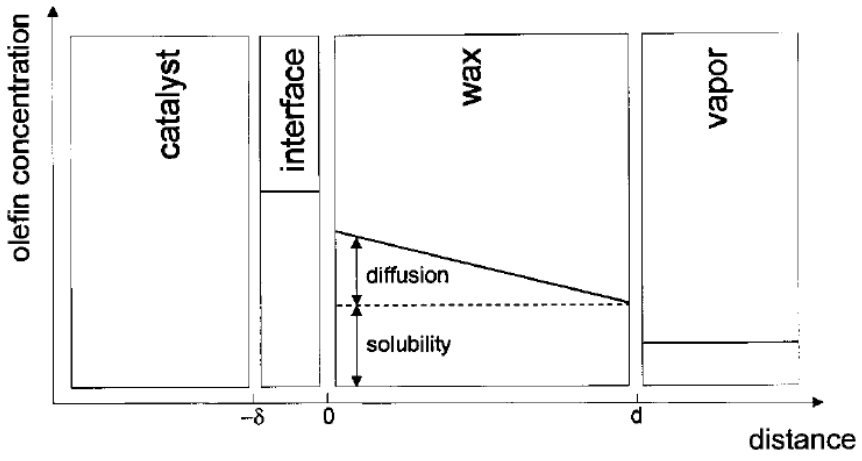

Figure 1.21: Olefins concentration profile across the phases [32]

Figure 1.21 is a schematic representation of the olefin concentration profile in the reaction environment. Within the film of liquid product (0 < x < d) over the catalyst an olefin concentration gradient is established: it is dependent of the olefin formation rate, the layer thickness and the liquid phase diffusivity ($\mathfrak{D}_N$). The latter is in turn function of the chain length via the following relation, proposed by *Van der Laan et al.* [25]:

$$\mathfrak{D}_N \propto N^{-0.5} \tag{1.36}$$

A similar relation is proposed by *Iglesia et al.* [33], who use an exponential function with a different coefficient:

$$\mathfrak{D}_N \propto \mathfrak{D}_0 \cdot e^{-0.6N} \tag{1.37}$$

Where $\mathfrak{D}_0$ is the reference diffusion coefficient ([m^2/s]).

The physisorption of olefins is in turn referred to as a chain length independent phenomenon which occurs on the catalyst surface (x = δ). Iglesia stated that the real reason of the decrease in the O_N/P_N ratio is to be imputed to diffusion limitations. As shown by Eq. 1.37, increasing *N*, the mobility of olefins in the liquid phase exponentially decreases: as a consequence, the contact time with the catalyst surface increases, resulting in a higher readsorption probability. However, the relation obtained by *Iglesia et al.* [34], even with its strong chain length dependency for the diffusion coefficients, cannot predict the strong decrease in the olefin to paraffin ratio found experimentally. Moreover, other studies [35] have shown more reasonable chain length dependencies of the diffusion coefficients, and using these diffusivities the model by *Iglesia et al.* [34] appears to underestimate the O_N/P_N ratio.

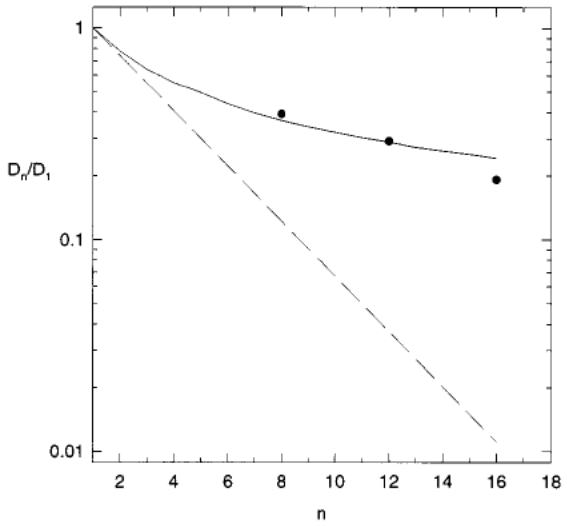

Figure 1.22: Diffusivities of n-paraffins in solid wax at 540 K [25]

Furthermore, *Kuipers et al.* [32] measured the O_N/P_N ratio for the FTS on a polycrystalline cobalt foil, which structurally cannot generate diffusion limitations, and still found a strong exponential decrease with the chain length. Apparently, not only diffusion limitations have to be taken into account for the description of the product distribution, but also solubility and physisorption become relevant. *Van der Laan* [25] proposed the so-called "Olefin VLE model", in which the chain length dependence of the olefin readsorption rate is credited to their increasing solubility in the FT waxy products. Generally, the most common species in the hydrocarbon phase are olefins with carbon numbers around 23 ÷ 30: as a consequence, the solubilisation of heavier olefins is the most favoured, due to the high affinity of the latter with the hydrocarbon solvent. Likewise, also physisorption phenomena appear to affect the olefin to paraffin ratio. *Keldsen et al.* [25] measured the adsorption enthalpies of paraffins and found that the energetic levels for the adsorbent-adsorbate interactions vary with *N* according to the following equation:

$$-\Delta H_{ADS} = 12.6 + 8.7 \cdot N \tag{1.38}$$

Therefore, a high concentration of heavy products is found across the catalyst-liquid interface.

1.2.5 Influence of process conditions on the selectivity

It is widely accepted that the chain growth probability varies with the process conditions. A recapping table showing the main effects is reported by *Van der Laan and Beenackers* [25]:

Table 1.2: Selectivity Control in Fischer–Tropsch Synthesis by Process Conditions [25]

Parameter	Chain length	Chain branching	Olefin selectivity	Alcohol selectivity	Carbon deposition	Methane selectivity
Temperature	↓	↑	*	↓	↑	↑
Pressure	↑	↓	*	↑	*	↓
H_2/CO	↓	↑	↓	↓	↓	↑
Conversion	*	*	↓	↓	↑	↑
Space velocity	*	*	↑	↑	*	↓
Alkali content iron catalyst	↑	↓	↑	↑	↑	↓

Note: Increase with increasing parameter: ↑. Decrease with increasing parameter: ↓. Complex relation: *.

Temperature

Although an increase in temperature would favour the FT kinetics, the main drawback is a decrease in the chain growth probability, due to the increasing desorption rates favoured by the high temperature. The model derived by *Song et al.* [36] as a linear interpolation of experimental data, which were obtained by *Van der Laan and Beenackers* [25], emphasises the temperature dependence of the α parameter:

$$\alpha = \left(A\frac{y_{CO}}{y_{CO}+y_{H_2}} + B\right)[1 - 0.0039(T - 533)] \qquad (1.39)$$

Being A = 0.2332 ± 0.0740, B = 0.6330 ± 0.0420, T the temperature [K], y_{CO} and y_{H2} the molar fraction of the feed gas. Figure 1.23 represents how the product distribution varies with temperature, at a fixed syngas composition (H2/CO = 2), as predicted by *Song et al.* [36]:

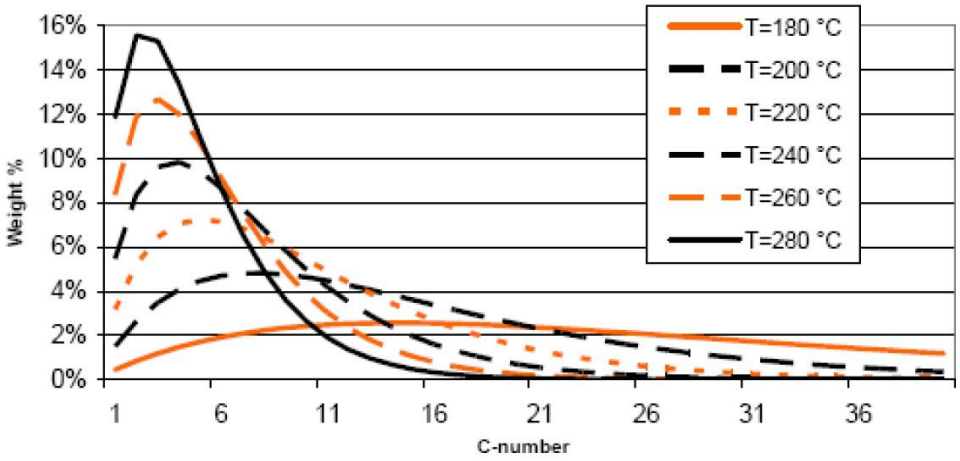

Figure 1.23: Product distribution as a function of temperature [36]

Partial pressure of CO and H_2

It is widely recognized that the chain growth probability increases when increasing pressure: this behaviour can be credited to the limited desorption rate at higher pressures. In this manner, the product remains longer on the catalyst surface and grows its chain. Thus, in principle, the higher the pressure, the higher would be α. In the industrial process, though, the pressure choice is made in view of other major drawbacks of high operating pressures, which are significant pumping costs, high pressure drops and necessity of resistant materials. Industrial FT processes are commonly operated at 20 ÷ 25 [bar].

In terms of partial pressures, H_2 is known to favour hydrogenation reactions, i.e. termination reactions, so high H_2/CO ratios tend to lower the chain growth probability. Figure 1.24 shows the product distribution as a function of the partial pressures of *CO* and H_2:

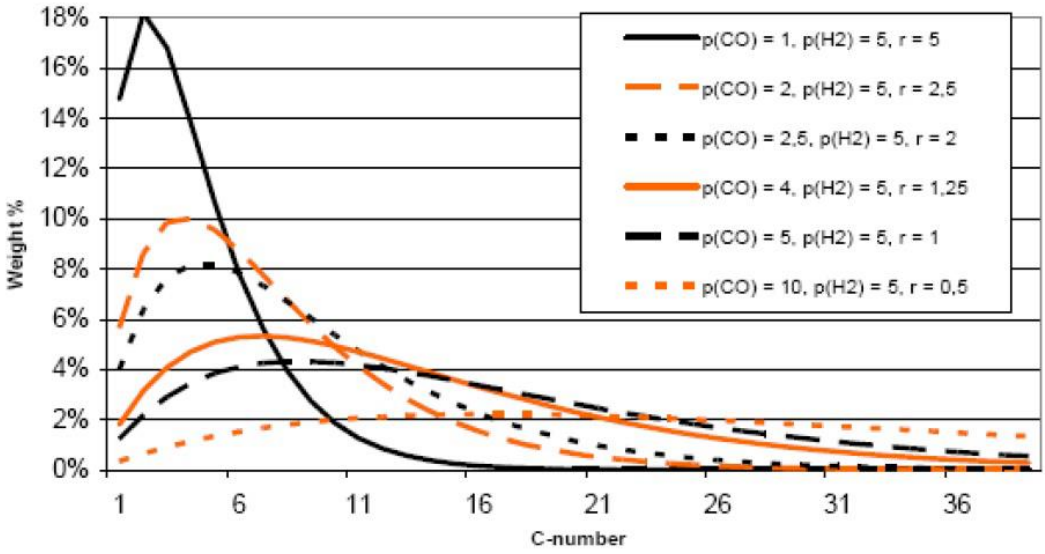

Figure 1.24: Product distribution as a function of the H_2/CO inlet ratio *r*

Space velocity

The effect of space velocity has been studied by various authors. *Kuipers et al.* [37] found an increase of the O_N/P_N ratio when decreasing the contact time (i.e. increasing the space velocity) and *Iglesia et al.* [33] measured an increase in the average product molecular weight when increasing the contact time. Thus, apparently, low space velocities favour the yield in the desired product: again, industrially the main drawback of operations with low gas flows is the inefficient heat removal, due to the low heat transfer coefficients. In such a highly exothermic process as FTS temperature control is a major concern, thus gas velocities need to be kept high: so, in order to ensure both the contact time needed for a good selectivity and high heat transfer coefficient, high flows and long tubes are industrially employed.

1.2.6 LTFT and HTFT operations

Usually FT processes can be classified, according to the operating temperatures, into *Low Temperature FT (LTFT)* and *High Temperature FT (HTFT)*.

LTFT processes are usually operated at T = 200 ÷ 240 [°C] and aim at the production of heavy hydrocarbons, which are then upgraded to a high quality diesel. The reaction environment of a LTFT process is triphasic: it comprises a gaseous phase, consisting of syngas and light products, a liquid phase, rich in waxy products, and a solid phase, which is the catalyst.

HTFT processes operate at significantly higher temperatures (T = 300 ÷ 350 [°C]) and aim to produce light hydrocarbon products in the range C_2 ÷ C_{11}, which are then upgraded to gasoline. Such high temperatures are needed to guarantee gas-solid operations.
Figure 1.25 shows typical product distributions for both the process choices, compared to the composition of a light crude oil:

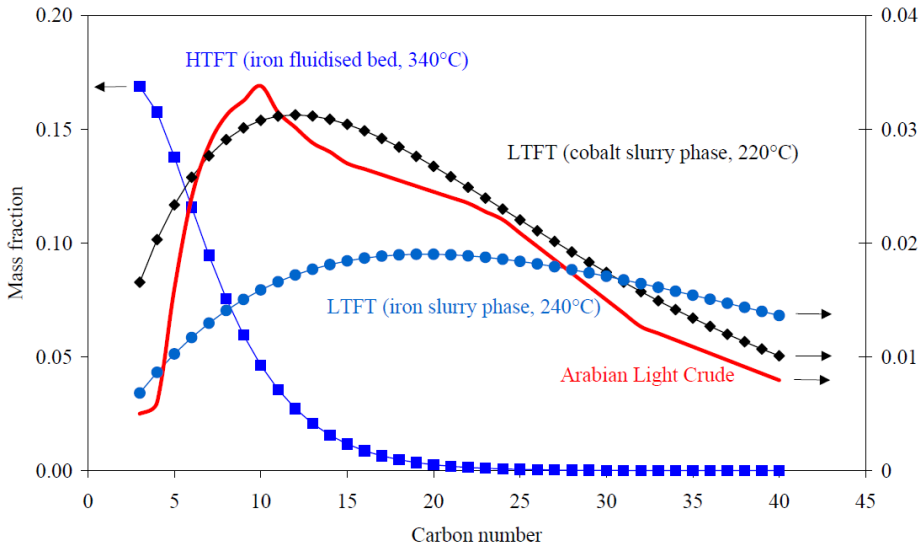

Figure 1.25: FT product distribution: HTFT vs LTFT [38]

The closest composition to that of the Arabian Light Crude appears to be the syncrude obtain at low temperatures using Co-based catalyst.

Along with the product distribution, also the catalyst choice is strictly related to the operating conditions. More in particular:

- Co is employed at low temperature (Co-based LTFT)
- Fe is used both at high and low temperatures (Fe-based LTFT & Fe-based HTFT)

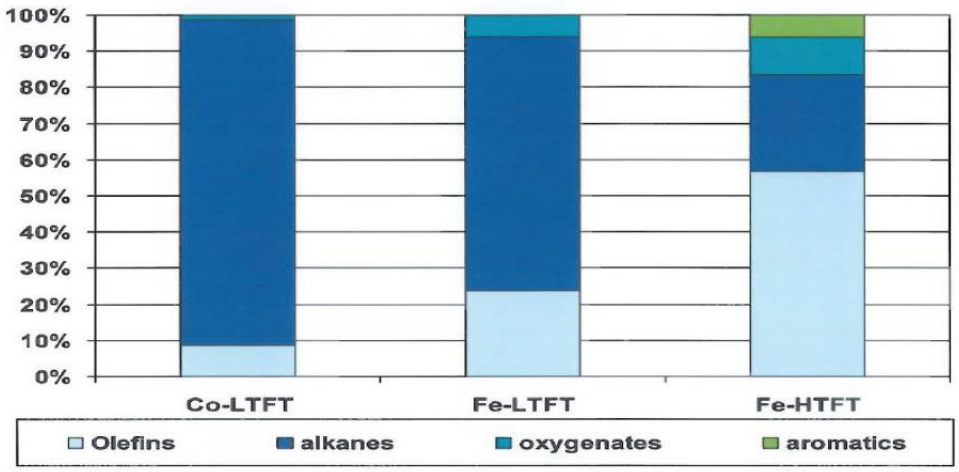

Figure 1.26: Product yield with different processes [38]

1.2.7 FT reactors

When designing reactors for Fischer-Tropsch synthesis, the major concern is always temperature control. Being the reaction strongly exothermic, the objective is to minimise the temperature rise along the bed: to achieve this requires a rapid heat removal in the direction perpendicular to the reactant flow. Being FT synthesis kinetically controlled, the objective of keeping the temperature down is not related to equilibrium considerations such as in other industrial processes, like methanol or ammonia production. The reasons for the strict temperature control are instead mainly related to the catalyst activity and product selectivity, as discussed in Section 1.2.6.

As in most exothermic processes, the heat removal is performed via heat exchangers, fed with water, which produce useful steam for the process. The higher the temperature of the heat exchange, the higher the pressure of the steam produced and the higher the overall thermal efficiency of the process. To achieve rapid heat transfer from the reaction zone to the heat exchanger wall, different configurations are industrially employed:

- *Multi-tubular fixed bed reactor* (MTFBR)
- *Circulating fluidized bed reactor* (CFBR)
- *Slurry bubble column reactor* (SBCR)

1.2.7.1 Multi-tubular fixed bed reactor (MTFBR)

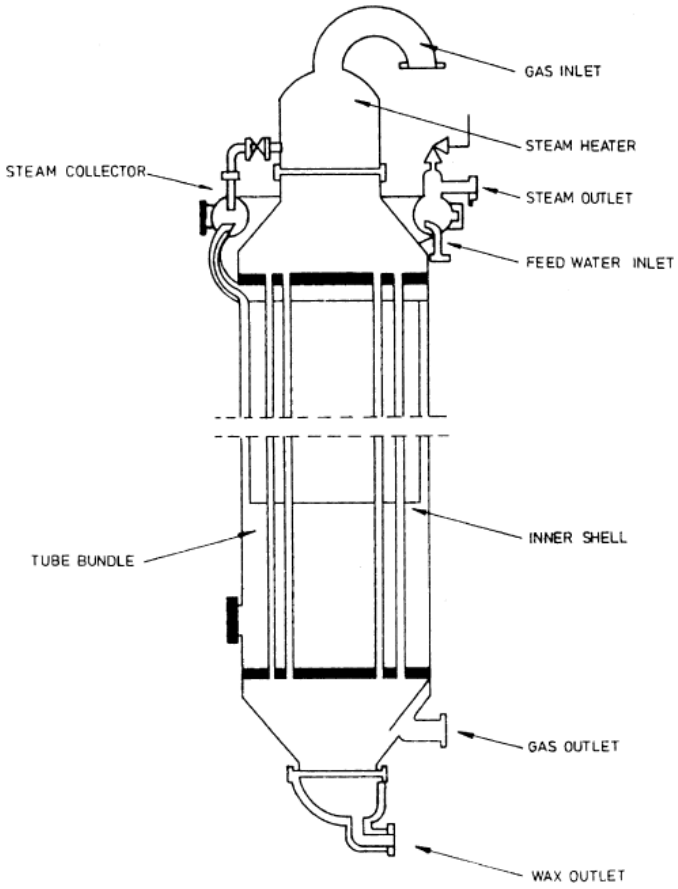

Figure 1.27: Multitubular Fixed Bed Reactor [29]

The multi-tubular reactor design comprises thousands of long (12 ÷ 20 [m]) and narrow (2 [in]) tubes, filled with catalyst particles, inserted into a vessel in which cooling water flows shell-side.

The syngas mixture flows tube-side and reacts along the catalyst bed, producing heat. Typical operating conditions of these units are reported below:

Table 1.3: Multitubular Fixed Bed Reactor: operating conditions

MTFBR	
Temperature [°C]	200 ÷ 220
Pressure [bar]	25
Active Phase	Iron / Cobalt

The advantage of using narrow tubes is the reduction of the distance between the centre of the tube, where usually the hot spots occur, and the tube wall, surrounded by the coolant. In addition, for the same bed volume, a higher number of tubes results in a higher heat transfer area, ensuring a better heat removal.

Also, high gas velocity produces a turbulent flow, which increases heat transfer coefficients and minimizes the thickness of the stagnant layer, over the catalyst surface and the tube wall, of reactants and products: this layer has to be minimized as it limits the heat transfer.

The advantages of a MTFBR design are as follows. They are easy to operate. There is no problem of catalyst-product separation. The liquid product trickles down the reactor and is collected at the bottom, where it is easily separated from the gas phase via a knock-out vessel: for this reason, the MTFBR design is suitable for wax production. On the other hand, many are the economical disadvantages. The construction cost is substantial. The high flow rate, needed for an efficient heat transfer, results in large pressure drops along the bed, which, coupled with the gas recycle, make the compression costs rise significantly. As FT is diffusion limited, the use of small particles would increase the catalyst efficiency and thus the production: however, this would result in an even higher differential pressure over the reactor.

Another major drawback is linked to the catalyst replacement: the latter is, due to the narrow tubes employed, a challenging operation that cannot be performed on-line. Obviously, the longer the downtimes, the greater the economic loss for the plant.

1.2.7.2 Circulating fluidized bed reactor (CFBR)

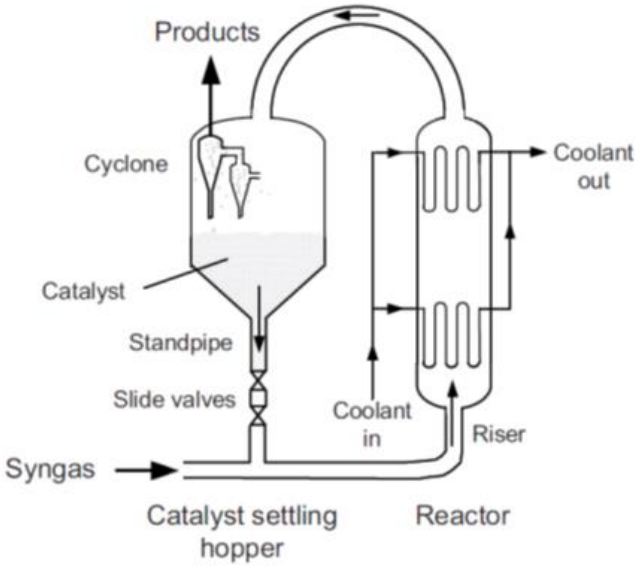

Figure 1.28: Circulating fluidized bed reactor [11]

An alternative way to ensure an efficient heat transfer is to fluidize the catalyst bed and "move" it to the heat exchanger. This reactor design consists of two main zones: the reaction and the catalyst separation zone. In the reaction zone the syngas mixture is contacted with the catalyst particles and the reaction occurs: heat is removed by cooling water circulating in coils. The small catalyst particles are entrained by the gas flow and pushed upwards, towards the catalyst separation zone. Here, the cross section increases and the catalyst particles fall down, whilst the gaseous products are recovered from the top; a system of cyclones ensures an efficient gas-solid separation. The catalyst at the bottom of the separation zone is then sent back to the reaction zone for another cycle. The bed fluidization would be impossible if a liquid phase were involved: for this reason, the CFBR design is employed only in HTFT operations.

Table 1.4: Circulating Fluidized Bed Reactor: operating conditions

CFBR	
Temperature [°C]	330
Pressure [bar]	20 ÷ 40
Active Phase	Iron

The main advantages of this reactor choice are as follows. The investment cost is lower, compared to that of a MTFBR. The direct physical contact between catalyst particles and heat exchanger walls, along with the high flow rates needed to fluidize the system, contribute to a significant improvement in the temperature control, when compared to that of the MTFBR. The higher the heat transfer efficiency, the lower is the exchange area required and, in turn, the investment cost. Once the catalyst particles are fluidized, further increases in the space velocity do not affect the pressure drops, which are in any case lower than that of a fixed bed reactor: also the compression costs are less. Furthermore, the fluidized bed operation makes the catalyst replacement easier and feasible on-line: losses due to down-time and labour intensive turn-arounds are in this way eliminated.

The main disadvantages of CFBR are linked to the small dimensions of the catalyst particles (100 [μm]). The latter are subjected to high mechanical stresses due to the high gas flow rates and the frequent collisions with the walls. Even though cyclone efficiencies are well above 99%, some of the small fines formed may be entrained by the gas flow exiting the reactor. For this reason, an additional separation unit based on oil scrubbing has to be placed downstream of the reactor: usually these units are complex and energy intensive, resulting in a lower thermal efficiency of the whole process.

1.2.7.3 Slurry bubble column reactor

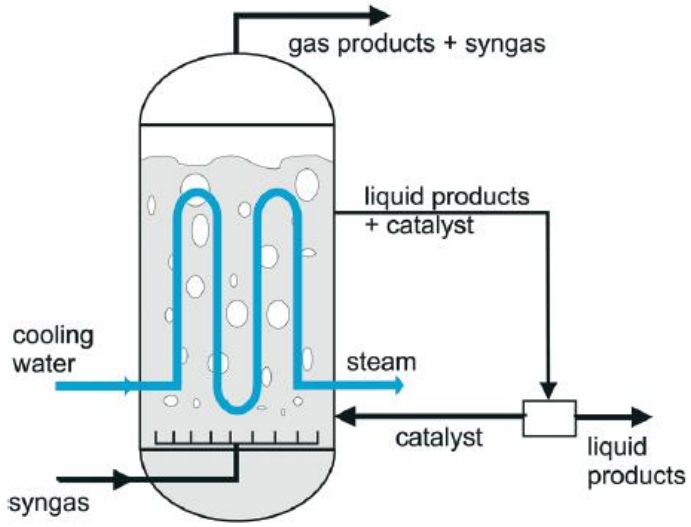

Figure 1.29: Slurry Bubble Column Reactor [39]

The slurry reactor is another version of the fluidized bed reactor. However, differently from the latter, it is operated as a three-phase system. For this reason, the SBCR is preferred for wax production (LTFT). The finely divided catalyst is suspended in the product waxy medium and syngas bubbles upwards from the bottom of the reactor. The heat produced is removed by boiler feed water, which circulates in coils placed inside the reaction environment. The volatile hydrocarbons and unreacted syngas are recovered from the top, while the liquid, and the catalyst suspended in it, are sent to a separation unit where the catalyst is recovered and sent back to the reactor.

Table 1.5: Slurry Bubble Column Reactor: operating conditions

SBCR	
Temperature [°C]	200 ÷ 250
Pressure [bar]	25
Active Phase	Cobalt / Iron

The main advantages for this reactor design are as follows. The construction cost of equivalent capacity reactors is 40% less for the slurry [40] : therefore, large scale design is preferred. The excess liquid wax offers a large heat sink, which provides a very efficient temperature control and almost isothermal conditions in the entirety of the reactor. The pressure drop is significantly lower than that of the MTFBR and this translates to lower compression costs. As for the CFBR, the catalyst replacement is rather simple and can be done on-line.

Along with these advantages, there are also some important drawbacks. The catalyst-product separation is challenging: the density difference between the two, that is about 0.7 [g/cm^3] for Fe catalyst and 0.68 [g/cm^3] for waxes, is too small to have a simple gravitational separation. The catalyst is subjected to high mechanical stresses. The presence of sulphur affects all the reaction environment, leading to a faster deactivation: in MTFBR these problem would only affect the initial part of the catalyst bed.

Table 1.6 recaps typical dimensions and operating conditions for the described conventional reactor designs:

Table 1.6: Typical dimensions and operating conditions of FT reactors (Fe catalyst) [11]

	Multitubular fixed bed reactor	Slurry-phase reactor	Circulating fluidized bed reactor
Dimensions			
Reactor height (m)	12	22	46
Reactor diameter (m)	3	5	2.3
Tube diameter (m)	0.05	—	—
Number of tubes	>2000	—	—
Catalyst size	1–3 mm	10–150 μm	40–150 μm
Reactor capacity (b/d)	600	2500	1500
Potential reactor capacity (b/d)	3000	30 000	8000[a]
Conditions			
Inlet *T* (K)	496	533	593
Outlet *T* (K)	509	538	598
Pressure (bar)	27	15	22
H_2/CO feed ratio (mol/mol)	1.7–1.8	≥0.7	2.5–3

[a]Capacities of CFB reactors at the Sasol II and III plants were 7500 b/d.

1.2.8 Overview of industrial Fischer-Tropsch processes

The objective of this paragraph is to provide an overview on the main process technologies aimed at the production on synthetic fuels and inspired to the original Fischer-Tropsch process, with some differences in terms of catalyst, reactor and operating conditions. Various companies are active today in FT research and development, but only few are currently running industrial processes:

Table 1.7: Currently operating and planned Fischer-Tropsch plants [11]

Company	Location	Feedstock	Reactor (catalyst)	Operation	Current liquids output (b/d)
Sasol (I)	Sasolburg, South Africa	initially coal, currently natural gas	fixed bed (Fe) CFB (Fe) slurry (Fe)	1955 – present 1957–1993 1993 – present	5000
Sasol (Sasol Synfuels[a])	Secunda, South Africa	coal, currently supplemented by natural gas	CFB (Fe) FFB (Fe)	1980–2000 1995 – present	160 000
PetroSA[b]	Mossel Bay, South Africa	natural gas	CFB (Fe)	1991 – present	30 000
Shell	Bintulu, Malaysia	natural gas	fixed bed (Co)	1993 – present	14 700
Sasol-Chevron/Qatar Petroleum (Oryx)	Ras Laffan, Qatar	natural gas	slurry (Co)	2007 – present	34 000
Shell/Qatar Petroleum (Pearl)	Qatar	natural gas	fixed bed (Co)	2011/2012	140 000
Sasol-Chevron	Escravos, Nigeria	natural gas	slurry (Co)	2013	34 000

[a]Formerly Sasol II and Sasol III.
[b]Formerly Mossgas.

1.2.8.1 Processes based on conventional reactors

Sasol I

The original *Sasol I* plant, based in Sasolburg (South Africa), went on-stream in 1955: it processed coal, of which South African has large reserves, producing synthetic fuels (5000 [bpd]). The plant design was rather complex, as it comprised both the high temperature and low temperature FT technologies. In the 2000s, the plant was readjusted to process natural gas instead of coal, becoming in effect a GTL plant for chemicals and waxes production.

Figure 1.30 shows the simplified flow block diagram of the original plant:

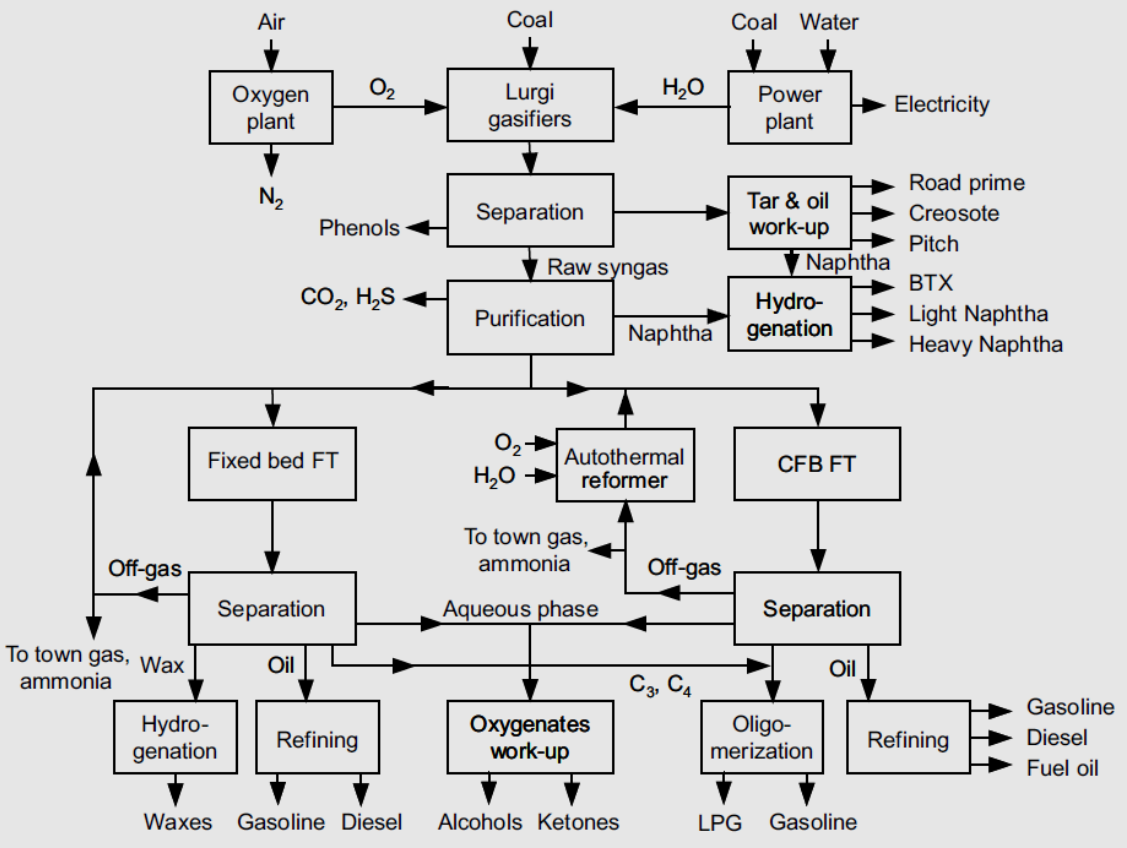

Figure 1.30: Simplified flow block diagram of Sasol I plant [11]

Coal is gasified with pure oxygen, coming from the air separation unit, into a Lurgi reactor. The raw syngas produced is then cooled to remove water and tars, and purified from CO_2, H_2S and hydrocarbons in the naphtha boiling range: the latter are hydrotreated and then blended into the gasoline pool or sold as BTX solvents. The purified syngas is sent to the FT reactors: the HTFT unit employs circulating fluidized bed reactors, while the LTFT unit adopts fixed bed reactors. The product effluent from the reactors is cooled and oil and water are condensed. While the aqueous phase is sent to the oxygenate recovery unit to produce alcohols and ketones, the hydrocarbon product is sent to the refining zone where valuable fuels are obtained. It is noteworthy to describe how the off gases from the different reactors are handled. The ones from the LTFT, being rich in syngas due to low conversions and a heavier product distribution for LTFT operations, are in part recycled directly to the fixed bed reactors. On the other hand, being the off gases from the HTFT

rich in light hydrocarbons, they are sent to the autothermal reforming (ATR) unit where recycle syngas is produced.

Shell Middle Distillate Synthesis (SMDS) Process

Shell has been the first company worldwide to build a GTL plant, targeting to the exploitation of the off-shore natural gas fields. Their first FT plant was constructed in Bintulu (Malaysia) in 1993 and produced 14700 [bpd] of liquid fuels.

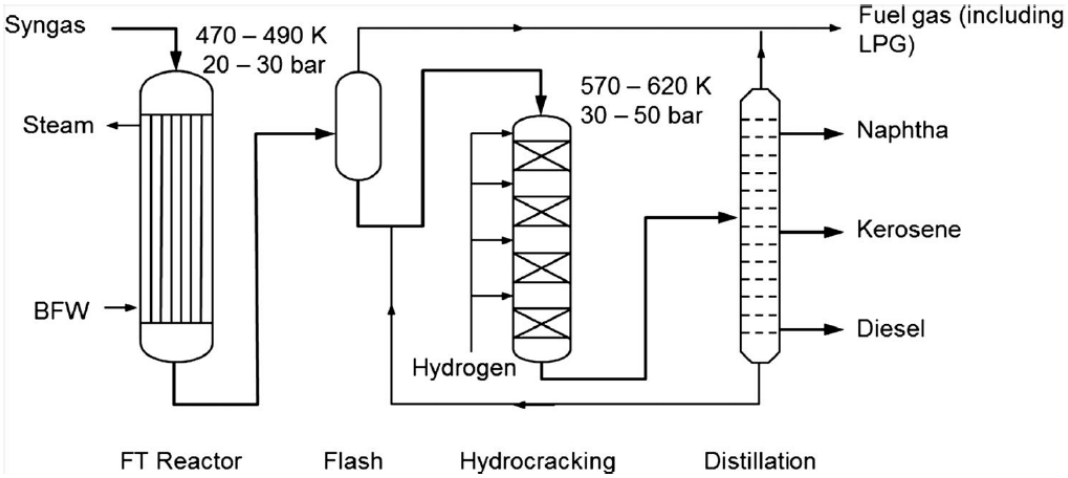

Figure 1.31: Simplified scheme of the SMDS process [41]

The syngas is produced via partial oxidation of methane with oxygen: being the H_2/CO ratio attained below the required stoichiometric value for FTS (1.7 vs 2.15), the syngas composition is adjusted by mixing it with the hydrogen-rich syngas obtained by catalytic steam reforming of the methane produced in the FT reactors [29]. The latter are multitubular fixed bed reactors containing over 10000 tubes filled with cobalt catalyst: this reactor and catalyst design, along with the low temperature, favour the production of waxes. The liquid product, after being separated from the light fractions, is heated up and sent to a mild hydrocracking unit. Here, transportation fuels are produced: the more severe the operating conditions in the hydrocracker, the lighter the product mixture. A subsequent distillation step separates the fuels according to their boiling range.

Pearl GTL

Developed by *Shell* and *Qatar Petroleum* and based in Ras Laffan Industrial City (Qatar), Pearl is the world's largest GTL plant [42]. It was built close to the world's largest single gas reserve, the North Field in the Arabian Gulf, whose estimated capacity is more than 900 [TCF] of gas, exploitable for about 100 years. The plant, started up in 2011, reached full production at the end of 2012 and today delivers 140 [kbpd] of product, despite its capacity of 260 [kbpd].

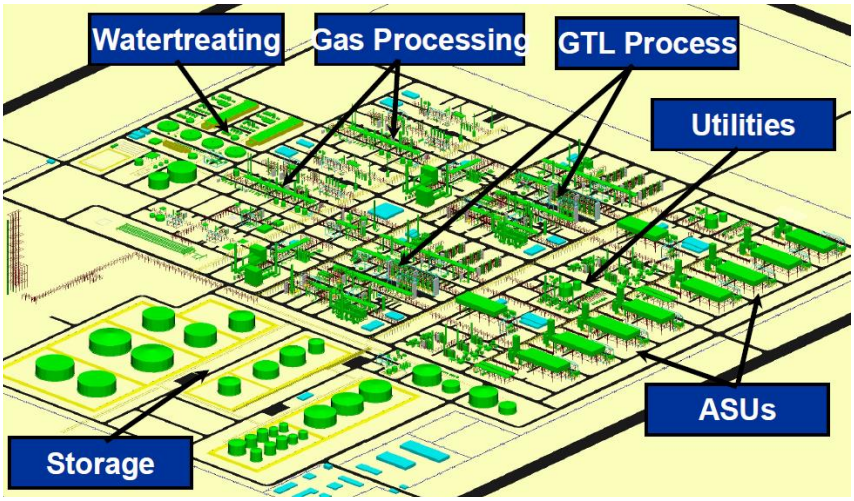

Figure 1.32: Pearl GTL project [43]

Syngas is produced via methane partial oxidation and is sent to the synthesis zone, which consists of 24 water-cooled multitubular fixed bed reactors, weighing 1200 [tons] each, filled with 30 ÷ 100 [tons] of Co-based catalysts supported on SiO_2. The FT products are then hydrocracked and isomerized to diesel, aviation fuels and lubricants.

Being the world's largest plant, its figures are impressive [44]: more than 40 distillation columns, about 2000 pumps and 50 compressors, 1000 online analysers and 14000 lab samples analysed per month.

Figure 1.33: Aerial view of Pearl GTL plant [42]

1.2.8.2 Processes based on unconventional reactors

Conventional GTL and CTL (coal-to-liquid) processes require very high capital investments, in the order of billions of US dollars [39]: in order to ensure a profitable operation over the plant lifetime, the production volumes must be at least about 30000 [bpd]. For this reason, these plants must be located close to sites which are very rich in fossil fuels reserves. The current distribution of natural gas reserves is however very scattered: very few are the large gas fields, whereas the number of small gas fields is increasing. In particular, only 6% of the gas reserves proven today would satisfy the lifetime capacity required by conventional GTL plants.

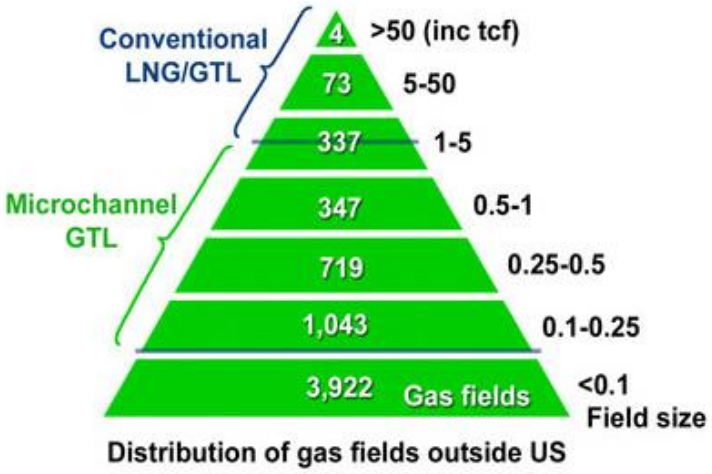

Figure 1.34: Worldwide distribution of natural gas reserves ([TCF] = Trillion Cubic Feet)

Today's process intensification aims to reduce plant size, thus reducing the capital cost while maintaining the economic feasibility. Such smaller plants have the potential to exploit the small gas field, enabling a cheaper transportation of more valuable liquid products from remote sites in the world. In addition, small scale GTL technology would provide an alternative to *flaring* in the oil refining industry, which is strictly regulated and severely taxed.

Using compact reactors, the plant size can be easily adjusted to the available volumes of feedstock. These reactors have a standard design and, once manufactured in the workshop, they are mounted over sledges: the transportation in this way is less challenging, especially when they are to be sent to remote areas or installed in already existing gas extraction/processing rigs.

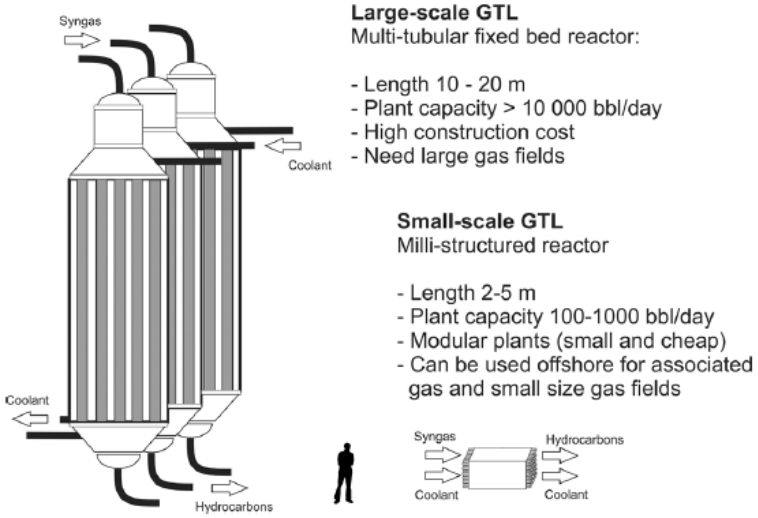

Figure 1.35: Comparison of large-scale and small-scale GTL reactors [39]

Velocys technology

Velocys Inc., headquartered in Ohio (USA), was the first company to launch on the market a novel technology which enables the exploitation of remote natural gas sources. This technology allows profitable operations of small scale FT plants, for volumes of production ranging from 1500 to 15000 [bpd]. Combining compact microchannel reactors and super-active catalysts, both fixed and variable costs are significantly reduced, compared to conventional GTL plants.

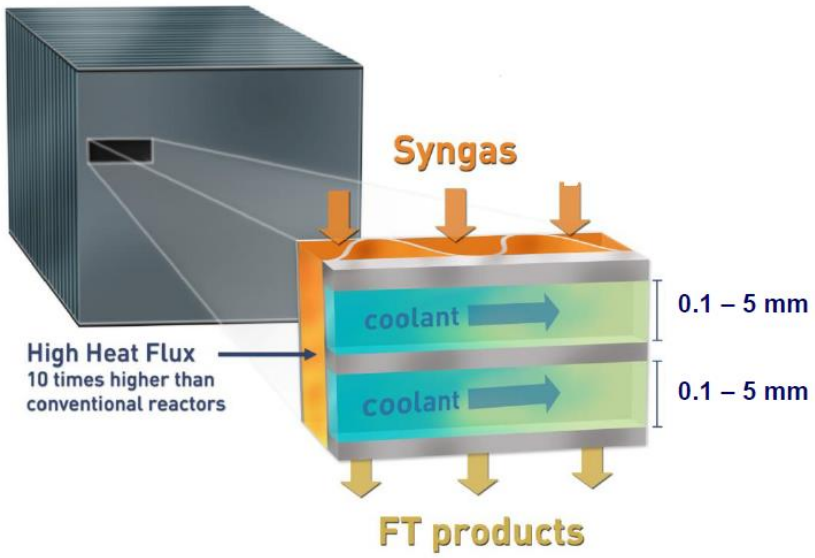

Figure 1.36: Microchannel reactor technology developed by *Velocys Inc.* [45]

In contrast with the multitubular fixed bed, the microchannel reactor has thousands of channels loaded with catalyst and interspersed with water cooling channels (Figure 1.36): the small channels provide a high surface which allows fast and efficient heat removal, enabling the use of highly active catalysts.

In particular, the company reports for such catalysts (Co-based) outstanding performances: conversions well above 90% and selectivity to liquid products over 87% in recycle configuration. Such performances, along with the efficient heat removal, make the small scale GTL technology profitable: currently *Velocys Inc.* is developing a plant [46] close to Ashtabula's harbour (Ohio, USA) aiming to produce 5000 [bpd] from the abundant reserves of Marcellus Shale, the largest natural gas field in the US.

CompactGTL technology

The target of the technology developed by *CompactGTL*, a British company headquartered in Abingdon (Oxfordshire, UK), is to exploit stranded reserves of natural gas producing *syncrude* (to be mixed with crude oil), which is a high value product of easy transportability. To pursuit this goal, two modular microchannel reactors are employed: the first converts natural gas into syngas, which is then converted to *syncrude* in the second reactor.

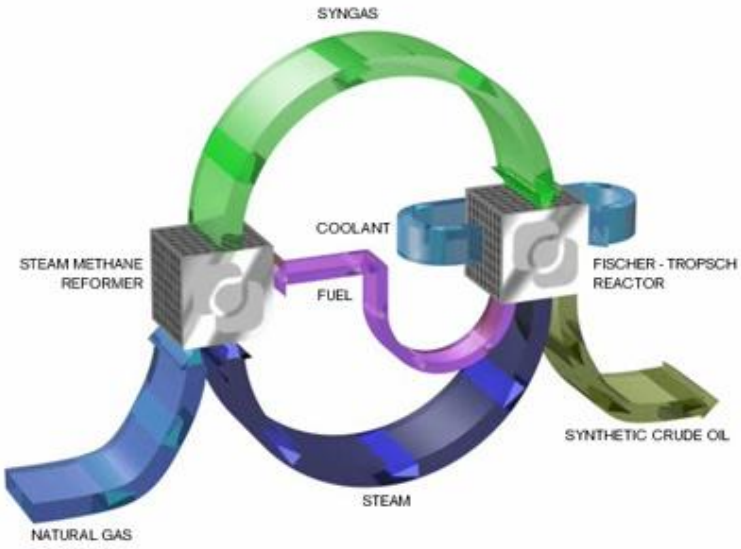

Figure 1.37: Production loop developed by *CompactGTL*

As shown in Figure 1.37, the water produced in the second reactor is purified and then sent to the first, where it reacts with natural gas forming syngas (SMR= *Steam Methane Reforming*). The unconverted syngas and gaseous fractions produced in the second reactor are burned "shell-side" in the first, providing the heat needed for the endothermic SMR to proceed. The main advantage is to have a self-sustaining plant, which does not require an air separation unit for oxygen production. In 2011, the first demonstration plant, commissioned by Petrobras, was built by *CompactGTL* in Aracaju (Brasil) and today produces 20 [bpd] of liquid products.

ENI-IFP technology

For some years until 2014, the catalysis group at *Politecnico di Milano*, in collaboration with *ENI* (*Ente Nazionale Idrocarburi*) and *IFP* (*Institut Français du Pétrole*) worked on structured multitubular reactors for Fischer-Tropsch synthesis. Enhanced heat removal and mass transfer, when compared to that of conventional packed bed reactors, are the key factors of this technology: metallic monoliths are employed due to their high thermal conductivity. In 2012, tests carried out on the monolith reactors showed very promising results: the group, in fact, performed a feasibility study for a demonstration plant with 20 [bpd] capacity. Unfortunately, the recent collapse in oil prices led these oil-and-gas companies to stall the investments in the project.

Bibliography Chapter 1

[1] "Organisation for Economic Co-operation and Development." [Online]. Available: https://en.wikipedia.org/wiki/Organisation_for_Economic_Co-operation_and_Development.

[2] British Petroleum, "BP Statistical Review of World Energy June 2016."

[3] Exxon Mobil, "The 2016 outlook for energy: a view to 2040," 2016.

[4] "Toyo Engineering Corporation: GTL (Gas to Liquids)." [Online]. Available: http://www.toyo-eng.com/jp/en/products/energy/gtl/.

[5] C. G. Visconti and P. Forzatti, "Studi e sperimentazione del processo di produzione di combustibili liquidi da carbone," 2011.

[6] R. Guettel, U. Kunz, and T. Turek, "Reactors for Fischer-Tropsch synthesis," *Chemical Engineering and Technology*, vol. 31, no. 5. pp. 746–754, 2008.

[7] C. H. Bartholomew, "History of cobalt catalysts design for FTS," *AIChE Natl. Spring Meet.*, p. 83b, 2003.

[8] National Engergy Technology Laboratory, J. F. Goellner, V. Shah, M. J. Turner, N. J. Kuehn, J. Littlefield, G. Cooney, and J. Marriott, "Analysis of Natural Gas-to Liquid Transportation Fuels via Fischer-Tropsch," *U.S. Dep. Energy*, p. 101, 2013.

[9] B. Y. F. Morales and B. M. Weckhuysen, "Promotion Effects in Co-based Fischer – Tropsch Catalysis," *R. Soc. Chem.*, vol. 19, no. 1, pp. 1–40, 2006.

[10] M. De Beer, A. Kunene, D. Nabaho, M. Claeys, and E. Van Steen, "Technical and economic aspects of promotion of cobalt-based Fischer-Tropsch catalysts by noble metals – a review," vol. 114, no. October 2013, pp. 14–16, 2014.

[11] J. A. Moulijn, M. Makkee, and A. E. Van Diepen, *Chemical Process Technology*, Second Ed. Wiley, 2013.

[12] E. Tronconi, "Lecture 8: Fischer-Tropsch Synthesis." Course of Industrial Organic Chemistry, Politecnico di Milano, 2015.

[13] H. Schulz, "Major and minor reactions in Fischer – Tropsch synthesis on cobalt catalysts," *Top. Catal.*, vol. 26, no. December, pp. 73–85, 2003.

[14] P. Winslow and A. T. Bell, "Application of transient response techniques for quantitative determination of adsorbed carbon monoxide and carbon present on the surface of a ruthenium catalyst during Fischer-Tropsch synthesis," *J. Catal.*, vol. 86, no. 1, pp. 158–172,

1984.

[15] E. Iglesia, S. C. Reyes, and R. J. Madon, "Transport-enhanced α-olefin readsorption pathways in Ru-catalyzed hydrocarbon synthesis," *Journal of Catalysis*, vol. 129, no. 1. pp. 238–256, 1991.

[16] M. E. Dry, "Practical and theoretical aspects of the catalytic Fischer-Tropsch process," *Appl. Catal. A Gen.*, vol. 138, pp. 319–344, 1996.

[17] H. Pichler and H. Buffleb, "Synthesis of Paraffin Wax on Ruthenium Catalysts at Pressures up to 100 Atmospheres," *Brennstoff-Chem*, vol. 21, pp. 257–264, 1940.

[18] I. Wender, H. W. Sternberg, and M. Orchin, "Chemistry of the Metal Carbonyls. I. New Concepts Applied to Carbonyls of Cobalt," *J. Am. Chem. Soc.*, vol. 74, pp. 1216–1219, 1952.

[19] E. Van Steen and H. Schulz, "Polymerisation kinetics of the Fischer – Tropsch CO hydrogenation using iron and cobalt based catalysts," *Appl. Catal. A Gen.*, vol. 186, pp. 309–320, 1999.

[20] S. Shetty, A. P. J. Jansen, and R. A. Van Santen, "Direct versus Hydrogen-Assisted CO Dissociation," *J. Am. Chem. Soc.*, no. 131 (36), pp. 12874–12875, 2009.

[21] A. A. Adesina, "Hydrocarbon synthesis via Fischer-Tropsch reaction : travails and triumphs," *Appl. Catal. A Gen.*, vol. 138, pp. 345–367, 1996.

[22] M. Ojeda, R. Nabar, A. U. Nilekar, A. Ishikawa, M. Mavrikakis, and E. Iglesia, "CO activation pathways and the mechanism of Fischer – Tropsch synthesis," *J. Catal.*, vol. 272, no. 2, pp. 287–297, 2010.

[23] J. Flory, "Molecular Size Distribution in Linear Condensation Polymers," vol. 1, no. 7, 1936.

[24] R. B. Anderson and R. A. Friedel, "Composition of Synthetic Liquid Fuels. I. Product Distribution and Analysis of C5-Cs Paraffin Isomers from Cobalt Catalyst," vol. 72, no. 1940, pp. 1212–1215, 1949.

[25] G. P. van der Laan and A. A. C. M. Beenackers, "Kinetics and Selectivity of the Fischer-Tropsch Synthesis: A Literature Review," *Catal. Rev. Sci. Eng.*, vol. 41, no. 3–4, pp. 255–318, 1999.

[26] O. O. James, B. Chowdhury, M. Adediran, and S. Maity, "Advances Reflections on the chemistry of the Fischer – Tropsch synthesis," *RSC Adv.*, vol. 2, pp. 7347–7366, 2012.

[27] R. M. De Deugd, "Fischer-Tropsch Synthesis Revisited; Efficiency and Selectivity Benefits

from Imposing Temporal and/or Spatial Structure in the Reactor," Doctoral thesis, TU Delft, The Netherlands, 2004.

[28] L. Fratalocchi, "Preparazione e analisi di reattività di un catalizzatore eggshell Co/Al2O3 per la sintesi di Fischer-Tropsch," Master Thesis, Politecnico di Milano, 2013.

[29] M. E. Dry, "The Fischer – Tropsch process : 1950 – 2000," *Catal. Today*, vol. 71, pp. 227–241, 2002.

[30] B. W. Wojciechowski, "The Kinetics of the Fischer-Tropsch Synthesis," *Catal. Rev.*, vol. 30, no. 4, pp. 629–702, 1988.

[31] T. J. Donnelly, I. C. Yates, and C. N. Satterfield, "Analysis and Prediction of Product Distributions of the Fischer-Tropsch Synthesis," *Energy & Fuels*, vol. 2, no. 6, pp. 734–739, 1988.

[32] E. Kuipers, I. H. Vinkenburg, and H. Oosterbeek, "Chain Length Dependence of α-Olefin Readsorption in Fischer-Tropsch Synthesis," *Journal of Catalysis*, vol. 152, no. 1. pp. 137–146, 1995.

[33] E. Iglesia, "Design, synthesis, and use of cobalt-based Fischer-Tropsch synthesis catalysts," *Appl. Catal. A Gen.*, vol. 161, pp. 59–78, 1997.

[34] E. Iglesia, "Design, synthesis, and use of cobalt-based Fischer-Tropsch synthesis catalysts," *Appl. Catal. A Gen.*, vol. 161, no. 1–2, pp. 59–78, 1997.

[35] Erkey, Rodden, and Akgerman, "Diffusivities of synthesis gas and n-alkanes in Fischer-Tropsch wax," *Energy and Fuels*, vol. 4, no. 3, pp. 275–276, 1990.

[36] H. Song, D. Ramkrishna, S. Trinh, and H. Wright, "Operating Strategies for Fischer-Tropsch Reactors : A Model-Directed Study," *Korean J. Chem. Eng.*, vol. 21, no. 2, pp. 308–317, 2004.

[37] E. W. W. Kuipers, C. Scheper, J. H. H. Wilson, I. H. H. Vinkenburg, and H. Oosterbeek, "Non-ASF product distributions due to secondary reactions during Fischer-Tropsch synthesis," *J. Catal.*, vol. 158, no. 158, pp. 288–300, 1996.

[38] D. Leckel and H. Tropsch, "Upgrading of Fischer-Tropsch Products to Produce Diesel," *Haldor Topsøe Catal. Forum*, 2010.

[39] B. Todić, V. V. Ordomsky, N. M. Nikačević, A. Y. Khodakov, and D. B. Bukur, "Catalysis Science & Technology Opportunities for intensification of Fischer – Tropsch over cobalt catalysts in microreactors," *Catal. Sci. Technol.*, vol. 5, pp. 1400–1411, 2015.

[40] B. Jager and R. Espinoza, "Advances in low temperature Fischer-Tropsch synthesis," *Catal.*

Today, vol. 23, no. 1, pp. 17–28, 1995.

[41] "Gas-to-liquids projects gaining momentum as process list grows - Oil & Gas Journal." [Online]. Available: http://www.ogj.com/articles/print/volume-95/issue-25/in-this-issue/gas-processing/gas-to-liquids-projects-gaining-momentum-as-process-list-grows.html.

[42] "The world's largest GTL plant - Shell Global." [Online]. Available: http://www.shell.com/about-us/major-projects/pearl-gtl/the-world-s-largest-gas-to-liquids-plant.html.

[43] A. Hoek, "The Shell GTL process: Towards a world scale project in Qatar," *Chemie-Ingenieur-Technik*, vol. 77, no. 8, p. 1172, 2005.

[44] A. Holmen, "Lecture 4: Fischer-Tropsch Synthesis." Course of Petrochemistry and Oil Refining, NTNU (Norwegian University of Science and Technology), 2015.

[45] S. C. LeViness, "Velocys Fischer-Tropsch Synthesis Technology - New Advances on the State of the Art Who is Velocys," *Oxford Catal.*, pp. 1–32, 2013.

[46] "Velocys - Projects." [Online]. Available: http://www.velocys.com/projects_overview.php.

Chapter 2 – State of the Art of Co/γ-alumina catalysts

The optimization of the FT process is strictly related to further improvements in catalysts performances, mainly through a better exploitation of the cobalt active phase. This requires enhanced dispersion on the support and higher reducibility and stability. In this chapter, an overview on the main investigations in the literature will be given in order to better understand scientific developments and ideas that led to different solutions.

It is well established that catalyst activity is directly proportional to the number of active sites. In Co-based catalysts these are made of metallic Co on the surface. Better dispersion of the catalyst leads to an increased number of active sites and thus better catalytic performances. The first and relatively straightforward solution is to deposit the active phase on a highly porous support (e.g. SiO_2, Al_2O_3, TiO_2) to facilitate metallic dispersion. Furthermore, a strongly interacting support can be chosen to improve the dispersion via metallic-support interactions; however, strong Co-support interactions, as it occurs in the case of alumina and titania, favor the dispersion of the supported Co particles but decrease their reducibility leading to catalyst materials with a limited number of accessible surface Co metal sites. This is due to the formations of metal-support bonds, often reported to be in the form of cobalt-aluminates ($CoAl_2O_4$), that are more difficult to be reduced.

Active phase deposition pathway influences the Co structure and catalytic activity as a consequence. Typically, Co/Al_2O_3 catalyst is prepared via impregnation of the active phase solution followed by drying, calcination and reduction. Despite the ease of reproducibility of this technique, crystallite structure is highly influenced by the nature of the precursor as well as solvent, pH of the impregnating solution and operating conditions of the calcination and reduction steps.

Several studies are reported in literature with the aim of improving supported catalyst activity and many of them prove the important role of a small addition of noble metals in the catalyst formulation. The function of the noble metal promoter is to enhance the reducibility of Co-species to obtain higher quantities of metallic Co (Co^0), the active species in FTS. It is thought that promoters facilitate H_2 dissociation, that is the slow step of reduction processes [1]. *Vada et al.* [2]

also demonstrated that the intrinsic activity of the active phase is not affected upon promoter addition.

Another concern to take into account is catalyst stability, mainly for the presence of water, produced during FTS in big amounts, that may lead to changes in the catalytic structure. According to *Jacobs et al.* [3], who studied the effect of water on a Pt-promoted Co/Al_2O_3 catalyst, water was found to influence FTS rates in two regimes. At water partial pressures below 25% by volume, the catalytic activity decreased reversibly; however, at higher water partial pressures, changes in the cobalt structure were readily observed as the formation of cobalt aluminate-like species were suggested to be formed.

With the intent of summarizing the main hints given in the literature [4], an efficient Co-based catalyst should be designed in such a way that it has:

- High active sites density
- Optimized sites distribution on the support surface
- Optimal crystallites dimensions
- Low fraction of hardly reducible Co-compounds (e.g. cobalt-aluminates)
- High stability
- Affordable cost

2.1 Effects of Co^0 crystallite size and dispersion

Dimension and dispersion of the cobalt active phase have a significant effect on the performance of FT catalysts. Given the cobalt load, dimension and dispersion influence one another with opposite trends; the lower the dimension, the higher the dispersion and vice-versa. By plotting the activity performances in function of Co-crystallite size, a maximum can be observed; activity significantly decreases with very small or very big Co clusters. As it often happens in science, when a maximum is observed the explanation can be related to the competition between two different phenomena. In this specific case, crystallite dimensions play a role both during reduction and reaction. The first process, reduction, works better with larger crystallites as long as they show less interactions with the support and are consequently easier to be reduced. On the other hand, during catalyst testing, a widespread dispersion of small Co^0 particles provides a higher number of active sites and hence

higher activity per unit of mass. Summarizing, larger crystallites facilitate reduction but limit the catalytic activity. Conversely, smaller crystallites show hindered reduction but improved catalytic performances.

The first studies on this topic were performed by *Reuel et al.* [5] and *Lisitsyn et al.* [6] and later confirmed by *Iglesia et al.* [7]. They all show a sensitive increase in the catalytic activity when crystallite size goes from 200 to 9 [nm]. Furthermore, *Iglesia* demonstrates how the specific activity, often referred to as *Turnover Frequency (TOF)*, is not influenced by crystallite dimensions, at least for values higher than 9 [nm]. Conversely, with dimensions below 9 [nm] a dramatic decrease in activity is observed: most authors ascribe this behavior to the low reducibility of the small cobalt clusters, others [6 - 7] suggest carbide formation and structure sensitivity to be the major causes. The determination of an optimal dimension for cobalt crystallites is still a debated topic amongst researchers; *Bezemer et al.* [10] studied the effect of the crystallite dimension testing cobalt catalyst supported on an inert substrate (carbon nanofibers, CNF), so as to decouple the problem of strong support interactions with the active phase, at 1 [bar] and 35 [bar]; they found at both pressures volcano-like curves, whose maxima were pointed at 6 [nm] and 8 [nm], respectively.

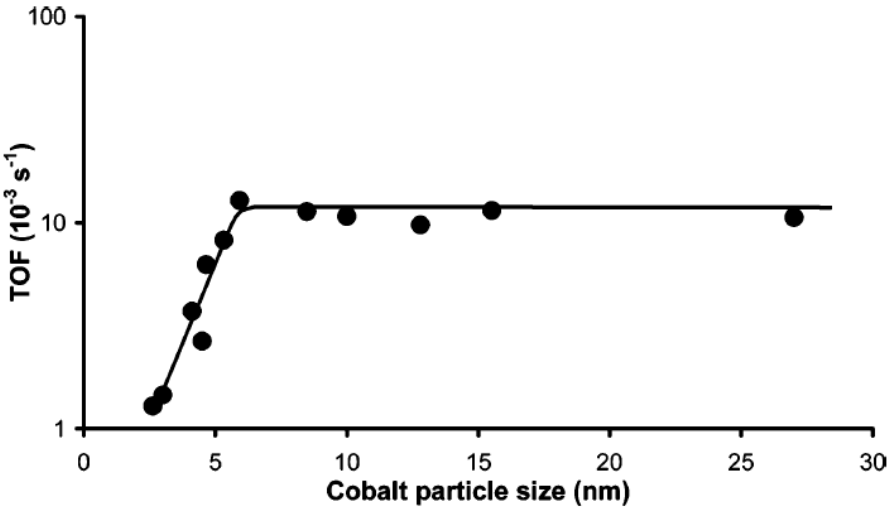

Figure 2.1: Influence of cobalt particle size on TOF (1 [bar]) [10]

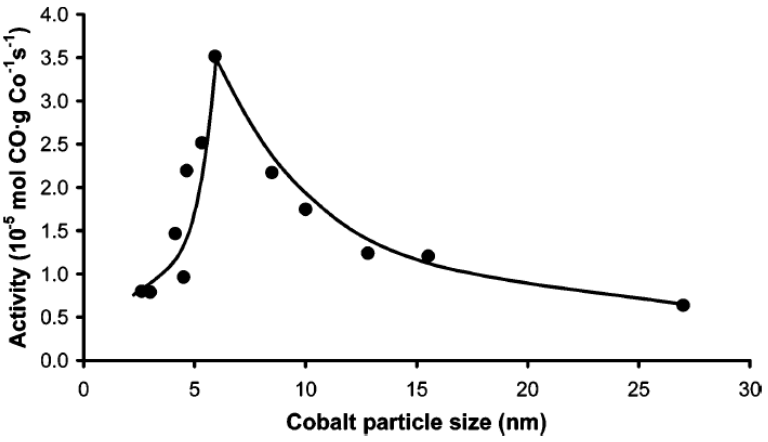

Figure 2.2: Influence of cobalt particle size on activity, normalized on the Co loading (1 [bar]) [10]

The trend found by the authors at 1 [bar] (Figure 2.1 and Figure 2.2) was consistent with their experiments (black dots) run at commercially relevant FT conditions and with data taken from *Iglesia et al.* (gray squares) [7]:

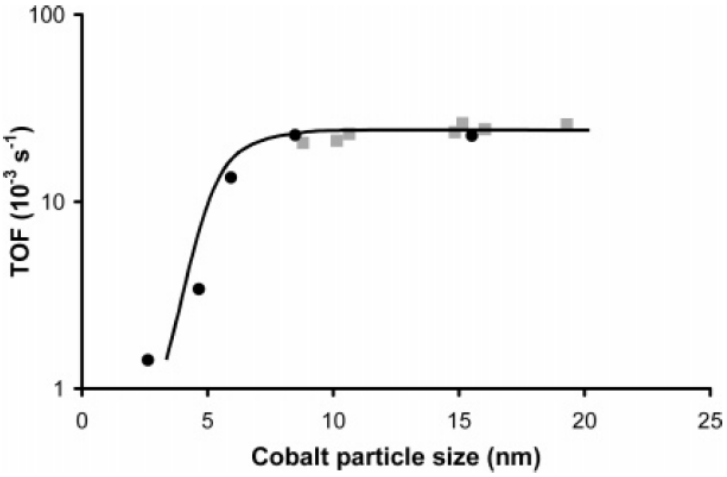

Figure 2.3: Influence of cobalt particle size on TOF (35 [bar]) [10]

Cobalt particle size also influences product distribution. *Borg* et al. [11] investigated the relationship between the dimension of cobalt crystallites and the selectivity towards long chain

hydrocarbons (C_{5+}). Crystallite dimensions in the range 3 ÷ 18 [nm] have been investigated over 26 samples supported on both γ-Al_2O_3 and α-Al_2O_3.

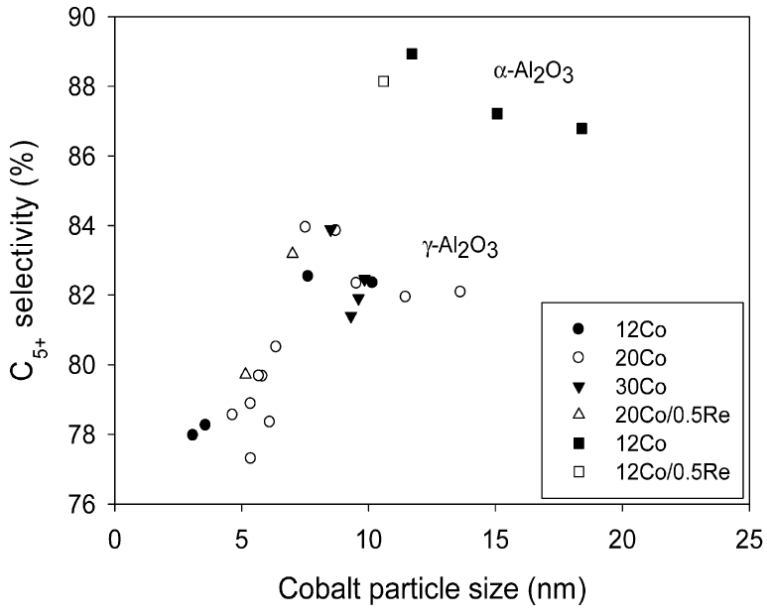

Figure 2.4: Influence of cobalt particle size on C_{5+} selectivity [11]

The C_{5+} selectivity profile, obtained for the same values of conversion, shows once again a maximum around 8 [nm] for catalysts supported on γ-Al_2O_3 and around 12 [nm] for α-Al_2O_3 supported catalysts. The results are consistent with earlier studies published by the same authors [12] and by *Bezemer et al.* [10]. The differences obtained with the two supports can be ascribed to different chemical properties of the surface.

The traditional approach used for catalyst preparation (impregnation, drying, calcination, reduction) leads to a broad crystallite size distribution. Since activity in FTS is crystallite-size dependent, an analysis of the relationship between crystallite dimension and catalyst activity based on average cluster dimensions results to be inaccurate. This last considerations, leads *Breejen et al.* [13] to identify another optimal crystallite size about 4.7 ± 0.2 [nm], stressing the fact that a narrow size distribution is crucial for the higher activity. However, experiments show that very small clusters (e.g. < 2 ÷ 4.4 [nm]) are subjected to re-oxidation by water as they are thermodynamically unstable at typical FTS conditions [14]. Oxidized clusters have a weaker interaction with the support and tend to sinter, thus forming aggregates of bigger dimensions: these generate an attractive force

towards smaller metallic Co-clusters, which is strong enough to make them coalesce with bigger clusters (*Ostwald ripening phenomenon).*

In conclusion, cobalt crystallites have to be small enough to maximize dispersion and active sites density, but at the same time large enough to be easily reduced and stable with respect to re-oxidation and sintering.

2.2 Incipient Wet Impregnation (IWI) and precursor choice: nitrate, acetate and organic solvent

Incipient Wet Impregnation (IWI) is the usual method for FT Co-based catalyst preparation, starting from a solution of cobalt salts (usually cobalt nitrate) with pH values between 2 and 3. Main factors affecting the adoption of cobalt nitrate salts are low costs, high Co loads per single impregnation step and a relatively easy ligand removal. At such low pH values, interaction between the positively charged support and the cat-ion Co is modest; until the completion of the drying process, the majority of soluble Co keeps its mobility on the surface. Redistribution of Co particles during the drying process and the agglomeration during calcination lead to low metal dispersion and a wide cluster size distribution.

In order to better design the catalysts, one first approach could stand in the choice of a different precursor since it has a dramatic effect on activity and selectivity. In their studies on SiO_2 supported catalysts, *Sun et al.* [15] demonstrate how, opposite from nitrate, Co-acetate as a precursor leads to a high dispersion of Co_3O_4 species: however, the latter are difficult to be reduced due to strong Co-support interactions. For this reason, a mixture of the two precursor is proposed by the same authors so that metallic sites derived from Co-nitrate, obtained at lower temperatures, facilitate the reduction of smaller oxide clusters from Co-acetate. XRD spectra show that smaller crystallites can be obtained with respect to the usual preparation. The best trade-off between reducibility and dispersion is obtained with a weight ratio of 1 (Table 2.1); the activity test shows significant improvements.

Table 2.1: Catalytic behaviors of various Co/SiO_2 catalysts for CO hydrogenation [15]

Catalyst	CO conversion (%)	CH_4 selectivity (%)	CO_2 selectivity (%)
10N	29.8	6.58	1.64
3N/7A	21.3	6.25	0.65
5N/5A	42.5	6.27	1.82
7N/3A	30.8	6.08	0.98
5A/5N	31.3	6.65	1.19
5A+5N	33.5	8.89	1.27
10A	6.2	7.62	1.63

The decomposition of the precursor represents an important step in the catalyst preparation. In particular, the heat released during decomposition can have a massive influence on the structure of Co-species. This aspect, along with effects on dispersion and reducibility, has been thoroughly investigated for Co/SiO_2 catalysts by *Girardon et al.* [16]. The thermal decomposition of Co-nitrate is weakly endothermic and complies with the following stoichiometry, previously proposed by *Cseri et al.* [17]:

$$3[Co\,(NO_3)_2 \cdot 6H_2O] \rightarrow Co_3O_4 + 6NO_2 + O_2 + 18H_2O \qquad (2.1)$$

On the other hand, the decomposition of Co-acetate is strongly exothermic. As formerly shown by *Poul et al.* [18], the strong exothermicity is due to an autocatalytic oxidation triggered by the generation of the Co-oxide:

$$3[Co\,(CH_3COO)_2 \cdot 4H_2O] + 12.5O_2 \rightarrow Co_3O_4 + 12CO_2 + 21H_2O \qquad (2.2)$$

Figure 2.5 shows that Co-nitrate decomposition occurs at 423 [K] while Co-acetate decomposes at slightly higher temperatures, about 493 [K]. Endothermic decomposition favors the formation of Co_3O_4 crystallites, on the other hand highly exothermic decomposition leads to the formation of high Co-silicate fractions, difficult to be reduced but well dispersed. It is also observed that calcination procedure has an active role in determining the decomposition temperature itself. A decomposition under mild and controlled conditions leads to a shift of the reduction peaks towards lower temperatures: in this way, both Co-silicates concentrations and Co_3O_4 crystallite dimensions can be reduced.

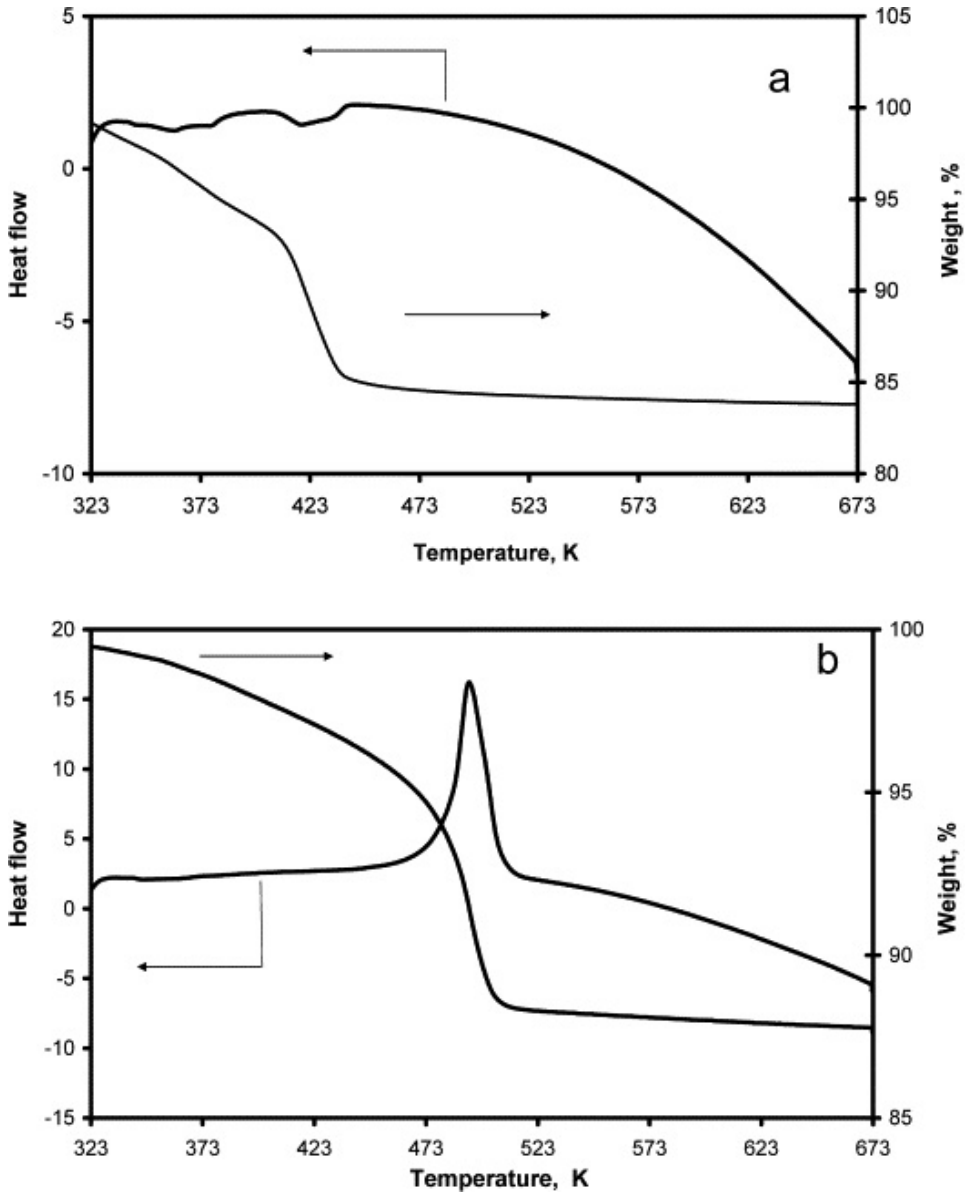

Figure 2.5: DSC-TGA curves of SiO2-supported cobalt nitrate (a) and acetate(b) [16]

Catalyst produced with Co-acetate as precursor show lower activity performances due to a higher Co-silicate concentration that implies lower reaction rates. Nevertheless, the activity of these systems can be adjusted with an accurate control of the decomposition conditions; for example, the addition of a promoter can change significantly the decomposition mechanisms. Summarizing, a compromise between dispersion and degree of reduction is observed in Co-acetate catalysts, while large crystallites are observed when Co-nitrate is used as a precursor.

An alternative way to increase dispersion is the addition of an organic compound that may form stable complexes with Co^{2+}, thus modifying its interactions with the support. As an example, SiO_2 shows surface groups, such as silanol groups (SiOH), which strongly interact with the cobalt oxides, hindering their reducibility. Treating the support surface with functional organic groups (e.g. CH_3-SiO_2, $(CH_3)_2$-SiO_2 and $(CH_3)_3$-SiO_2), reduces the concentration of the SiOH groups: as a consequence, the strong Co-support interactions are weakened, resulting in higher reducibility and increased FT activity [19].

Another example of increased FT activity by adding an organic compound in the impregnating solution is shown in the work of *Koizumii et al.* [20]. SiO_2 supported cobalt catalysts are prepared adding ethylene glycol (EG) and the similar DEG (diethylene glycol) and TEG (triethylene glycol), with different glycol/Co^{2+} molar ratios, to the Co-nitrate solution. TPR and chemisorption analysis have been performed on the prepared catalysts to study the effects of glycol addition in terms of activity, selectivity, reducibility, and Co dispersion. Table 2.2 shows how Co^0 dimensions can be controlled in a 6-30 [nm] interval by adopting different glycol types. For each glycol employed, degrees of reduction higher than 95% are granted. The activity increase depends on the glycol/Co^{2+} ratio with an optimal value, which depends on the precursor.

Table 2.2: Effect of glycol addition on catalyst reducibility, Co0 dispersion and TOF [20]

Catalyst	**Co reduction [%]**	**Chemisorbed H_2 [μmol·gcat^{-1}]**	**Co^0 dispersion [%]**	**Co^0 crystallite diameter [nm]**	**TOF [10^{-3} s^{-1}]**
Co(20) –TEG(1.0)/SiO_2	95	154	12	8.0	149
Co(20) –TEG(0.5)/SiO_2	98	172	13	7.4	141
Co(20) –TEG(0.25)/SiO_2	99	164	12	7.9	148
Co(20) –TEG(0.125)/SiO_2	99	78	5.9	16.0	114
Co(20) –EG(1.0)/SiO_2	>99	190	14	7.8	131
Co(20) – SiO_2	>99	42	3.2	30.0	118

As shown in Table 2.2, the chain growth probability (α) decreases using TEG with respect to the catalyst obtained via nitrate Co(20)/SiO_2. This may suggest that TEG formulations lead to smaller

crystallites, which are responsible of the lower C_{5+} selectivity. Despite decreasing chain growth probability, productivities appear to increase.

Table 2.3: Effect of TEG addition on product selectivities, chain growth probability and productivity for Co(20)/SiO2 catalysts [20]

Catalyst	Selectivity [C – mol%]					α	Productivity [g·kg$_{cat}^{-1}$·h^{-1}]	
	CH_4	C_{2-4}	C_{5-9}	C_{10-20}	C_{21+}		C_{5+}	C_{10-20}
Co(20) –TEG(1.0)/SiO_2	14	7	35	37	7	0.81	1328	616
Co(20) –TEG(0.5)/SiO_2	13	12	41	31	3	0.79	1415	587
Co(20) –TEG(0.25)/SiO_2	10	18	28	37	7	0.82	1590	825
Co(20) –TEG(0.125)/SiO_2	16	6	29	42	6	0.83	386	209
Co(20) – SiO_2	15	5	24	44	12	0.85	302	167

Gonzàlez-Cortéz et al. [21], report advantages from addition of urea (UMxC *Urea Matrix Combustion)* during catalyst preparation. Urea favors the formation of highly active and well dispersed metallic species on *Ni-MoS_2 / γ-Al_2O_3* catalysts, used in hydrodesulphurization processes. This new methodology is based on the combustion auto-propagation effect and requires low ignition temperatures for the reaction between the precursor salt and the organic matrix in an exothermic reaction. The crystallite size is governed by the combustion process, which does not leave enough time for the crystallites to grow.

2.3 Promoter addition

Promoters are agents added to the catalyst materials to improve both stability and catalytic performances.

According to the different ways of inducing beneficial effects, promoter elements can be conveniently divided in three main categories:

- Structural promoters, which act on the cobalt-support interactions thus influencing the metal dispersion;
- Stabilizers, added to prevent catalyst deactivation;

- Electronic promoters, which are able to reduce the energetic barrier associated to the reaction steps; the electronic promotion occurs via ligand effect, thus altering the environment of an active Co site. It can only occur when there is a direct chemical interaction between promoter element and the cobalt active phase

Noble metals such as Pt, Re, Ru and Pd are the most widely used promoters in FT synthesis. Their ability to enhance cobalt dispersion by acting on oxide cobalt reducibility is well established with the consequence of increased catalytic performances. By testing Co-based catalyst promoted with such noble metals, *Diehl and Khodakov* [4] reported higher reaction rates, up to 8 times more than the one observed ones with the unpromoted catalyst.

The enhanced cobalt dispersion with promoted catalysts is mainly due to a lower average crystallite size. Increased reducibility given by the promoter also allows the smaller crystallites to be reduced as well, thus resulting in enhanced dispersion and lower average crystallite size.

The formation of preferential bonds between electronic noble metal promoters and cobalt atoms has been reported by different researchers [22]. Noble metal atoms are built-in the cobalt particles either during calcination or during the reduction process, as shown in Figure 2.6.

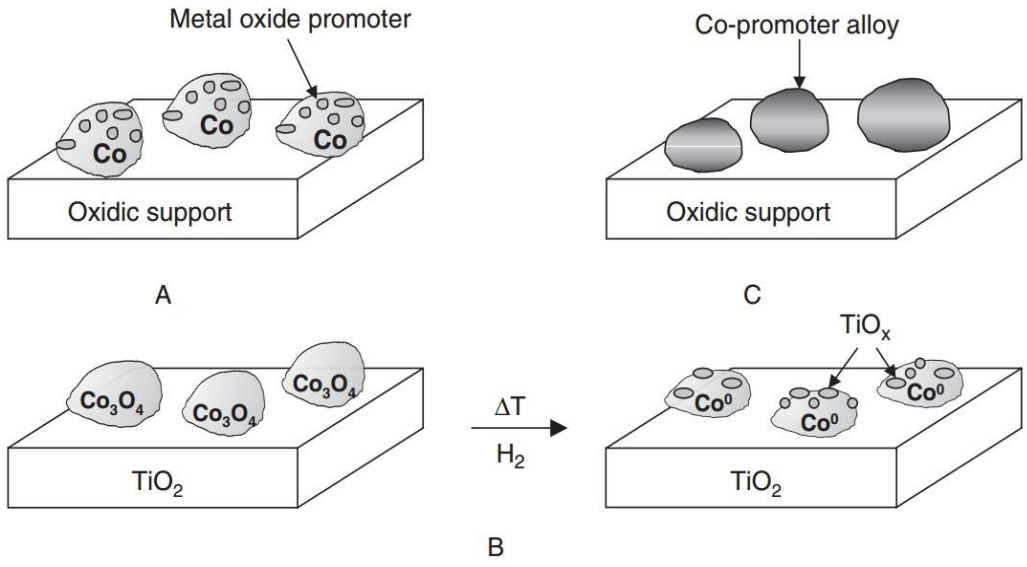

Figure 2.6: The different modes of action of electronic promoters in Co-based FT catalysts: (A) promoter metal oxide decoration of the cobalt surface; (B) the SMSI (Strong Metal-Support Interaction) effect; and (C) cobalt-promoter alloy formation [22]

These bimetallic particles change the electronic properties of the superficial Co-atoms thus influencing activity, selectivity and stability of the catalyst.
Moreover, *Morales and Weckhuysen* [22] report that noble metals avoid, or at least limit, the formation of cobalt-support bonds thus increasing the turnover frequency.

2.3.1 Platinum promotion effect

Platinum is one of the most studied promoters along with rhenium and ruthenium. The first investigations date back to the early 90's, when *Zsoldos et al.* [23] noticed a significant increase in reducibility for γ-Al_2O_3–supported catalysts upon the addition of small amounts of platinum (1.5 wt.%). Since then, the research on Pt-promoted Co-based catalysts has continued growing. Today, studies on platinum promotion have reached a high level of detail, both in terms of catalyst characterization and performances. In particular, the attention is mainly focused on platinum loading and deposition order, which will be further analyzed in the following chapters.
The definition of an optimal platinum load comes from a trade-off between costs and performances, as the price of platinum is almost 1000 times higher than cobalt, thus being of great impact on the economic balance of the whole process [4].
The strong interaction between the cobalt active phase and the support, mentioned in the previous paragraph has a dual effect. On the one hand, it limits sintering and enhances the dispersion of cobalt particles, but on the other hand, it limits their reducibility. In order to avoid this drawback, a promoter is required to improve performances in the reduction phase.
It is well established that Pt-promoted catalysts show a significant improvement in catalytic performances with respect to the corresponding unpromoted. This is mainly due to an increase in the number of active sites rather than a direct catalytic effect, since promoter elements are not considered themselves to be catalytically active [24]: they operate during reduction rather than reaction. By increasing the extent of reduction of Co-oxides, they allow a better exploitation of the cobalt load, enhancing the available fraction of active cobalt species during reaction (Co^0).
Promotion of cobalt-based catalysts also affects the dispersion of cobalt particles [25] due to a higher concentration of cobalt sites [26]. A higher number of active sites actually results in a higher number of cobalt crystallites, thus a smaller average size and higher dispersion. *Jacobs et al.* [27]

studied promoted catalysts with a high platinum load (0.5-5.0 wt. %): they noticed a significant influence of Pt addition on the average crystallite dimension.

Table 2.4: Average crystallite diameter as a function of Pt loading [27]

Catalyst	Average crystallite diameter [nm]
25%Co/Al_2O_3	14.6
0.5%Pt–25%Co/Al_2O_3	10.0
1.0%Pt–25%Co/Al_2O_3	8.8
2.0%Pt–25%Co/Al_2O_3	8.1
3.0%Pt–25%Co/Al_2O_3	7.4
4.0%Pt–25%Co/Al_2O_3	7.2
5.0%Pt–25%Co/Al_2O_3	6.3

The addition of 1.0 wt. % of Pt makes the crystallite diameter to downsize from 14.6 [nm] to 8.8 [nm]. With a Pt load up to 5.0 wt. %, average particle diameter reaches 6.3 [nm].

Platinum's ability to catalyze the reduction of cobalt oxides has been attributed to two main mechanisms:

- Electronic/ligand effects arising from Pt-Co coordination
- High affinity for H_2 activation (i.e. adsorption and dissociation)

2.3.1.1 Pt-Co ligand effects

Zsoldos et al. [23] ascribes the increased Co/Al_2O_3 reducibility to platinum's ability to hinder the formation of mixed cobalt-support species, namely $CoAl_2O_4$, thanks to Pt-Co bonds. It is well established in literature that Pt tends to create Pt-Co bonds more than Pt-Pt bonds. According to *Khodakov et al.* [28], promotion of Co catalyst with noble metals may lead to the direct interaction between cobalt and promoter, either during oxidative treatments or during reduction, with formation of bimetallic particles. As *Davis et al.* [29] observed by XANES (*X-Ray Absorption Near Edge Structure*) and EXAFS (*Extended X-Ray Absorption Fine Structure*) spectroscopy, in such particles cobalt is directly bonded to the noble metal. The EXAFS Fourier transform moduli of a platinum foil and of the reduced cobalt catalyst promoted with Pt are different. The peak in the Fourier transform moduli of the cobalt catalyst is situated at 2.1 [Å]. The peak at 2.1 [Å] observed in the

profile of the reduced Co catalyst promoted with Pt (Figure 2.7), can be attributed to Pt-Co coordination in the metallic phase.

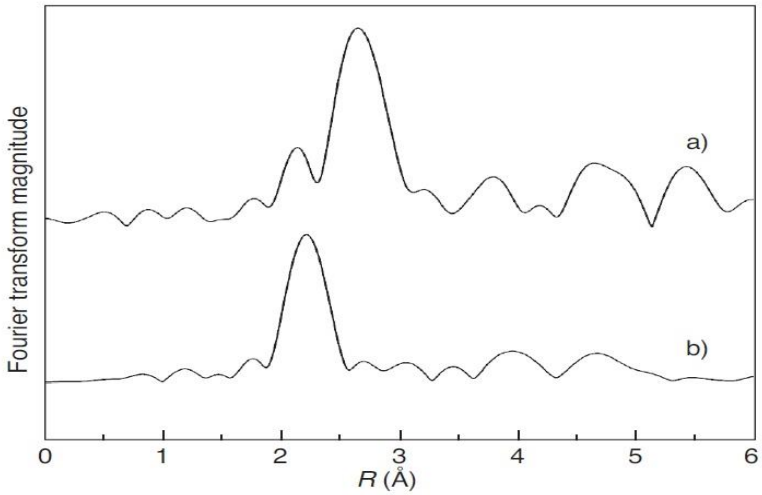

Figure 2.7: EXAFS analysis on (a) platinum foil and (b) 15%Co-1.0%Pt/Al_2O_3 after reduction at 673 [K] [29]

2.3.1.2 H_2 spillover

It is commonly established that one of the main advantages of noble metal promoter addition stands in the hydrogen spillover mechanism. If the activation of hydrogen on cobalt oxides is the slow step in the reduction processes, this mechanism facilitates the supply of dissociated (activated) hydrogen. Hydrogen spillover occurs from the promoter to the cobalt oxides and is defined as the chemisorption of hydrogen molecules on metal surfaces to form adsorbed hydrogen species, followed by their migration to another surface such as the support [1]. Dissociative adsorption of H_2 on the noble metal promoter is followed by the diffusion of atomic hydrogen along the support first, and then on to the reducible cobalt oxide. It has been observed that distances up to several millimeters can be covered. As pointed out by *Jacobs et al.* [30], the extent of reduction *versus* temperature trend strongly suggests a nucleation and growth mechanism for the reduction process. The reduction proceeds rapidly once cobalt metal nuclei are available for the dissociation of hydrogen (i.e. slow step).

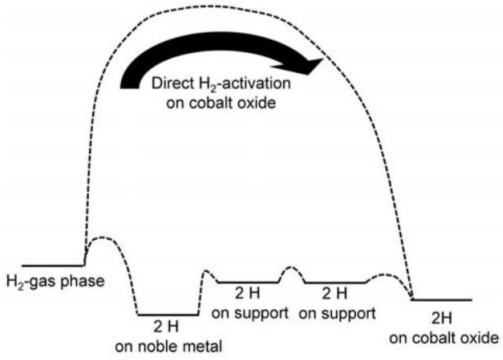

Figure 2.8: Energy levels required to facilitate the reduction of Co oxide due to the presence of a noble metal promoter [24]

According to *Nabaho et al.* [1], spillover mechanism may lead to different reduction paths of a metallic oxide in the presence of a noble metal promoter. Two main paths can be imagined, highlighted in Figure 2.9 with different colors. The first starts with dissociative adsorption of H_2 on the promoter surface (*1. Dissociative adsorption*) and is followed by the spillover step in which hydrogen atoms cross the promoter-oxide interface (*2. Spillover*). Reduction then occurs by reaction of the spillover hydrogen atoms with the oxygen of the metal oxide to form water (*3. Reduction*). Alternatively, spillover can occur from an isolated promoter crystallite leaned on the support (*II. Spillover*), followed by migration of hydrogen atoms via the surface hydroxyl groups (OH) of the oxidic support (*III. Surface migration*) and the final spillover from the support to the metal oxide (*IV Spillover*) that leads to reduction (*3. Reduction*). Reduction via H_2 spillover competes with the direct H_2 adsorption on the vacancies of the cobalt oxides (*A. Direct adsorption by oxide*).

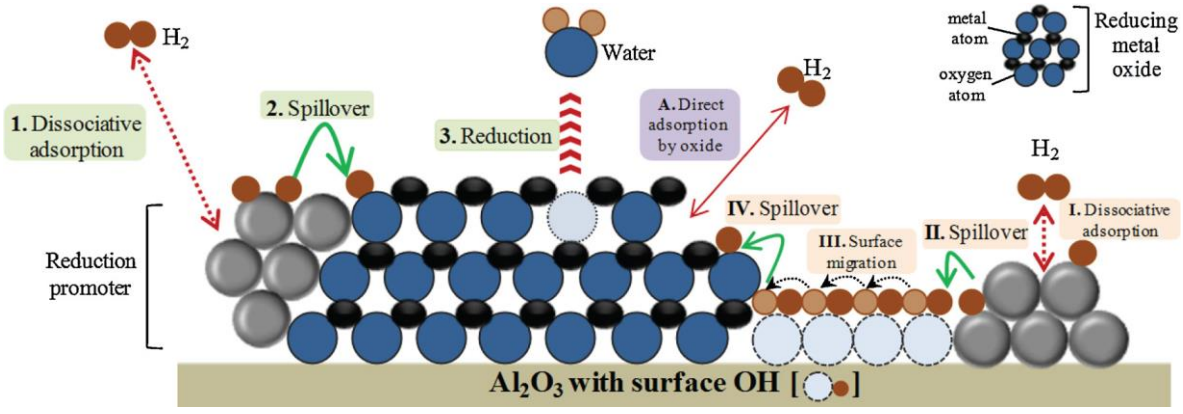

Figure 2.9: Proposed pathway of spillover hydrogen during promoter-aided reduction of a metal oxide [1]

It has been proposed [31], for the spillover mechanism via surface migration, that hydrogen migrates by continuously forming and breaking adjacent OH bonds. Although it seems the easiest explanation for the phenomenon, it is not likely to occur since the energy barrier for this process is quite high. An alternative explanation is the so-called 'bucket-brigade' model, in which surface OH groups do not migrate, but rather act as vehicles that pass along spillover hydrogen species. Spillover hydrogen is proposed to form with the support weak H-OH bonds, having lower energy barriers and thus faster rates of diffusion (Figure 2.10). When H_a crosses the metal-support interface to the closest surface OH group, H_O at the end of the chain is 'pushed' out of the network. Consequently, the spilt over H_a does not physically migrate but rather triggers a knock-on effect that results in a net displacement of hydrogen. The mobility in this manner is high because it is the charge of H_a being transferred, rather than its mass.

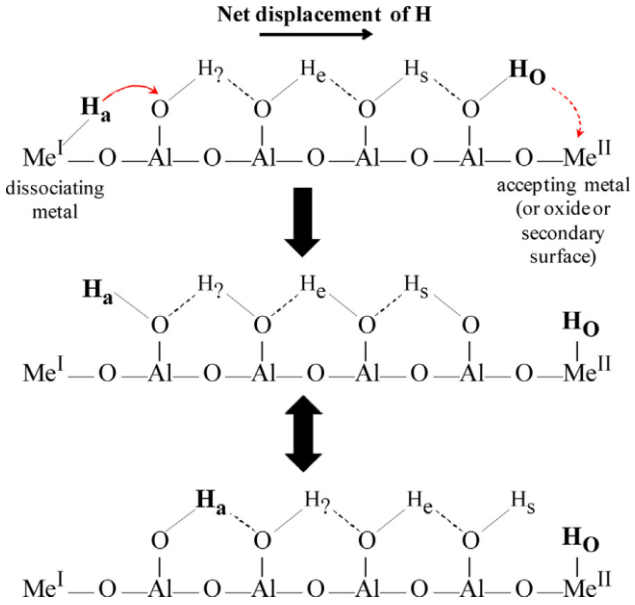

Figure 2.10: Surface migration of hydrogen according to the bucket-brigade model (–, covalent bonds and other interactions; ---, hydrogen bonds) [1]

Alternatively to the proposed bucket-brigade model, other pathways have been suggested to influence the spillover mechanism: transfer of only weakly chemisorbed hydrogen atoms [32], 'jumpover' of activated hydrogen atoms via the gas phase [33] and 'bridges' such as carbon and specific interfacial OH groups at the metal-support interface [34] are the main ones.

In the same work *Nabaho et al.* [1] tried to decouple the two possible effects ascribed to the promoter on Co-based catalysts: spillover and ligand/electronic effects. Unlike the first, the latter requires a physical contact between Pt and Co to occur. The role of Pt during reduction has been investigated using a model hybrid catalyst (mechanical mixture of Pt/Al_2O_3 + Co/Al_2O_3) prepared starting from γ-Al_2O_3 of 128 [μm], successively milled to 15 [μm]. Although the unmilled catalyst showed a very similar reduction behavior to that of the unpromoted catalyst, using milled γ-Al_2O_3 the reducibility of the hybrid catalyst increased: this indicates that, during reduction, no direct Pt-Co contact/coordination is needed to induce the promotion (Figure 2.11). It must be mentioned, however, that the same beneficial effect for the hybrid catalyst was not observed during FT reaction, probably due to the hindering effect of CO on the spillover mechanism, thus showing that a direct coordination between the two metals is still needed to increase the activity [1].

Nevertheless, milling of alumina apparently favored an intimate contact between the support particles, as the smaller particle size resulted in a higher contact area per unit mass; this enabled hydrogen to migrate over adjacent support particles, to ultimately reduce cobalt oxides at faster rates. These results can be ascribed to as evidence of hydrogen transportation via surface migration on the support, because the transfer via any other means cited above [32-34] would not have shown any dependence on the diameter of the support particles.

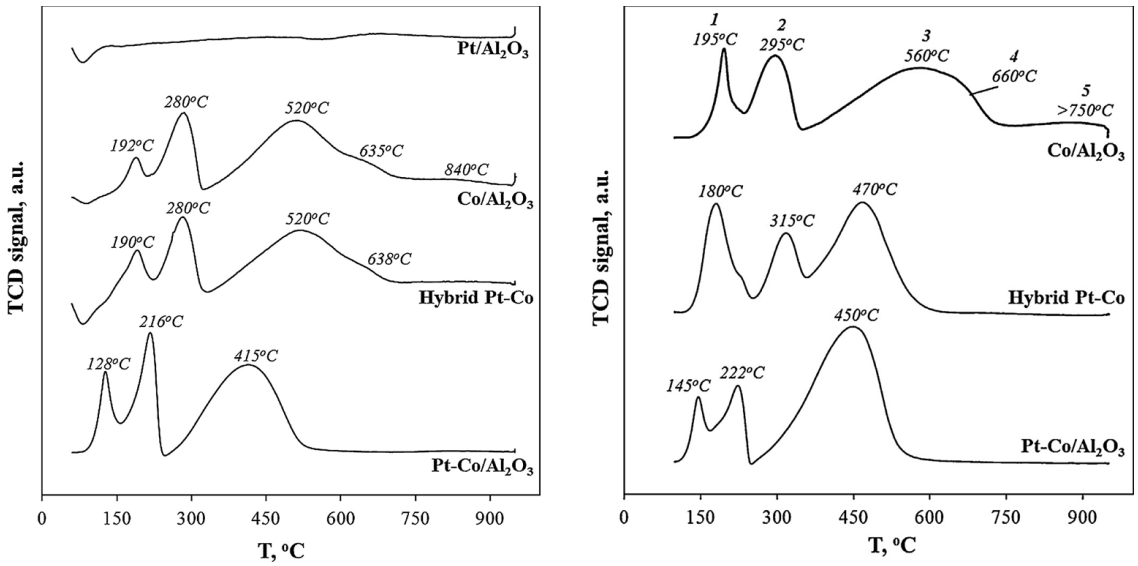

Figure 2.11: TPR profile of the catalyst samples prepared using: γ-Al_2O_3 128 [μm] and γ-Al_2O_3 15.5 [μm] [1]

Cobalt oxide reduction from Co_3O_4 to Co^0 is commonly thought to follow a path consisting of two reactions accounting, from a stoichiometric point of view, for 25% and 75% of the oxygen depletion respectively.

$$Co_3O_4 + H_2 \rightarrow 3CoO + H_2O \quad (2.3)$$

$$CoO + H_2 \rightarrow Co^0 + H_2O \quad (2.4)$$

Catalyst reducibility can be evaluated by characteristic temperatures of the two main TPR reduction steps. As it can be noticed from both Figure 2.11 and Figure 2.12, even a small addition of Pt shifts the reduction temperatures towards lower values.

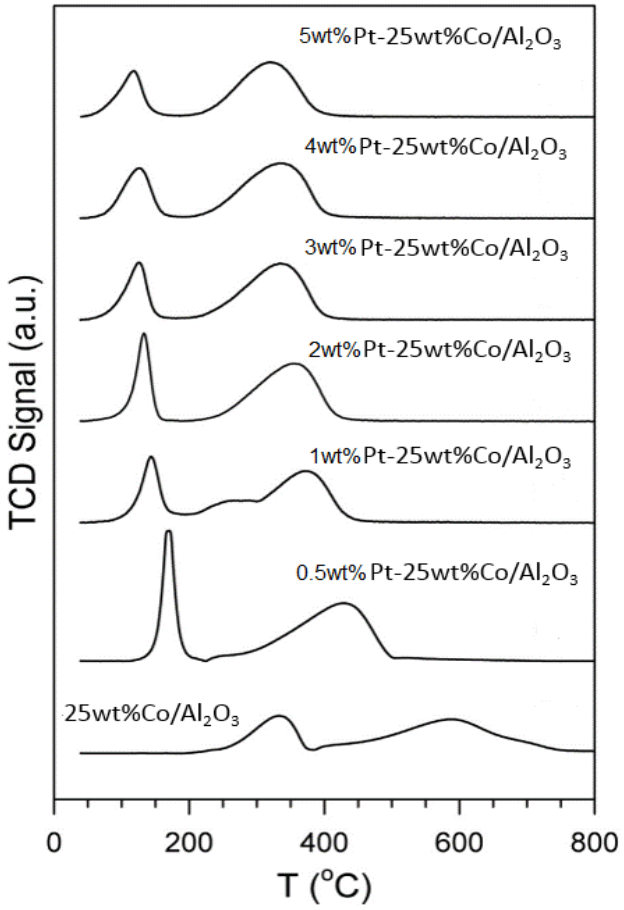

Figure 2.12: TPR profiles of unpromoted and Pt promoted 25%Co/Al2O3 catalysts [27]

Hence, platinum promotion leads to beneficial effects for both the reduction steps. However, as the transition $Co_3O_4 \rightarrow CoO$ occurs at low temperatures, usually lower than the typical catalyst activation temperatures (350 ÷ 400 [°C]), also unpromoted sample can easily get over this step. Thus, the major improvement with Pt promotion lays in the second step, i.e. the transition $CoO \rightarrow Co^0$, which is thought to be cluster-size dependent [29] and severely hindered by interaction with the alumina support [1]. The addition of Pt appears to decrease the energy barrier related to the second step, thus showing significantly lower reduction temperatures: this catalyzing effect was mainly attributed to H_2 dissociation and its subsequent spillover that occurs more readily on the noble metal surface than on the cobalt oxides surface.

2.3.1.3 Effect of Pt Promoter on activity, product selectivity and kinetic parameters

Ma, Jacobs et al. [35] studied the effect of Pt promotion on catalytic performances of a 15%Co/Al_2O_3 catalyst. The addition of 0.5% Pt improved the rate constant of CO hydrogenation by 140%: this is consistent with the fact that Pt significantly increases Co reduction and thus the number of active Co^0 sites; however, Pt did not alter *Co-site time yield* (CTY). In terms of selectivities, yields in light hydrocarbons (C_2 – C_4) and in heavier hydrocarbons increased and decreased, respectively: this behavior can be ascribed to the hydrogen dissociation on the noble metal and subsequent spillover onto the cobalt active site, which makes the system more hydrogenating. During FT reaction, a fraction of Pt may still be present on the catalyst surface and continue to facilitate dissociation of molecular H_2, continuously providing dissociated H to active Co^0 species and thus increasing the chain termination rate.

Bibliography Chapter 2

[1] D. Nabaho, J. W. Niemantsverdriet, M. Claeys, and E. Van Steen, "Hydrogen spillover in the Fischer-Tropsch synthesis: An analysis of platinum as a promoter for cobalt-alumina catalysts," *Catal. Today*, vol. 261, pp. 17–27, 2016.

[2] S. Vada, A. Hoff, E. ÅdnaneS, D. Schanke, and A. Holmen, "Fischer-Tropsch synthesis on supported cobalt catalysts promoted by platinum and rhenium," *Top. Catal.*, vol. 2, no. 1–4, pp. 155–162, 1995.

[3] G. Jacobs, T. K. Das, P. M. Patterson, J. Li, L. Sanchez, and B. H. Davis, "Fischer-Tropsch synthesis XAFS - XAFS studies of the effect of water on a Pt-promoted Co/Al2O3 catalyst," *Appl. Catal. A Gen.*, vol. 247, no. 2, pp. 335–343, 2003.

[4] F. Diehl and A. Y. Khodakov, "Promotion of Cobalt Fischer-Tropsch Catalysts with Noble Metals: a Review," *Oil Gas Sci. Technol. …*, vol. 64, no. 1, pp. 11–24, 2009.

[5] R. Reuel and C. H. Bartholomew, "Effects of Support and Dispersion on the CO Hydrogenation Activity / Selectivity Properties of Cobalt," *Journal of Catalysis*, vol. 85. pp. 78– 88, 1984.

[6] A. S. Lisitsyn, A. V. Golovin, V. L. Kuznetsov, and Y. I. Yermakov, "Properties of catalysts prepared by pyrolysis of Co2(CO)8 on silica containing surface Ti ions," *Journal of Catalysis*, vol. 95, no. 2. pp. 527–538, 1985.

[7] E. Iglesia, "Design, synthesis, and use of cobalt-based Fischer-Tropsch synthesis catalysts," *Appl. Catal. A Gen.*, vol. 161, pp. 59–78, 1997.

[8] B. G. Johnson, C. H. Bartholomew, and D. W. Goodman, "The Role of Surface Structure and Dispersion in CO Hydrogenation on Cobalt," *J. Catal.*, vol. 128, pp. 231–247, 1991.

[9] D. Schanke, a M. Hilmen, E. Bergene, K. Kinnari, E. Rytter, E. Adnanes, and A. Holmen, "Reoxidation and deactivation of supported cobalt Fischer-Tropsch catalysts," *Energy & Fuels*, vol. 10, no. 4, pp. 867–872, 1996.

[10] G. L. Bezemer, J. H. Bitter, H. P. C. E. Kuipers, H. Oosterbeek, J. E. Holewijn, X. Xu, F. Kapteijn, a J. Van Dillen, and K. P. De Jong, "Cobalt Particle Size Effects in the Fischer − Tropsch Reaction Studied with Carbon Nanofiber Supported Catalysts," *Am. Chem. Soc.*, vol. 128, no. 12, pp. 3956–3964, 2006.

[11] Ø. Borg, P. D. C. Dietzel, A. I. Spjelkavik, E. Z. Tveten, J. C. Walmsley, S. Diplas, S. Eri,

A. Holmen, and E. Rytter, “Fischer-Tropsch synthesis: Cobalt particle size and support effects on intrinsic activity and product distribution,” *J. Catal.*, vol. 259, no. 2, pp. 161–164, 2008.

[12] D. Tristantini, S. Lögdberg, B. Gevert, Ø. Borg, and A. Holmen, “The effect of synthesis gas composition on the Fischer-Tropsch synthesis over Co/γ-Al2O3 and Co-Re/γ-Al2O3 catalysts,” *Fuel Process. Technol.*, vol. 88, no. 7, pp. 643–649, 2007.

[13] J. P. den Breejen, J. R. A. Sietsma, H. Friedrich, J. H. Bitter, and K. P. de Jong, “Design of supported cobalt catalysts with maximum activity for the Fischer-Tropsch synthesis,” *J. Catal.*, vol. 270, no. 1, pp. 146–152, 2010.

[14] A. M. Saib, D. J. Moodley, I. M. Ciobîc, M. M. Hauman, B. H. Sigwebela, C. J. Weststrate, J. W. Niemantsverdriet, and J. Van De Loosdrecht, “Fundamental understanding of deactivation and regeneration of cobalt Fischer-Tropsch synthesis catalysts,” *Catal. Today*, vol. 154, no. 3–4, pp. 271–282, 2010.

[15] S. Sun, N. Tsubaki, and K. Fujimoto, “The reaction performances and characterization of Fischer–Tropsch synthesis Co/SiO2 catalysts prepared from mixed cobalt salts,” *Appl. Catal. A Gen.*, vol. 202, no. 1, pp. 121–131, 2000.

[16] J. S. Girardon, A. S. Lermontov, L. Gengembre, P. A. Chernavskii, A. Griboval-Constant, and A. Y. Khodakov, “Effect of cobalt precursor and pretreatment conditions on the structure and catalytic performance of cobalt silica-supported Fischer-Tropsch catalysts,” *J. Catal.*, vol. 230, no. 2, pp. 339–352, 2005.

[17] T. Cseri, S. Békássy, G. Kenessey, G. Liptay, and F. Figueras, “Characterization of metal nitrates and clay supported metal nitrates by thermal analysis,” *Thermochim. Acta*, vol. 288, no. 1–2, pp. 137–154, 1996.

[18] L. Poul, N. Jouini, and F. Fievet, “Layered hydroxide metal acetates (metal = zinc, cobalt, and nickel): Elaboration via hydrolysis in polyol medium and comparative study,” *Chem. Mater.*, vol. 12, no. 10, pp. 3123–3132, 2000.

[19] L. Shi, D. Li, B. Hou, Y. Wang, and Y. Sun, “The modification of SiO2 by various organic groups and its influence on the properties of cobalt-based catalysts for Fischer-Tropsch synthesis,” *Fuel Process. Technol.*, vol. 91, no. 4, pp. 394–398, 2010.

[20] N. Koizumi, Y. Hayasaka, Y. Ibi, S. Suzuki, T. Shindo, and M. Yamada, “Enhancing the fischer-tropsch synthesis activity of co-based catalysts by adding ZrO x to the SiO2 support and chelating ligands to the co-precursor,” *Catal. Letters*, vol. 141, no. 8, pp. 1207–1214,

2011.

[21] S. L. Gonzàlez-Cortés, T. C. Xiao, S. M. A. Rodulfo-Baechler, and M. L. H. Green, "Impact of the urea-matrix combustion method on the HDS performance of Ni-MoS2/??-Al2O3 catalysts," *J. Mol. Catal. A Chem.*, vol. 240, no. 1–2, pp. 214–225, 2005.

[22] B. Y. F. Morales and B. M. Weckhuysen, "Promotion Effects in Co-based Fischer – Tropsch Catalysis," *R. Soc. Chem.*, vol. 19, no. 1, pp. 1–40, 2006.

[23] Z. Zsoldos, T. Hoffer, and L. Guczi, "Structure and catalytic activity of alumina-supported platinum-cobalt bimetallic catalysts. 1. Characterization by x-ray photoelectron spectroscopy," *J. Phys. Chem.*, vol. 95, no. 2, pp. 798–801, 1991.

[24] M. De Beer, A. Kunene, D. Nabaho, M. Claeys, and E. Van Steen, "Technical and economic aspects of promotion of cobalt-based Fischer-Tropsch catalysts by noble metals – a review," vol. 114, no. October 2013, pp. 14–16, 2014.

[25] D. Schanke, S. Vada, E. A. Blekkan, A. M. Hilmen, A. Hoff, and A. Holmen, "Study of Pt-promoted cobalt CO hydrogenation catalysts," *Journal of Catalysis*, vol. 156. pp. 85–95, 1995.

[26] A. Y. Khodakov, R. Bechara, and A. Griboval-Constant, "Fischer-Tropsch synthesis over silica supported cobalt catalysts: Mesoporous structure versus cobalt surface density," *Appl. Catal. A Gen.*, vol. 254, no. 2, pp. 273–288, 2003.

[27] T. Jermwongratanachai, G. Jacobs, W. Ma, W. D. Shafer, M. K. Gnanamani, P. Gao, B. Kitiyanan, B. H. Davis, J. L. S. Klettlinger, C. H. Yen, D. C. Cronauer, A. J. Kropf, and C. L. Marshall, "Fischer-Tropsch synthesis: Comparisons between Pt and Ag promoted Co/Al2O3 catalysts for reducibility, local atomic structure, catalytic activity, and oxidation-reduction (OR) cycles," *Appl. Catal. A Gen.*, vol. 464–465, pp. 165–180, 2013.

[28] A. Y. Khodakov, "Enhancing cobalt dispersion in supported Fischer-Tropsch catalysts via controlled decomposition of cobalt precursors," *Brazilian J. Phys.*, vol. 39, no. 1, pp. 171–175, 2009.

[29] G. Jacobs, J. a. Chaney, P. M. Patterson, T. K. Das, J. C. Maillot, and B. H. Davis, "Fischer-Tropsch synthesis: study of the promotion of Pt on the reduction property of Co/Al2O3 catalysts by in situ EXAFS of Co K and Pt L3 in situ edges and XPS," *J. Synchrotron Radiat.*, vol. 11, no. 5, pp. 414–422, 2004.

[30] G. Jacobs, T. K. Das, Y. Zhang, J. Li, G. Racoillet, and B. H. Davis, "Fischer-Tropsch synthesis: Support, loading, and promoter effects on the reducibility of cobalt catalysts,"

Appl. Catal. A Gen., vol. 233, no. 1–2, pp. 263–281, 2002.

[31] J. Y. Luo and W. S. Epling, "New insights into the promoting effect of H2O on a model Pt/Ba/Al2O3 NSR catalyst," *Appl. Catal. B Environ.*, vol. 97, no. 1–2, pp. 236–247, 2010.

[32] K. Gadgil and R. D. Gonzalez, "The adsorption of hydrogen atoms on support oxides active in promoting hydrogen atom spillover," *Journal of Catalysis*, vol. 40, no. 2. pp. 190–196, 1975.

[33] G. A. Badun, B. F. G. Johnson, and N. E. Shchepina, "Long distance hydrogen spillover found by a radioactive assay for the Ru5Pt/MCM-41 catalytic system," *Mendeleev Commun.*, vol. 19, no. 4, pp. 235–236, 2009.

[34] W. . Neikam and M. . Vannice, "Hydrogen spillover in the Pt black_Ce-Y zeolite_perylene system," *J. Catal.*, vol. 27, no. 2, pp. 207–214, 1972.

[35] W. Ma, G. Jacobs, R. Keogh, C. H. Yen, J. L. S. Klettlinger, and B. H. Davis, "Fischer-Tropsch synthesis: Effect of Pt promoter on activity, selectivities to hydrocarbons and oxygenates, and kinetic parameters over 15%Co/Al2O3," *ACS Symp. Ser.*, vol. 1084, pp. 127–153, 2011.

Chapter 3 – Lab-Scale Rig and Experimental Procedures

3.1 Fixed bed lab-scale rig

The reducibility studies and catalytic testing of state of the art Fischer-Tropsch catalysts have been performed in the LCCP (*Laboratory of Catalysis and Catalytic Processes*) laboratories on a rig operating at ambient pressure, shown in Figure 3.1.

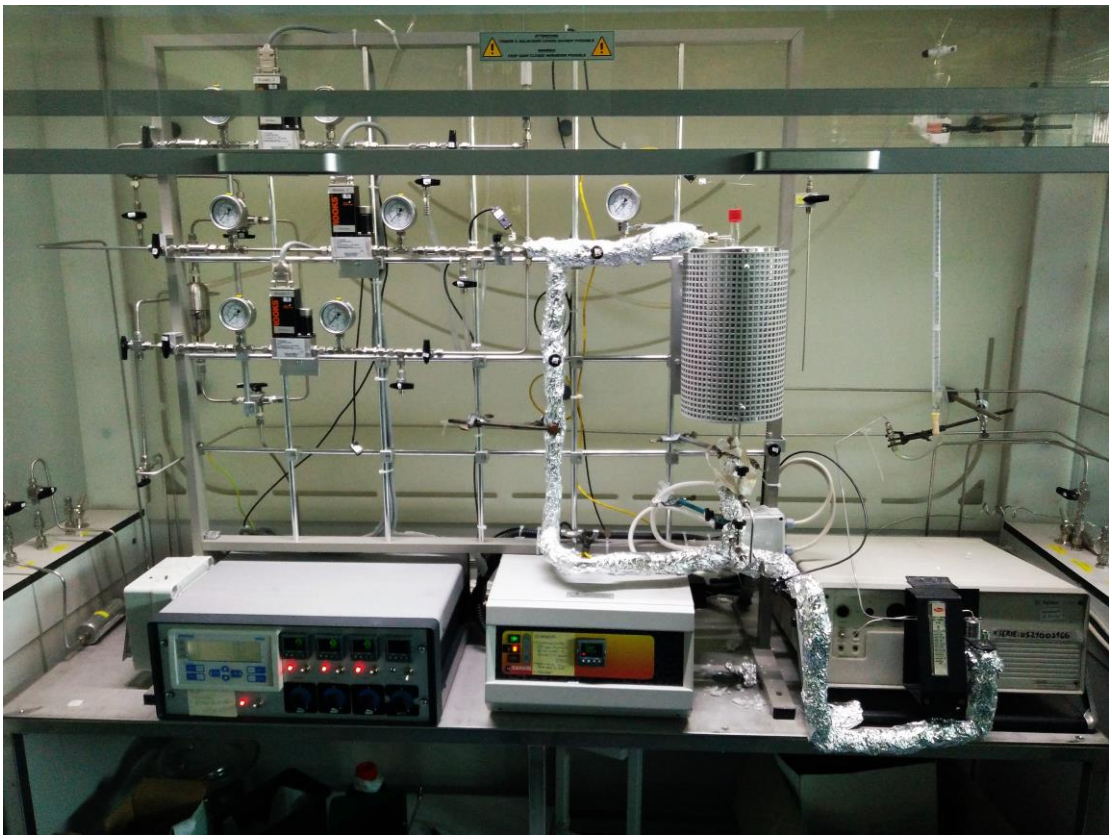

Figure 3.1: Lab scale experimental rig

It consists essentially of three main zones:

1. *Feed zone*
2. *Reaction zone*
3. *Product analysis zone*

As in Figure 3.1, some sections that need to be kept at high temperature are winded with heating tapes, which are in turn insulated with glass wool and a layer of aluminium sheet. The temperature of the line is monitored by two J-type thermocouples: their measures are sent to the control unit which regulates the thermal power emitted by the electrical resistance.
Except the high temperature section, which is made up of 1/16 [in] diameter tubes, the employed piping consists of 1/8 [in] diameter tubes, made of *INOX ASME 316 SEAMLESS* steel.

3.1.1 Feed zone

The feed zone is the part of the rig related to purification, regulation and distribution of the inlet gases.
The rig is connected to five gas lines, although only three of them can be used contemporarily. In particular, the upper one in Figure 3.1, named *IDR2* line, conveys the reactants; depending on the type of experiment carried out, different gas mixtures can flow in this line. They can be either syngas, during catalytic testing, a mixture of hydrogen and argon during reducibility analyses or a mixture of light hydrocarbons and CO_2 during calibration of the gas detector.
The line in the middle, named *H2* line, conveys pure molecular hydrogen and is operated during catalyst activation.
The lower line is connected to three gas ducts by means of two three-way valves in series: the gas mixtures which can be fed are either pure nitrogen (*Mix AC2* line), which is the inert during catalytic testing, pure helium (*He* line), used as a purge gas during cleaning operations, or a mixture of oxygen and helium, flowed when passivating the catalyst.
It is noteworthy to observe in Figure 3.1 the great similarities among the three lines. Each one is characterized by a sequence of four elements: an on/off valve to intercept the gas, a Bourdon tube pressure gauge ($P_{full\text{-}scale}$= 6 [barg]) and a mass flow controller followed by another Bourdon tube pressure gauge (Figure 3.2). Downstream of each line the gas can either be vented or

sent to the connecting joint of the three lines, where the reaction zone begins. While N_2 can be vented in the atmosphere (see Figure 3.2), the other gases are vented through the fume hood.

Figure 3.2: Flow control equipment (*Mix AC2* line)

An additional safety valve is connected to the joint so as to vent the gas in case of sudden overpressures in the rig.

Between the cylinders and the facility two pressure reduction valves are installed in order to keep the pressure at proper values for an accurate operation of the flow controllers.

Purification of the inlet gases

As frequently the presence of impurities within a gas cylinder is not negligible, each gas duct is equipped with a purification system before the inlet of the three lines described above. Feeding impurities to the reaction zone may affect the experiments both in qualitative (e.g. catalyst deactivation) and quantitative terms (e.g. incorrect inlet composition); it is therefore mandatory to feed gases as pure as possible in order to have appropriate reliability and reproducibility of the experimental data. In particular, the syngas feed must be free from CO_2 traces and iron-carbonyl compounds: to pursuit this requirement a so-called "iron-carbonyl trap" is installed (Figure 3.3).

Figure 3.3: Iron-carbonyl trap

This trap, made of steel (*INOX AISI 304*), is filled up with alkaline alumina pellets and connected at both ends with the *IDR2* line by means of threads. The alkaline alumina is prepared by impregnating γ-Al_2O_3 spheres (*Sasol*, d_{pellet} = 600 [μm]) with 12 wt.% potassium, using potassium carbonate (*Sigma Aldrich*, purity ≥ 99.0%) as a precursor. The impregnated spheres are then calcined in air at 500 [°C] (dT/dt = 1 [°C/min]).

The efficiency of the trap is periodically monitored by analysing the composition of the syngas feed. A by-pass line parallel to the trap is installed: can be useful when feeding harmful compounds to the trap such as light hydrocarbons, especially methane. Both the lines carrying N_2 and He are equipped with a so-called *oxyclear* unit which removes O_2 traces, residual from the air separation, from the gas streams. O_2 is very harmful during experiment as it tends to oxidize the catalyst, thus deactivating it.

Flow control of the inlet gases

The flow control in the facility is performed by three mass flow controllers (*BROOKS® Smart II Mass Flow model 5850S*). *IDR2* and *H2* line controllers can regulate a flow rate up to 100 [ml/min] whereas the controller's maximum flow rate for *Mix AC2* line is 200 [ml/min].

Each controller needs to undergo calibration before performing the experiments. The calibration is carried out by measuring the flow rates corresponding to different degrees of opening of the controller. During calibration, the glass flowmeter shown on the right hand side of Figure 3.1, has always been connected to the vent valve right after the corresponding flow controller, in order to avoid inaccuracy related to pressure drops along the line. Performing a linear regression of the measured data, a characteristic line is obtained:

$$Flow\ rate = m \cdot (degree\ of\ opening) + q \tag{3.1}$$

An example of calibration line obtained is reported in Figure 3.4:

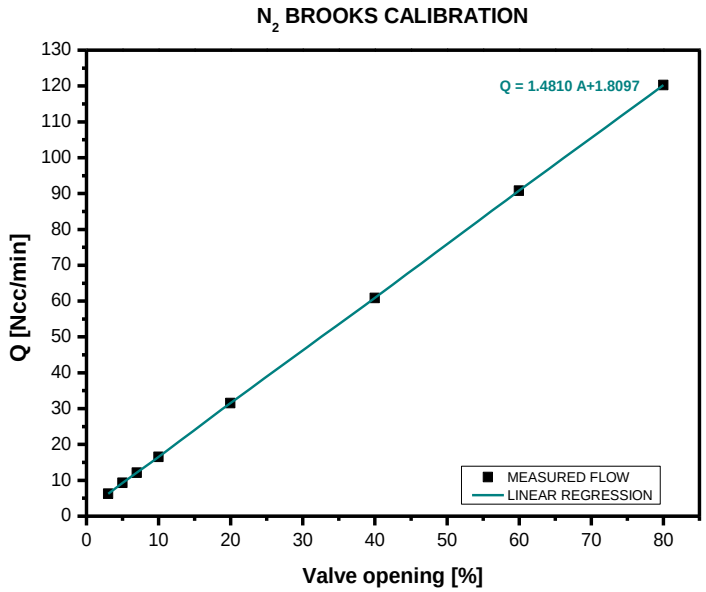

Figure 3.4: Calibration line for the mass flow controller of *MIX AC2* line

Albeit the calibration lines should cross the origin, the q values are in reality slightly different from zero, due to the closing dynamics of the valve whose behaviour is not precisely linear. Nevertheless, the typical work range of the controllers is entirely investigated during calibration. The latter is carried out periodically to guarantee correct flow rates throughout the experiments.

3.1.2 Reaction zone

The reaction zone starts from the connecting joint of the three lines, which is a four-way valve. From the latter follows a pipe that branches into two lines of 1/16 [in] diameter: one is connected to the reactor, the other is the by-pass line (insulated lines in Figure 3.1). In both of them, the flow is controlled by means of a needle valve. Downstream of the reactor, the gas can either flow directly into the by-pass line, which leads to the gas detector, or through a trap for condensable products, before reconnecting to the by-pass line. This two-way flow is handled via three additional needle valves installed downstream of the reactor.

3.1.2.1 Reactor

The fixed bed reactor employed in the experiments is a quartz tube of 12 [mm] diameter and 230 [mm] length. At its bottom, the solid flow is restrained by means of a porous separator which only allows the gas flow through it.

The loading of the reactor strongly depends on the axial temperature profile of the electrical oven in which the reactor is accommodated.

Thermal profile of the reactor

In order to ensure validity of the experimental data, the catalyst bed must lie in the isothermal section of the oven: it is therefore necessary to determine the temperature profile of the reactor before performing experiments. The thermal profile of the reactor is obtained using two J-type thermocouples: one is fixed on the porous separator at the bottom of the reactor and connected to the oven, so as to maintain constant heat flux, the other is mobile along the reactor and generates the thermal profile.

The first rough measures are obtained loading the entire reactor volume with a solid inert (quartz grains). Once the isothermal zone is identified, the same measure is carried out by filling the isothermal zone with α-Al_2O_3, so as to get closer to the thermal conductivity of the real catalyst bed. Two profiles have been obtained, by imposing as set point temperatures the catalyst activation temperature (400 [°C]) and the reaction temperature (240 [°C]).

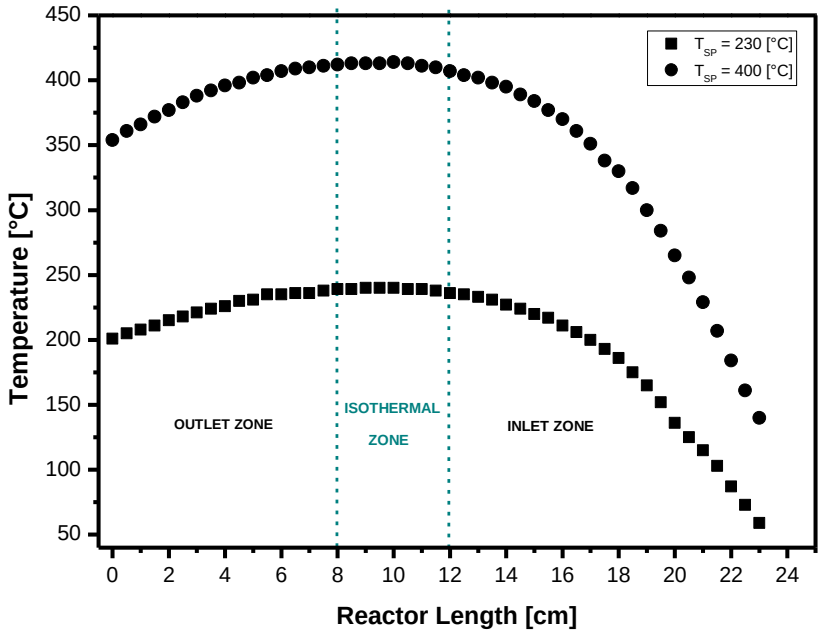

Figure 3.5: Thermal profile of the reactor

As the results show (Figure 3.5), the isothermal zone lays between 8 ÷ 12 [cm] from the porous separator. Being the catalyst bed 2.5 [cm] long, the length of the isothermal zone allows operations in reasonably isothermal conditions.

The final check is to verify the results obtained by measuring the temperature with a J-type thermocouple placed in the centre of the catalyst bed.

3.1.2.2 Condensable gas trap

Aim of this unit is to prevent that condensable species may reach the gas detector logging its absorption columns. Depending on the experiments carried out, different traps are employed.

Figure 3.6: Glass condenser

Figure 3.7: Soda-lime water trap

During catalytic testing, a simple glass condenser kept in cooling bath is used (Figure 3.6), while during TPR analyses the glass condenser is substituted with a U-shaped steel pipe (1/8 [in] diameter) filled with soda-lime powder (Figure 3.7).

3.1.2.3 Product analysis zone

Downstream of the reactor, the gas merges into the by-pass line and flows towards the gas detector. Since the gas stream flowing through the gas detector must be at high temperature, the line connecting the bottom of the reactor to the gas detector is heated up and insulated. The instrument installed in the rig is a gas chromatograph (*Agilent 3000 Micro Gas Chromatograph*): it consists of four columns, operating at different temperatures and pressures, downstream of which four TCD (*Thermal Conductivity Detectors*) are present. The TCD senses changes in the thermal conductivity of the column effluent by means of a filament immersed into the carrier gas: when the gas sample enters the columns, the composition changes and so does the thermal conductivity, causing a variation of the filament temperature. As a result, the electrical conductivity is altered, triggering a change of the potential difference across the filament for the entire contact time between the gas sample and the filament. The TCD allows detection of compounds which have a considerable thermal conductivity difference from the carrier gas; helium is often employed as a carrier gas, mainly because it is inert and it has a thermal conductivity about seven times higher than that of common organic gases.

Column A

The first column is 4 [m] long and filled with molecular sieves. It is operated at 80 [°C] and 24.5 [psi]. By means of this column H_2, N_2, CH_4, CO respectively can be separated and observed (Figure 3.8). Being the H_2 thermal conductivity close to that of He, Ar is preferred as a carrier gas so that H_2 can be better detected.

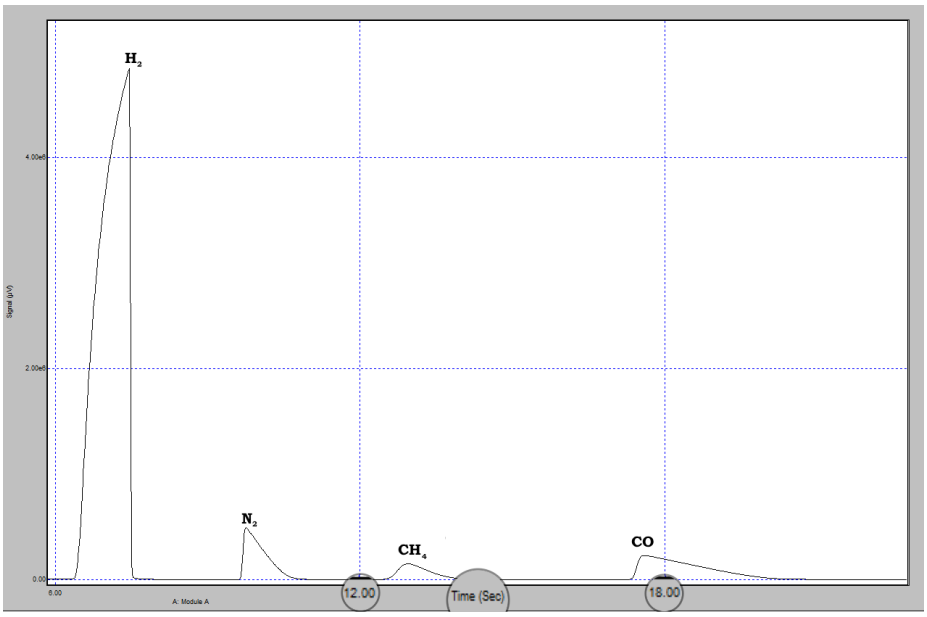

Figure 3.8: Typical chromatogram for column A (H_2, N_2, CH_4, CO)

Column B

The second column is filled with molecular sieves with backflush. It is operated at 100 [°C] and 28.7 [psi] with He as a carrier gas. Ar, N_2, CH_4 and CO respectively are separated in this column (Figure 3.9).

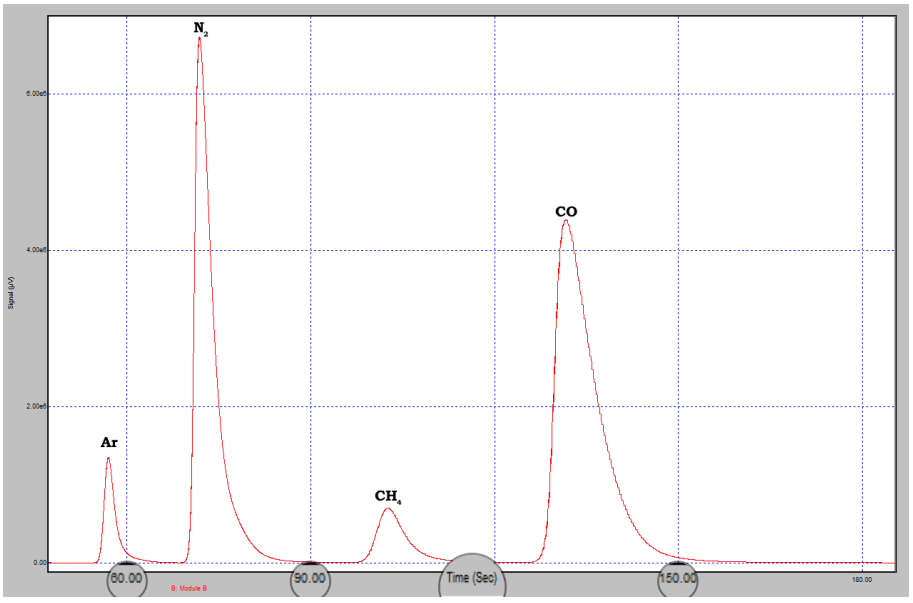

Figure 3.9: Typical chromatogram for column B (Ar, N_2, CH_4, CO)

Column C

The third column is significantly different from the first two: it is a *PLOT-Q* type column, operating at 55 [°C] and 22.3 [psi]. CH_4, CO_2, C_2H_4, C_2H_6, C_3H_6, C_3H_8 respectively are detected.

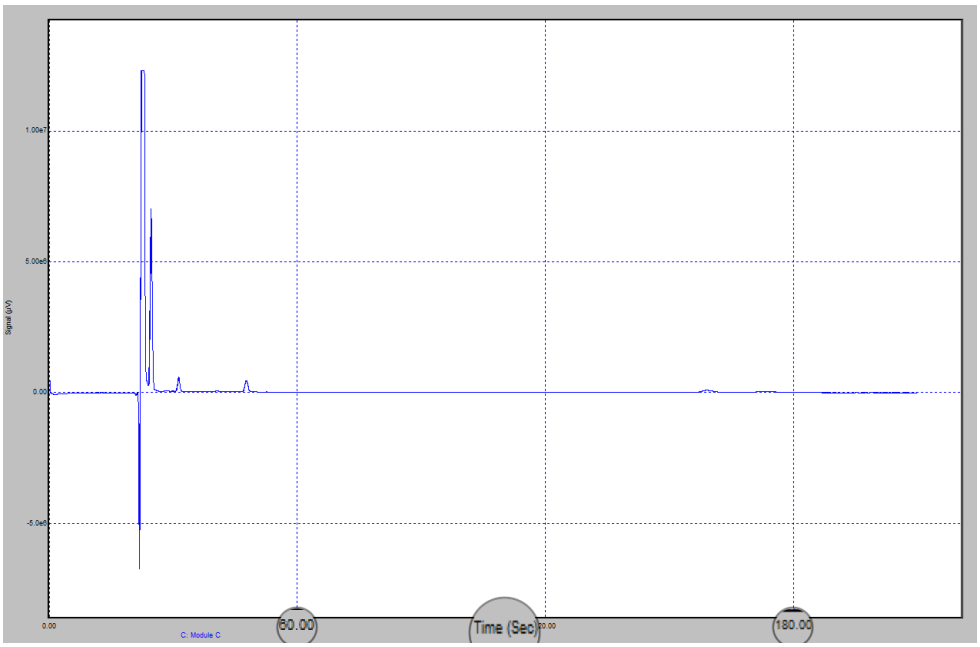

Figure 3.10: Typical chromatogram for column C

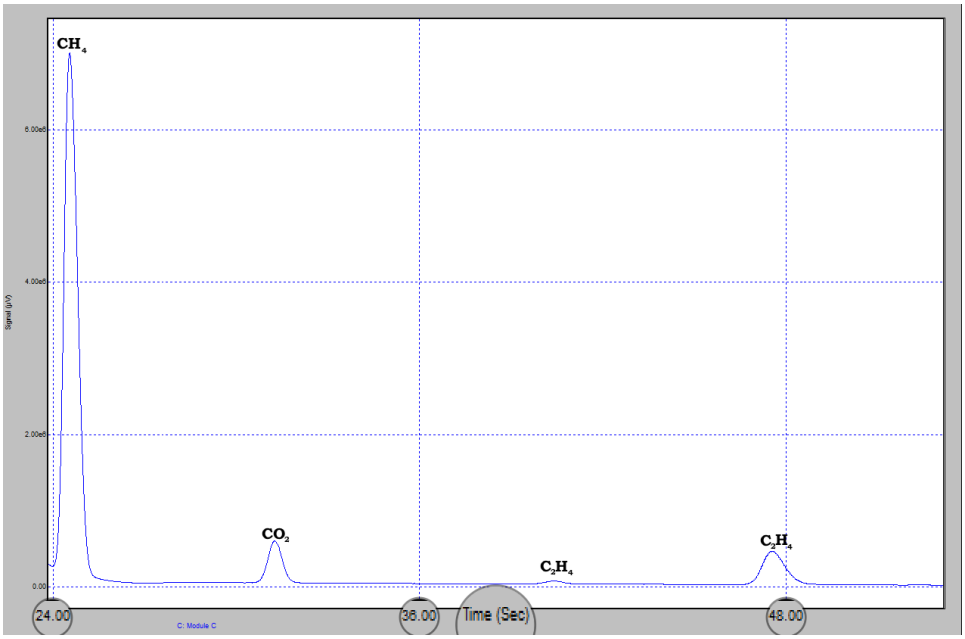

Figure 3.11: Zoom of the initial part of column C chromatogram (CH_4, CO_2, C_2H_4, C_2H_6)

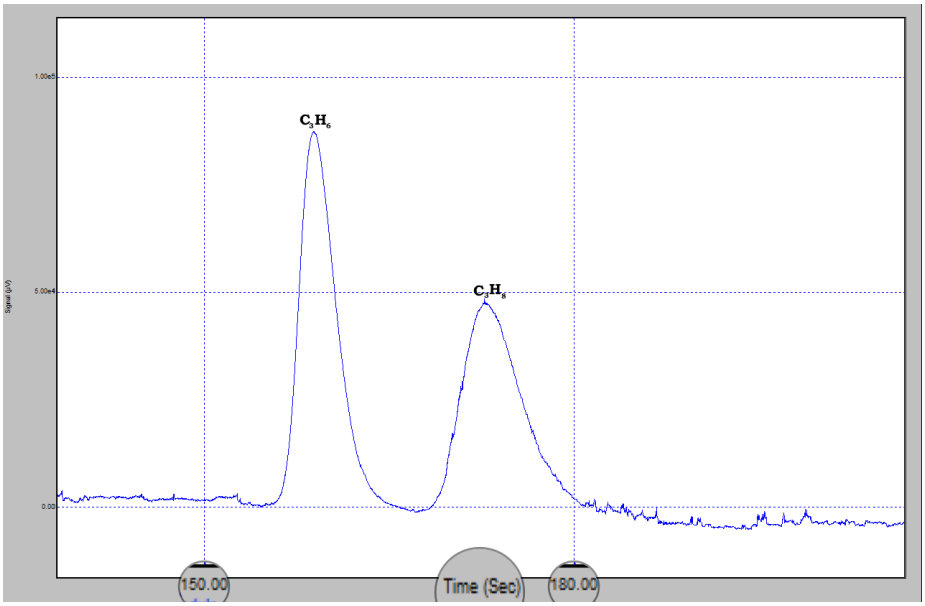

Figure 3.12: Zoom of the final part of column C chromatogram (C_3H_6, C_3H_8)

Column D

The fourth and last column is a *OV-1* type column, operating at 55 [°C] and 27.2 [psi]. The hydrocarbon fractions C_4, C_5, C_6 can be detected.

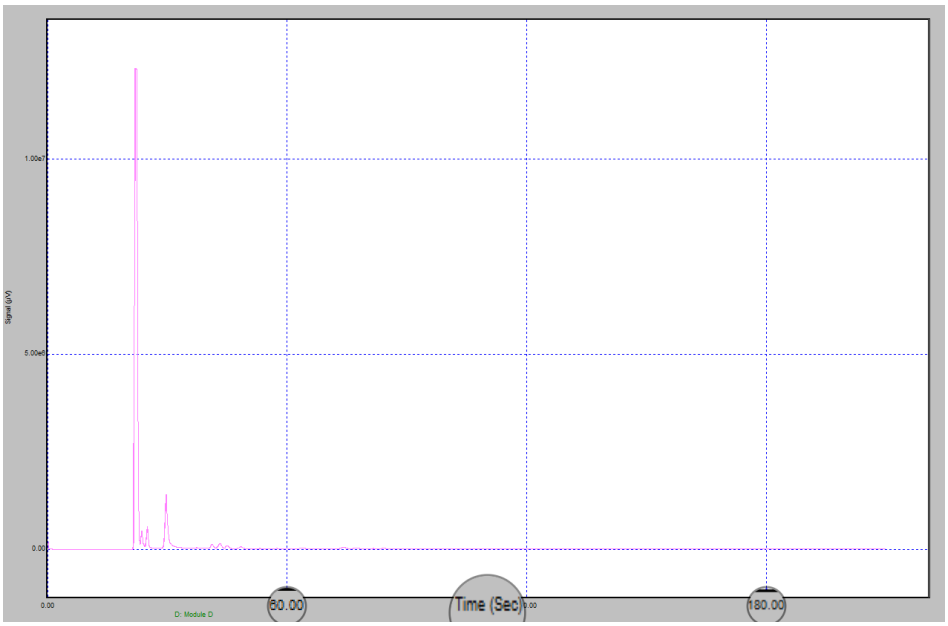

Figure 3.13: Typical chromatogram for column D

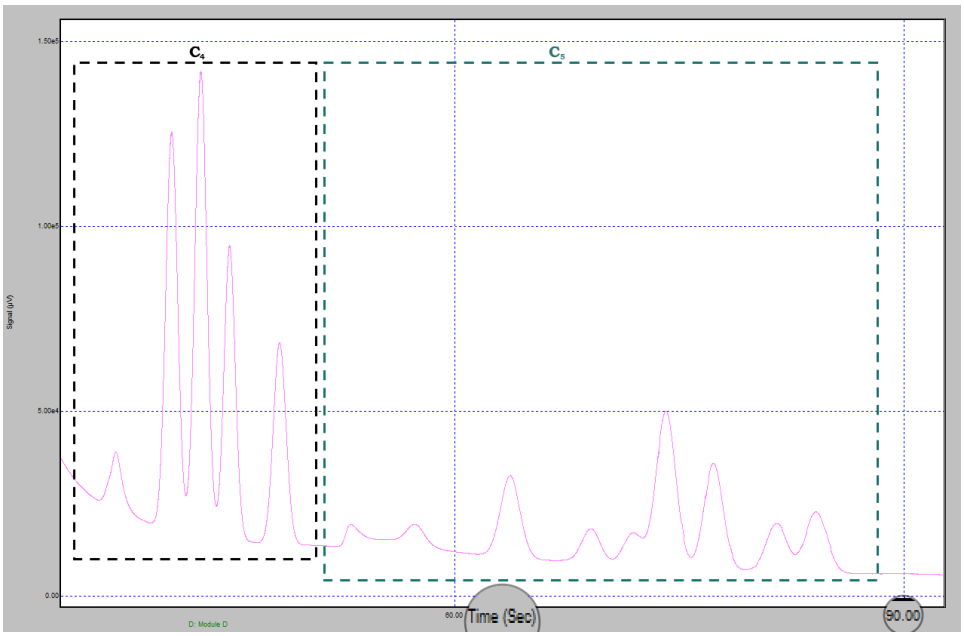

Figure 3.14: Zoom of the initial part of column D chromatogram (C_4, C_5)

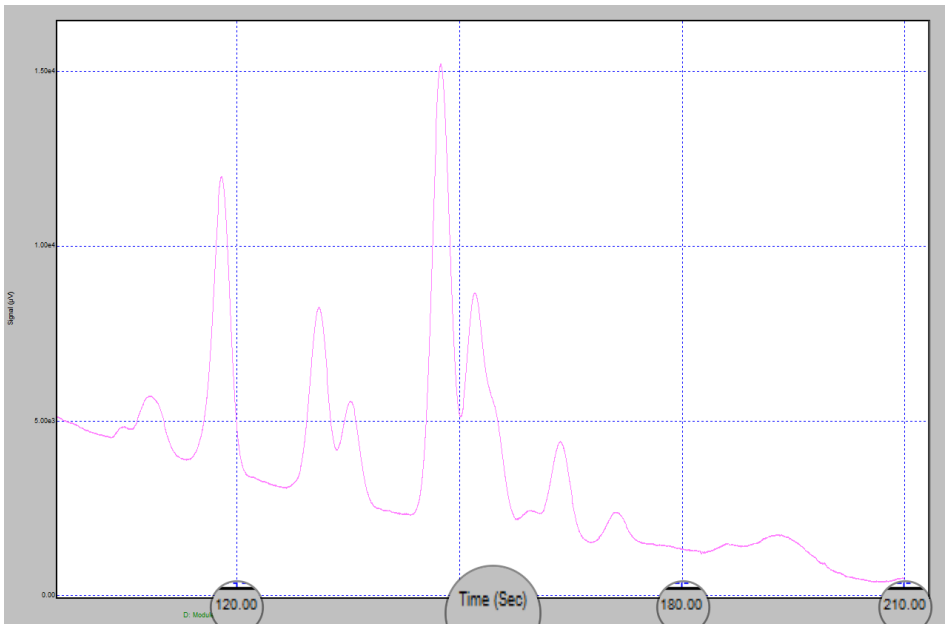

Figure 3.15: Zoom of the final part of column D chromatogram (C_6)

Gas chromatograph calibration

The output of the GC (*Gas Chromatograph*) is a variable potential signal which is sent to the CPU (*Central Processing Unit*), where it is processed and transformed into the so-called chromatogram: the latter consists of a profile with a number of peaks corresponding to different compounds which are present in the gas sample. The proportionality of the peak's area to the corresponding species concentration is governed by the following equation:

$$\frac{A_i}{C_i} \cdot f_i = \frac{A_{ref}}{C_{ref}} \tag{3.2}$$

Where: A_{ref} = area of the reference compound

C_{ref} = concentration of the reference compound

A_i = area of the i compound

C_i = concentration of i compound

Hence, in order to determine the concentration of the *i* species, it is necessary a reference compound whose concentration is constant and known throughout the experiments. The term f_i is the so-called *response factor*: it is the end point of the calibration process as it enables to relate the *i* species concentration (unknown) to the reference concentration (known).

The calibration is carried out by analysing samples of a product mixture, at known concentration, sent to the chromatograph from the *IDR2* line. The adopted reference species must be consistent both during calibration and during experiments and has to be inert during the reaction. The product mixture of known concentration contains N_2 and Ar: the latter is chosen as reference species because it is also present in the reacting syngas mixture. However, as argon is detected only in column B, it is necessary to find a common species which can be detected by all the columns: apart from column D, columns A, B and C can detect methane. Once methane concentration is acquired from column B, where Ar is the reference, methane becomes the new reference for the remaining columns A and C. This procedure is named *internal standard method*. Unfortunately, as column D does not share any of its compounds with the other columns, it becomes necessary to follow a different path in determining its species compositions. The so-called *external standard method*, used for column D, can be extended as side-check also to the other columns because it does not

depend on any reference compound. It defines a linear relationship between peak area and composition:

$$A_i = m_i \cdot x_i + q_i \qquad (3.3)$$

By collecting experimental data at different inlet gas compositions, it is possible to perform a linear regression obtaining the m_i and q_i values needed for the instrument calibration, without any dependence on reference species. Experimentally, the gas mixture of known composition if progressively diluted by co-feeding nitrogen: the gas analyses at different compositions should lie on a straight line crossing the origin (Figure 3.16).

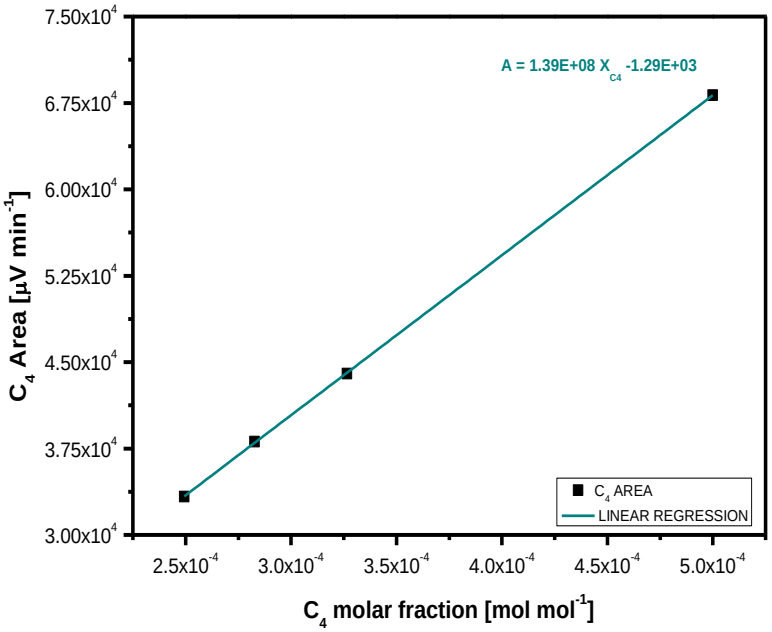

Figure 3.16: Calibration line for C4 species of column D (*external standard method*)

When available, the *internal standard method* is preferred: the other is highly sensible to alterations in flow rate and volume of the gas sample injected into the GC.

3.2 Catalyst testing

Aim of this phase of the experiments is to evaluate the performances at ambient pressure of the FT catalysts. In order to ensure accuracy and reproducibility, some standard procedures have been established, concerning the following phases of the catalytic testing:

1. Reactor preparation
2. In situ catalyst activation
3. Start up and reaction

3.2.1 Reactor preparation

The catalyst bed has to be placed into the reactor's isothermal section, which starts 8 [cm] above the porous separator and is about 4 [cm] long. The catalyst bed is made of a mechanical mixture of pure catalyst (m_{cat} = 2 [g]) diluted into α-Al_2O_3, 1:4 catalyst-alumina ratio. The α-Al_2O_3 powder is employed as a thermal diluent so as to ensure a uniform temperature distribution in the catalyst bed and avoid potential hot spots. Also, from the chemical point of view this allotropic form of alumina has low porosity and thus appropriate inertness in the reaction.

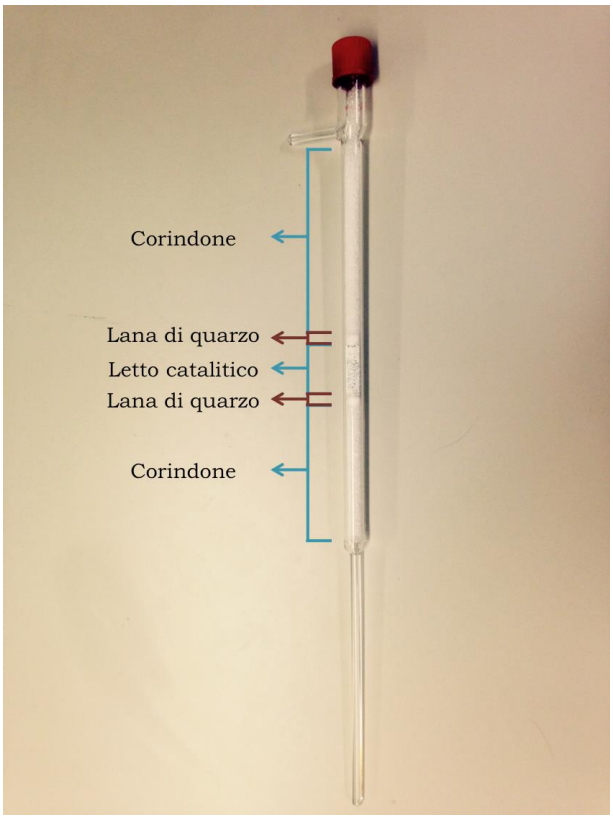

Figure 3.17: Reactor loading (TEMPORARY)

As shown in Figure 3.17, the catalyst bed is packed into two different layers on both sides: from the bottom, the reactor is loaded with 8 [cm] of corundum, a solid inert, and 0.5 [cm] of quartz wool to block the catalyst bed in the isothermal section and prevent its mixing with the corundum: the same applies above the bed in reversed order. The main role of the corundum is to create a uniform flux towards the catalyst bed, avoiding local composition gradients.

3.2.2 Catalyst activation

Once the reactor is loaded, a J-type thermocouple is placed in the centre of the catalyst bed and the reactor is closed with a plastic cork: it is then placed inside the oven and connected to the gas line. A leak test is carried out afterwards by closing the needle valve downstream of the reactor and feeding nitrogen until the pressure gauge upstream measures about 0.5-0.8 [barg]: the needle valve before the reactor is then closed, while the bypass line is opened and nitrogen flows through it. The system is kept under these conditions for 45 [min]: if the measured pressure does not change, the

leak test is considered as passed. Subsequently, a measure of the flow rate at the glass flowmeter provides an additional check for the presence of leakages. Subsequently, the connecting joints of the reactor with the gas line are insulated by glass wool and a layer of aluminum sheet: it is essential in this operation to fill the crawlspaces between the reactor and the oven walls, so as to prevent heat losses.

Now the system is ready for the in-situ reduction: the feed is switched from N_2 (*Mix AC2* line) to pure H_2 (*H2* line) at 50 [Ncc/min] and the GC analyses are run to check the purity of the feed. Once the chromatogram shows a flat profile apart from the H_2 peak, the oven is set for a 2 [°C/min] temperature ramp from 25 [°C] to 400 [°C]: the final temperature is maintained for 13.5 [h]. During catalyst activation, the two-step reduction mechanism of Co_3O_4 species occurs, yielding metallic cobalt (Co^0), which is the active phase during Fischer-Tropsch synthesis. The reactor is then cooled down to 180 [°C] (10 [°C/min]).

3.2.3 Start up and reaction

The activation step is followed by an intermediate phase whose purpose is to approach reaction conditions as smoothly as possible, because sudden changes in the operating conditions may damage the catalyst. At 180 [°C] the Fischer-Tropsch kinetics are still very slow, thus the H_2 feed can be switched to syngas (H_2/CO = 1, Q_{syn} = 42.54 [Ncc/min]) mixed with nitrogen in a high amount (Q_{N2} = 50 [Ncc/min]): this very diluted stream is almost inert at such low temperatures. The system is then brought to the reaction temperature of 240 [°C] following a temperature ramp of 1 [°C/min]; subsequently, nitrogen flow rate is slowly reduced (-1.5 [Ncc/min/min]) to the final value of 7.46 [Ncc/min]. The final fraction of inert gases in the reacting mixture, including both nitrogen and argon (2% of the syngas feed), is around 16 vol%. Figure 3.18 shows how reactor temperature and feed concentration change during start up and reaction.

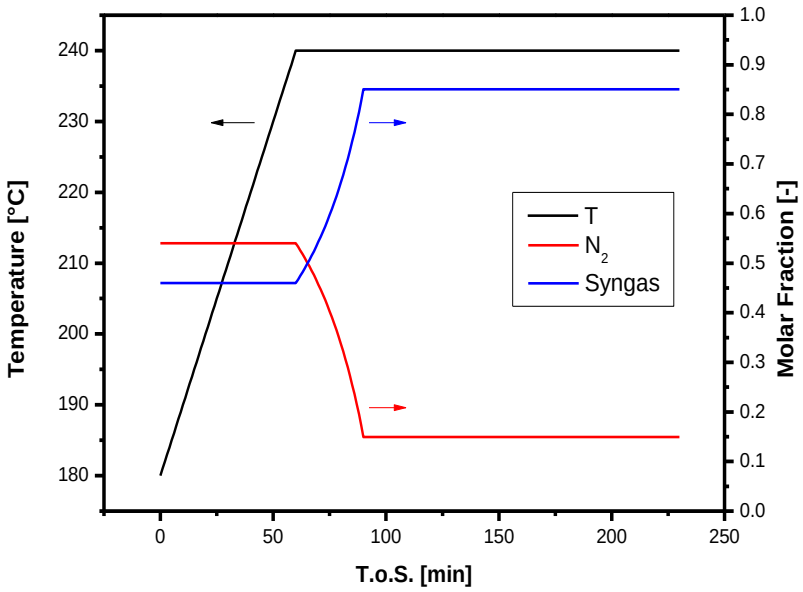

Figure 3.18: Temperature and molar fraction profiles during start up and reaction

3.3 Catalyst characterization

3.3.1 ICP-MS

The ICP-MS (*Inductively Coupled Plasma-Mass Spectrometry*) is an analytic tool capable of identifying the percent elemental composition of a sample. The analyses on this instrument have been performed, so as to verify that the actual amounts of active phase and promoter on the catalysts were the ones expected during preparation. Experimentally, the sample is dissolved into concentrated nitric acid or, when noble metals are present, concentrated hydrochloric acid; if the dissolution is not complete some phosphoric acid is added. Subsequently, the sample is introduced in a microwave oven (*Multiwave 3000, Anton-Paar*) which operates at 240 [°C] and 60 [atm]: the solution is then cooled down and nebulized so that a quadrupole achieves the separation, based on the mass/charge ratio. Finally, a detector downstream measures the concentration of the elements.

3.3.2 BET-BJH

The BET analysis – in honour of the scientists *Brunauer, Emmet and Teller* – coupled with the BJH – *Barret, Joyner, Halenda* – provides information on the morphological and structural properties of the catalysts, by studying nitrogen adsorption-desorption dynamics at -196 [°C]. Surface area, pore volume and pore size distribution (between 200 and 0.5 [nm]) can be determined with this technique. The instrument used for the measurements is a *Micrometrics Tristar 3000*, which evaluates the volumetric adsorption-desorption varying the relative pressure (P/P^0 = 0.001-0.98). The following expression correlates the relative pressure with the adsorbed gas volume:

$$\frac{1}{V_{ads}\cdot\left(\frac{P^0}{P}-1\right)} = \frac{C-1}{V_m C}\frac{P}{P^0} + \frac{1}{V_m C} \tag{3.4}$$

Where: P = partial pressure of the adsorbed gas

P^0 = vapour pressure

V_{ads} = adsorbed gas volume at STP

V_m = volume of a monolayer

C = non-dimensional constant, dependent of the adsorption enthalpy

The surface area is linked to the monolayer volume by this equation:

$$S_{TOT} = \frac{V_m N_{AV} O A}{V_{ads}} \tag{3.5}$$

being A the cross section area of the molecule gas probe (0.162 [nm^2]).

The so-called Kelvin equation (Eq. 3.6) correlates the relative pressure to the curvature radius of the meniscus formed by the adsorbed gas (r_m), which is in turn associated to the average pore radius (r_p) by Eq. 3.7.

$$ln\left(\frac{P}{P^0}\right) = -\frac{2\gamma V_{liq}}{RT}\frac{1}{r_m} \tag{3.6}$$

$$r_p = r_m + t \tag{3.7}$$

3.3.3 XRD

X-ray diffraction is a useful tool to identify the atomic and molecular structure of a crystal: it provides information on the crystalline phases of the catalyst sample. The emitted X-radiation impacts on the catalyst surface, producing a constructive interference with the vibration frequencies of the catalyst only when the so-called Bragg's law is satisfied:

$$n\lambda = 2d \cdot \lambda sin\theta \qquad (3.8)$$

Where: λ = wave length of the radiation
θ = existing angle between the crystalline plane and the radius
d = inter-planar spacing

The result is a spectrum whose peaks are linked to the crystallite concentration and dimension (D) by the so-called Scherrer equation:

$$D = \frac{k\lambda}{\beta_{hkl} cos\theta} \qquad (3.9)$$

Where k is a constant and β is a parameter associated with the half-height length of the peak of the reflection *hkl*. The instrument used for the measurements is a *PW 1050/70* which employs a Cu-Ka X-ray source. As the spectrum represents the composition of the whole catalytic material, it becomes necessary to operate a difference between spectra to identify the active phase: in particular, the support spectrum is subtracted from the catalyst spectrum.

A typical result of the analyses is shown in Figure 3.19:

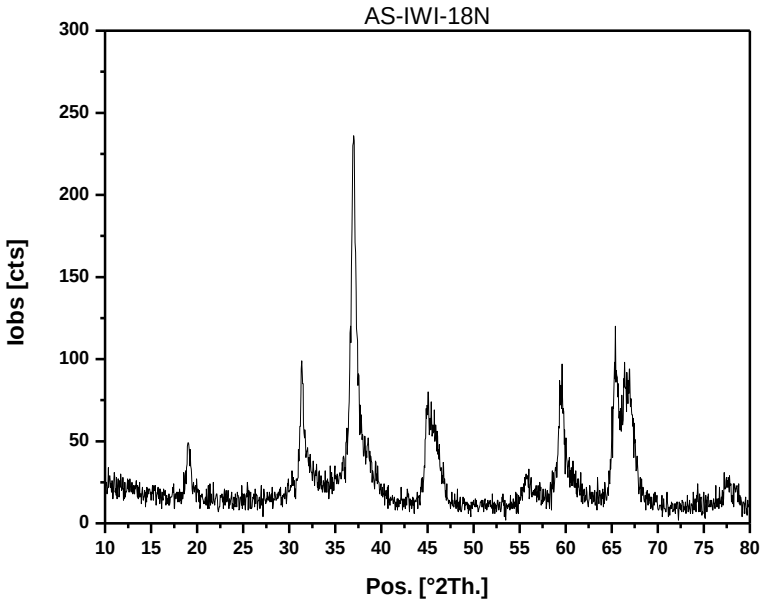

Figure 3.19: Typical XRD spectrum of a calcined catalyst

3.3.4 In situ TPR

The *Temperature Programmed Reduction* (TPR) is a common tool used in heterogeneous catalysis to determine catalyst reducibility as a function of temperature. In Co-based Fischer-Tropsch synthesis, TPR analyses provide precious information concerning the reduction steps which cobalt catalysts undergo during activation.

The TPR analyses are carried out in situ, by making some adjustments on the rig: particularly, the glass condenser downstream is substituted with the soda-lime trap, which prevents water to reach the gas chromatograph, and the analysis method of the latter is changed into short time analyses, which result in a well-defined H_2 consumption profile. Furthermore, the reactor loading is slightly different: from the bottom, the first 8.5 [cm] are filled with quartz wool, over which 200 [mg] of undiluted catalyst are blocked below an additional layer of quartz wool. In this way, the catalyst bed lays into the isothermal section. The K-type thermocouple is then carefully placed in the centre of the catalyst bed and the reactor is filled up with α-Al_2O_3 powder. It is then positioned vertically into the oven and connected to the gas line: as during catalyst testing, a leak test follows.

The TPR analyses are performed at two different conditions.

The first experiment is a TPR performed on to the calcined sample, aiming to observe the reducibility profile of the catalyst. Experimentally, a gas mixture of 5% H_2 diluted in Ar (20 [Ncc/min]) is fed through *IDR2* line to the reactor and the system is gradually (5 [°C/min]) heated up to 950 [°C]. A typical result of this experiment is shown in Figure 3.20:

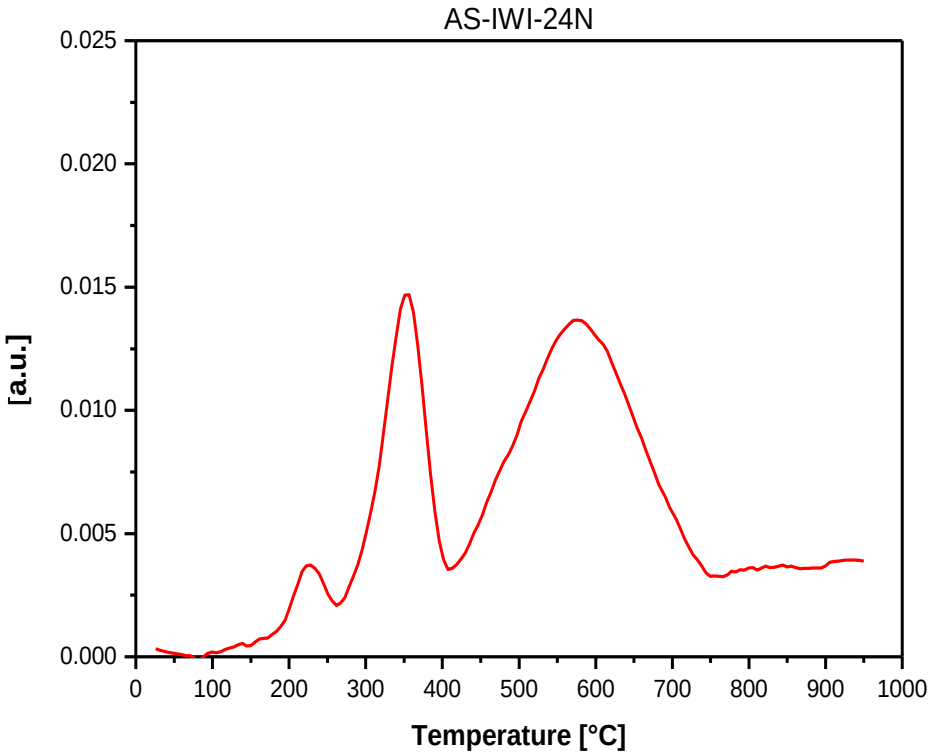

Figure 3.20: Typical result of a TPR analysis on a calcined sample

Chapter 4 – Influence of Pt Deposition Order on Conventional Co/γ-alumina Catalysts

Improvement in catalyst design and performances is crucial for Fischer-Tropsch process intensification. FT catalysts normally comprise a porous support, an active phase and a promoter; the choice of materials used for each role as well as their relative amount, deposition order and pathways represents the core of catalyst optimization. In this chapter, the influence of promoter deposition order is investigated in Co/Pt/γ-Al_2O_3 catalysts. As of today, the literature on this topic is rather scarce as only one work of interest can be accounted. In this study, *Cook et al.* [1] examined the effect of promoter deposition order on cobalt-based Fischer-Tropsch catalysts in terms on noble metal distribution, Co crystallite size, Co reducibility and catalyst activity. The two deposition pathways adopted are the following:

- Sequential deposition (seq-dep): according to the desired loading, the cobalt precursor is deposited in one or more steps separated from NM (*Noble Metal*) deposition;
- Co-deposition (co-dep): cobalt precursor and NM promoter are jointly deposited at least in one step and calcined together;

In the paper, three different promoters, namely platinum, ruthenium and rhenium were examined but, since our work is focused on Co/Pt/γ-Al_2O_3, only Pt promotion is hereby reported. The precursors used for catalyst preparation were cobalt-nitrates for the active phase and Pt-chloride salts for the NM: lanthanum was added as a support stabilizer. Promoted 25% Co/La/γ-Al_2O_3 catalysts were prepared by a three-step wet impregnation in the case of co-deposition and by a four-step impregnation for sequential deposition, being the first two steps identical in both deposition techniques. Noble metal loading was kept constant at 0.5 wt.%.

Cook et al. [1] showed evidence of the influence of deposition order on several properties such as crystallite diameter after calcination and after reduction (in brackets), *Extent Of Reduction* (EOR), Co dispersion (%D) and turnover frequency (Table 4.1). Conversely, significant effects did not appear neither in TPR nor in surface area. No notable deposition order effect in either NM oxidation

state or bonding was observed. What may seem inconsistent is the fact that EOR for the co-dep catalyst are substantially lower than those for the seq-dep catalysts even if TPR profiles appear to be the same (Figure 4.1). This may come from the fact that TPR profiles are obtained over a relatively short period of time while EOR data reflect longer times (i.e. 16 [h] under 100% H_2 flow).

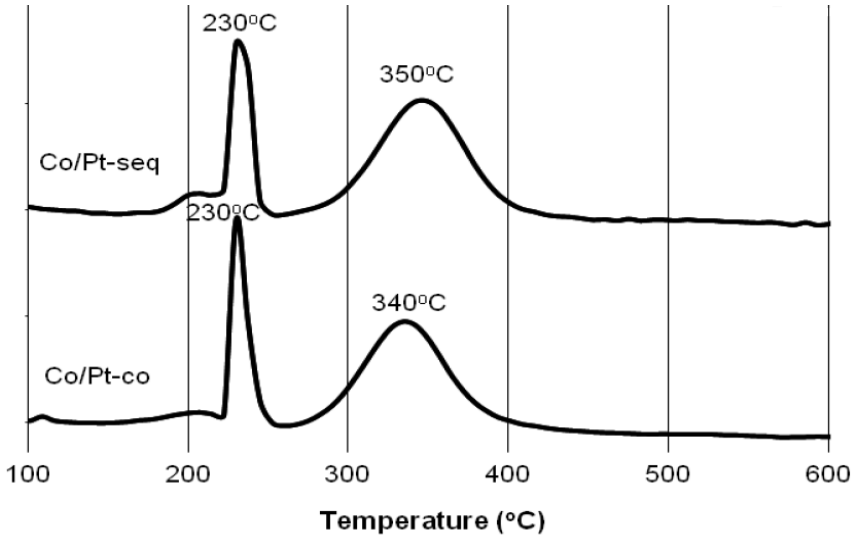

Figure 4.1: TPR profiles for co-dep and seq-dep catalysts

After calcination, cobalt crystallite sizes are larger for co-dep than for seq-dep, contrary to what expected based on the number of thermal treatments. Seq-dep catalysts undergo one more calcination step with respect to co-dep, thus advocating more Co agglomeration. It is suggested that the acidity of the co-dep solution may lead to Co aggregation rather than single particles formation.

Table 4.1: Surface area, diameter of cobalt crystallites after calcination and after reduction (in brackets), TPR 2nd peak temperature, extent of reduction (EOR) and turnover frequency (TOF) values for the unpromoted and Pt-promoted samples [1]

	Surf area [m^2g^{-1}]	**Co crystallite size**	**%D**	**TPR (2nd peak)**	**EOR [%]**	**TOF x10^3 [s^{-1}]**
Co-dep	99	13.6 (4.3)	18.8	230 °C (340 °C)	77	10.9
Seq-dep	98	9.2 (8.0)	16.1	230°C (350 °C)	91	5.37
Co	103	5.1 (4.7)	9.6	-	42	-

Given the fact that the influence of noble metal deposition order on catalytic performances is relevant, we aim to better clarify in our work its mechanisms and effects, by studying the deposition in a slightly different way. Following sequential deposition, in our preparation method Pt was deposited in two manners: directly on the support, before the very first Co deposition, or after the last one. Furthermore, cobalt load was varied to investigate how the hydrogen spillover mechanism, activated by platinum, could be influenced by it.

For each catalyst tested, three configurations were prepared:

- *NoPt*, unpromoted
- *PtDOWN*, promoted with Pt deposited directly on the support
- *PtUP*, promoted with Pt deposited after cobalt

4.1 Catalyst preparation

The catalysts prepared are cobalt-based supported on stabilized γ-Al_2O_3. Cobalt loading was varied (12,18,24 wt.%) while Pt loading was kept at 0.1 wt.%.

4.1.1 Stabilized alumina

Stabilized γ-Al_2O_3 was prepared via *Incipient Wet Impregnation* (IWI) of the support with an aqueous solution containing the cobalt precursor salts. It is well known [2] that part of the active cobalt tends to interact with the support forming mixed species in the form of hardly reducible cobalt-aluminates (Figure 4.2). For this reason, support stabilization was performed as the first step so that all the cobalt subsequently impregnated could be available during reaction; 5.7 wt.% cobalt loading, named *sacrificial cobalt*, was used. The impregnating solution was an aqueous solution of cobalt salts in the form of $Co(No_3)_2 \cdot 6H_2O$ (*Sigma Aldrich*, purity = 98%). After impregnation the catalyst was dried in an oven at 120 [°C] for 1 [h] (heating rate 0.6 [°C·min^{-1}]) and then calcined following a two-step ramp: 120-450 [°C] for 1 [h] (heating rate 2.2 [°C·min^{-1}]), then 450-900 [°C] for 4 [h] (heating rate 1.5 [°C·min^{-1}]). Aim of these procedures was to remove water and volatile compounds of the support and to fix cobalt on the alumina pellets in the form of ($CoAl_2O_4$). The acronym given to the stabilized support is "AS".

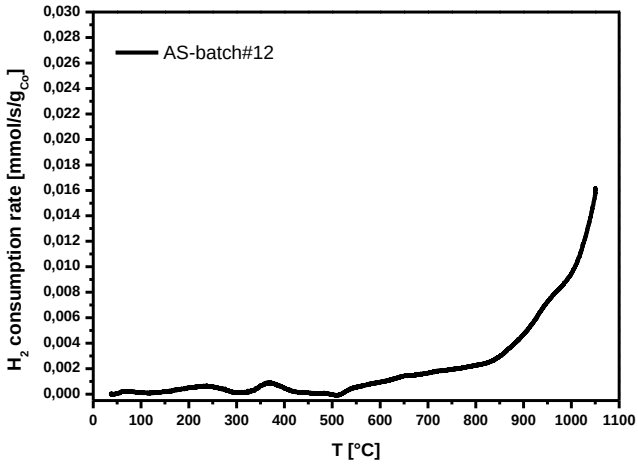

Figure 4.2: Hydrogen consumption rate for Stabilized Alumina (AS). Reduction of cobalt-aluminates occurs at very high temperatures

4.1.2 AS-IWI-24N

The catalysts were prepared via IWI method with $Co(No_3)_2 \cdot 6H_2O$ as a precursor. As the limit of solubility of cobalt precursor in water is 1.04 [$g \cdot ml^{-1}$], the impregnation of the desired cobalt loading was performed in four steps of 6 wt.%, each one followed by drying at 120 [°C] for 2 [h] and calcination at 400 [°C] for 4 [h].

It is thought that the calcination procedure can be shortened without any effect on catalytic performances. Therefore, a *flash calcination* was often preferred after each cobalt deposition step, consisting of a ramp of 2 [$°C \cdot min^{-1}$] up to 500 [°C] and 10 [min] dwell at such temperature.

4.1.3 AS-IWI-24N-0.1PtUP

Platinum deposition was performed with a noble metal (NM) loading of 0.1 wt.% and occurred via impregnation of an aqueous solution of $Pt(NH_3)_2(NO_2)_2$ (*Sigma Aldrich*), which was performed after the four cobalt impregnation steps. After NM impregnation, the catalyst underwent drying at 120 [°C] for 2 [h] and calcination at 500 [°C] for 5 [h].

4.1.4 AS-IWI-24N-0.1PtDOWN

Platinum deposition was performed directly on the support, followed by drying at 120 [°C] for 2 [h] and calcination at 500 [°C] for 5 [h]. Cobalt was then deposited with the same procedures mentioned above.

4.1.5 AS-IWI-18N and AS-IWI-12N families

The procedures adopted for the preparation of these catalyst are the same described above. Being the cobalt loading 18 wt.% and 12 wt.% instead of 24 wt.%, the number of cobalt deposition steps was reduced to three and two respectively. Platinum deposition pathway was maintained unaffected.

4.2 Catalyst characterization

For the investigation of the morphological and structural features of the catalyst prepared, some characterization techniques were adopted.

- XRD (*X-Ray Diffraction*), to estimate the average cobalt crystallite diameter of the calcined catalyst;
- TPR (*Temperature Programmed Reduction*), allows to identify the temperatures of the different reduction steps thus giving information about catalyst reducibility;
- TPD (*Temperature Programmed Desorption)*, to investigate possible presence of residual cobalt nitrates on the catalysts.

A useful comparison between the catalysts comes from the TPR analyses. In Figure 4.3 and Figure 4.5 the catalysts with 24 wt.% of cobalt loading are gathered. Furthermore, in Figure 4.5 TPR profiles are displayed as single peaks after deconvolution, in order to allow an easier comparison. Two main features can be inferred from these analyses: the first one is related to the temperatures of the two reduction steps which account, respectively, for 25% and 75% of hydrogen consumption, according to the following stoichiometry:

$$Co_3O_4 + H_2 \rightarrow 3CoO + H_2O \quad (4.1)$$

$$CoO + H_2 \rightarrow Co^0 + H_2O \quad (4.2)$$

The second one is related to the total amount of adsorbed hydrogen, represented by the areas under the TPR curves.

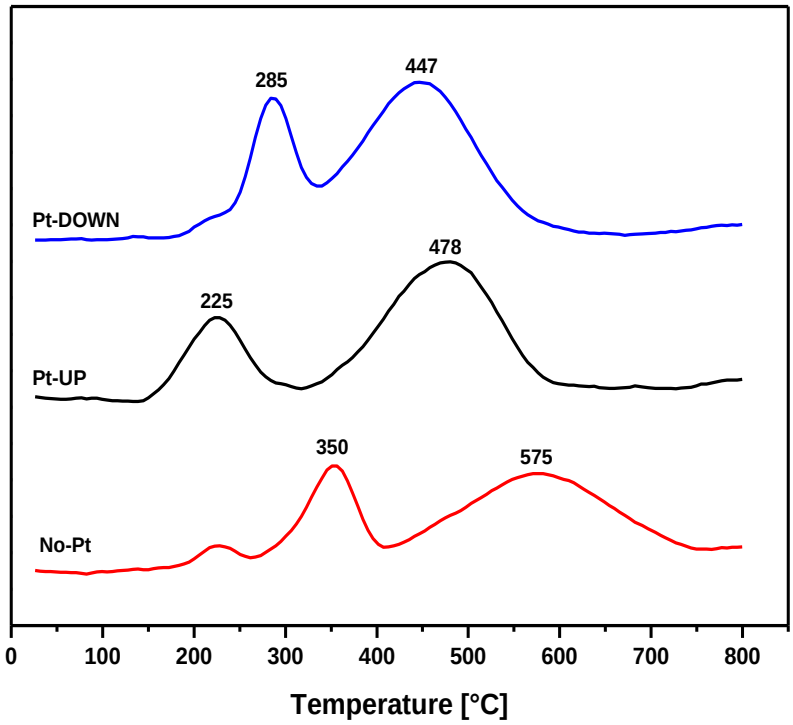

Figure 4.3: Comparison between TPR profiles of 24 wt.% catalysts

An eased reducibility due to the platinum effect is evident, as temperatures of the promoted catalysts are significantly shifted towards lower values for the two reduction peaks and the total adsorbed hydrogen is higher with respect to the unpromoted. Moreover, it is worth underlining that for a thorough comparison, also the temperature at which reduction peaks start growing has to be taken into account. From Figure 4.5, a better reducibility of *PtDOWN* can be ascribed to the fact that it has the highest formation of Co^0 active phase at any temperature above 300 [°C].

It was demonstrated in studies performed at the *University of Cape Town* (UCT) [4], by using catalysts from the same batches as ours, that despite calcined catalysts show identical particle size, reduced Co^0 display different particle diameters (Table 4.2). This is due to enhanced reducibility on promoted catalysts that allows even the smaller crystallites to be reduced thus shifting the average particle size towards lower values.

Table 4.2: Average particle size after calcination and after reduction

Catalyst	After Calcination [nm]	After Reduction [nm]
AS-IWI-24N	22	14
AS-IWI-24N-PtUP	21	11
AS-IWI-24N-PtDOWN	22	9

Increased reducibility of promoted catalyst, especially in *PtDOWN* configuration, is also validated by in situ XRD analyses of Figure 4.4 (UCT), as a higher metallic cobalt fraction can be observed at any temperature.

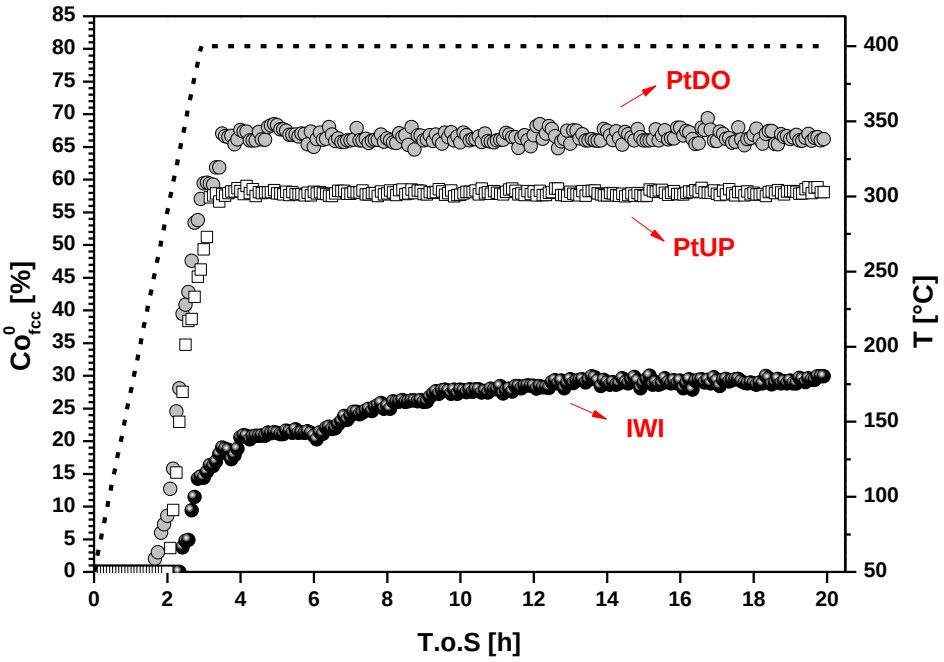

Figure 4.4: Co^0 fraction detected by in situ XRD performed at *University of Cape Town* (UCT) on 24 wt.% catalysts. "IWI" is the unpromoted catalyst

It is also worthwhile focusing on the differences between the two promoted catalysts. In fact, while the first reduction peak of AS-IWI-24N-0.1PtDOWN occurs at a higher temperature, a lower temperature is needed for the second peak to occur and the overall adsorbed hydrogen is higher. If hydrogen dissociation is the slow step of the reduction [3], it can be speculated that when platinum

is deposited as the last step (AS-IWI-24N-0.1PtUP), it lays on the external surface of the catalyst and, as it is more directly exposed to the H_2 flux it favors the reduction step $Co_3O_4 \rightarrow CoO$. Interestingly, the same trend is observed by in situ XRD analyses (UCT) showing the fast disappearance of the Co_3O_4 phase for the *PtUP* catalyst during the temperature ramp (Figure 4.6).

On the other hand, when the promoter is deposited directly on the support, the intimate contact between the latter and the noble metal favors hydrogen mobility via surface migration, thus facilitating the second step to occur.

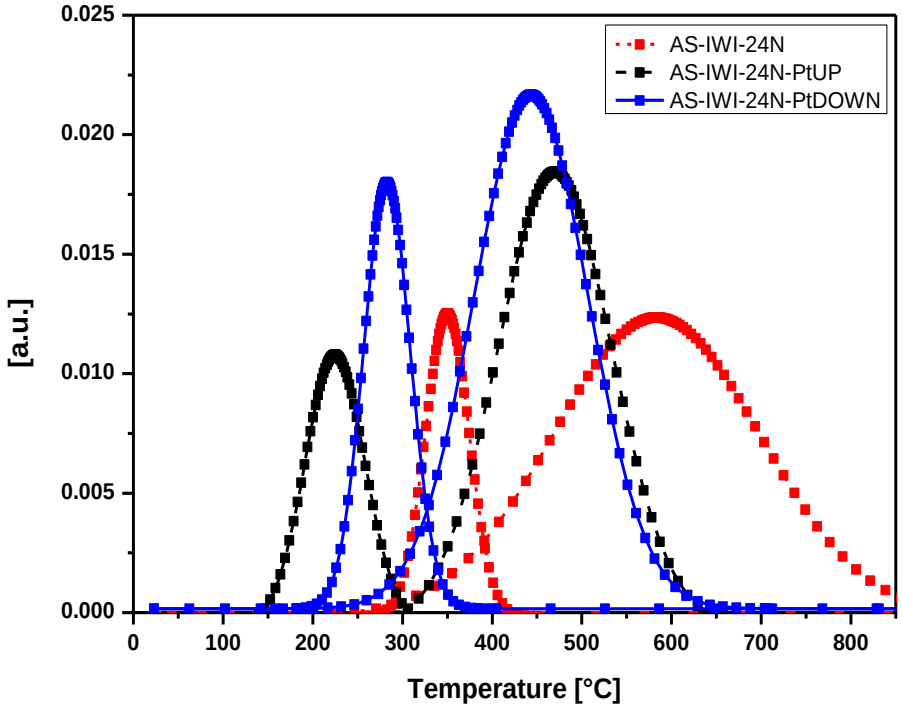

Figure 4.5: Comparison between the single reduction peaks, obtained after deconvolution (24 wt.% Co)

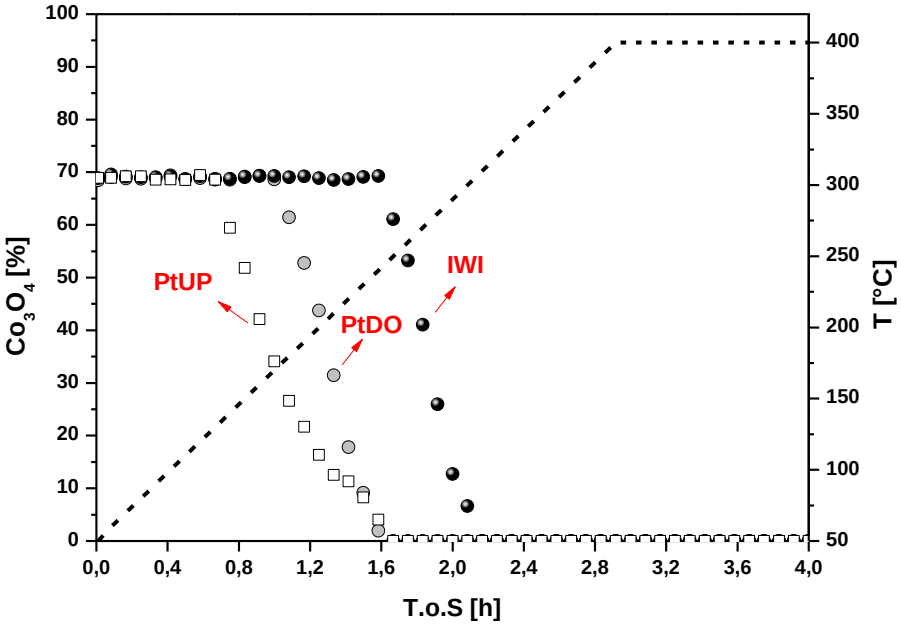

Figure 4.6: Co_3O_4 fraction detected by in situ XRD performed at *University of Cape Town* (UCT) on 24 wt.% catalysts. "IWI" is the unpromoted catalyst

Hydrogen spillover is thought as the most reasonable explanation for the increased reducibility of promoted samples and for the differences between promoted catalyst configurations. The ready availability of platinum on the external surface of the catalyst in AS-IWI-24N-0.1PtUP catalyst favors a quick hydrogen dissociation resulting in lower temperatures associated to the first reduction peak, while the proximity between platinum and support occurring in AS-IWI-24N-0.1PtDOWN helps spillover hydrogen to travel along the support thus resulting in an increased overall reducibility.

If the mechanism is the one described above, the difference between the two platinum deposition configurations may be influenced by the cobalt loading, as the latter may be imagined as a layer deposited on the support. In the case of *PtDOWN*, it covers the promoter too while, for *PtUP* catalysts, it is interposed between platinum and the support thus limiting the spillover that occurs via support migration.

To validate this conjecture, the same three configurations (*unpromoted*, *PtUP*, *PtDOWN*) were studied with a diminished cobalt loading. Promoted catalysts (AS-IWI-18N-0.1PtUP and AS-IWI-18N-0.1PtDOWN) still show better performances with respect to the unpromoted AS-IWI-18N,

both in terms of reduction temperatures and adsorbed hydrogen (Figure 4.7 and Figure 4.8). Moreover, with respect to the corresponding 24 wt.% samples, TPR profiles of 18 wt.% promoted catalysts become more similar one to the other as they differ in first peak temperatures by 43 [°C] and the second peak occurs at identical temperatures. Crystallite size after reduction and in situ XRD are not available but same trends are expected as for the 24 wt.% catalysts.

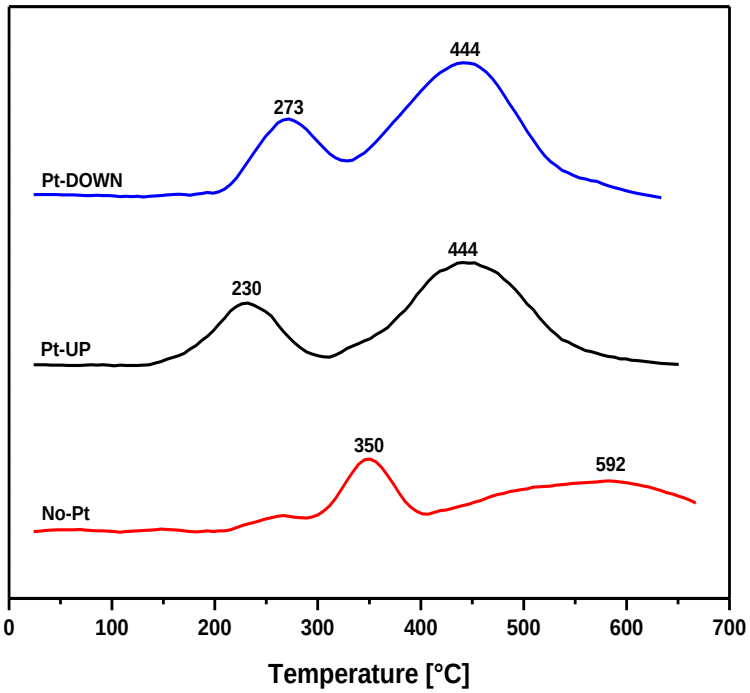

Figure 4.7: Comparison between TPR profiles of 18 wt.% catalysts

Figure 4.8 allows the same considerations previously explained for the 24 wt.% catalysts regarding position and shape of the peak temperatures. Given the high temperatures reached during TPR analyses, no cobalt in the form of CoO is expected to be found on catalyst surface, that is a complete reduction of the sample is always assumed. Nevertheless, in this case the unpromoted catalyst, despite having the same amount of cobalt as the promoted (18 wt.%), shows a lower overall hydrogen consumption (i.e. area below the two reduction peaks) which may be ascribed to the formation of cobalt aluminates. In fact, according to *Nabaho et al.* [3], who studied Co catalysts supported on unstabilized γ-Al_2O_3, cobalt-aluminates are formed from CoO species during TPR due to the high temperatures. It can be speculated that Pt reduces the apparent activation energy of the second reduction step thus allowing a higher fraction of small CoO particles, subjected to strong

support interactions, to be further reduced to Co^0 before undergoing high temperature transition to $CoAl_2O_4$. On the other hand, complete reduction for the unpromoted catalysts occurs at such high temperatures that it competes with cobalt aluminates formations. However, this phenomenon is restricted only to TPR analyses; as shown by in situ XRD analyses (Figure 4.9) carried out on the 24 wt.% catalyst family at the *University of Cape Town* (UCT), the hypothesis of a competition between the second reduction step and $CoAl_2O_4$ formation does not hold true at low temperatures, compatible with the ones employed for catalyst activation.

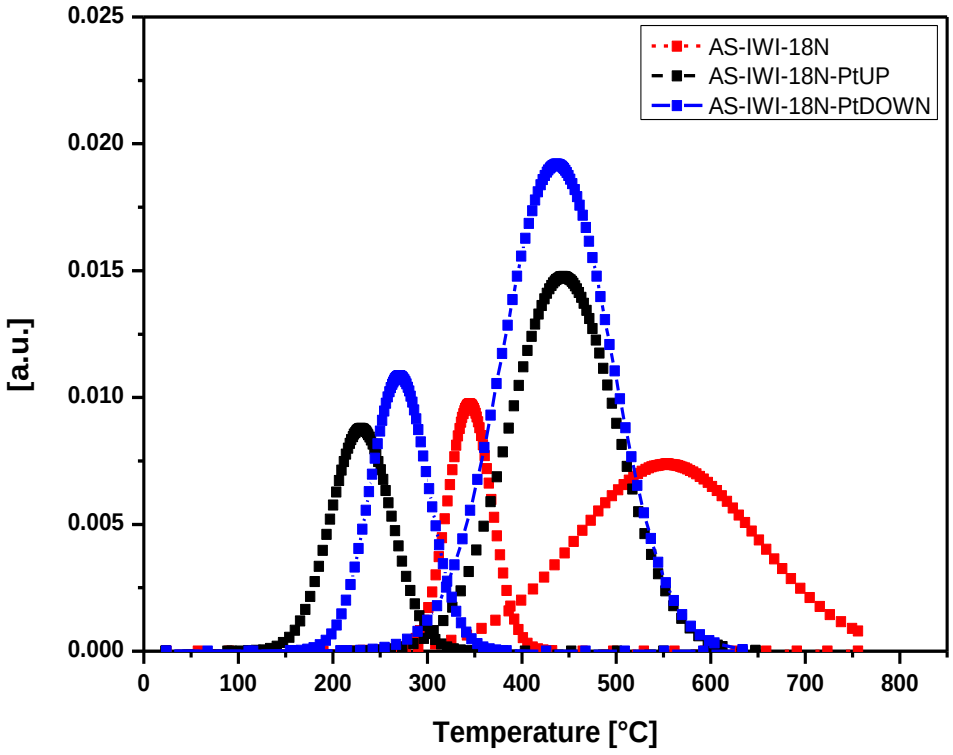

Figure 4.8: Comparison between the single reduction peaks, obtained after deconvolution (18% wt. Co)

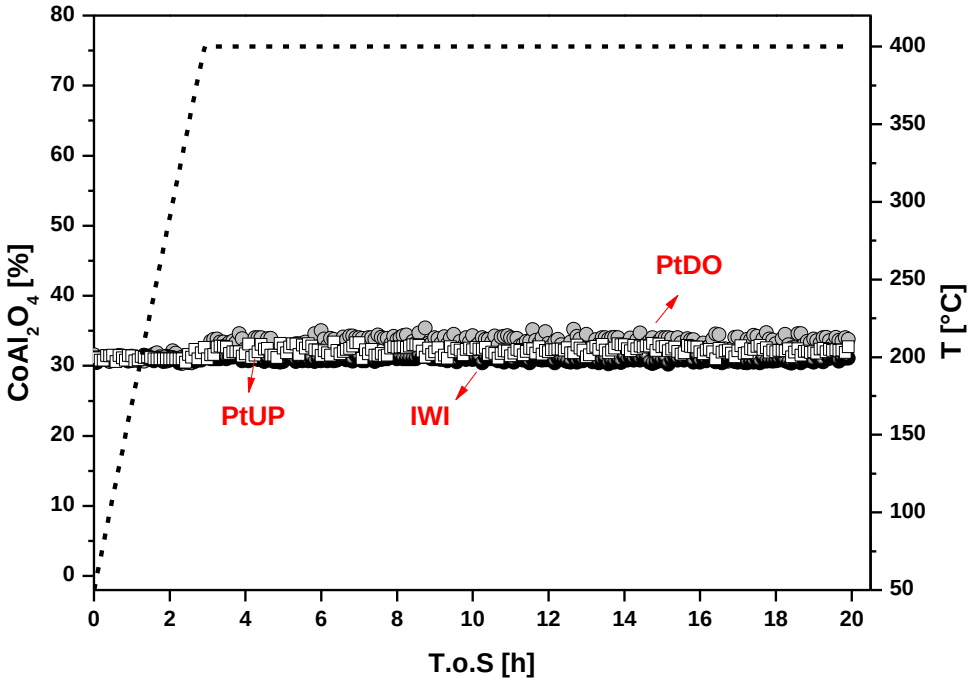

Figure 4.9: $CoAl_2O_4$ fraction detected by in situ XRD performed at UCT with 24 wt.% catalysts coming from the same batch. "IWI" is the unpromoted catalyst

Cobalt loading was further reduced to 12 wt.% for additional investigations. Promoted catalysts still show better reducibility than the unpromoted but, in this case, reduction temperatures are influenced by the deposition order (Figure 4.10 and Figure 4.11). As for 24 wt.%, a 30 [°C] difference is observed for the second reduction step between *PtDOWN* catalyst and the corresponding *PtUP*.
It is possible that in this configuration cobalt particles are so small and difficult to be reduced that the deposition order effect is emphasized.

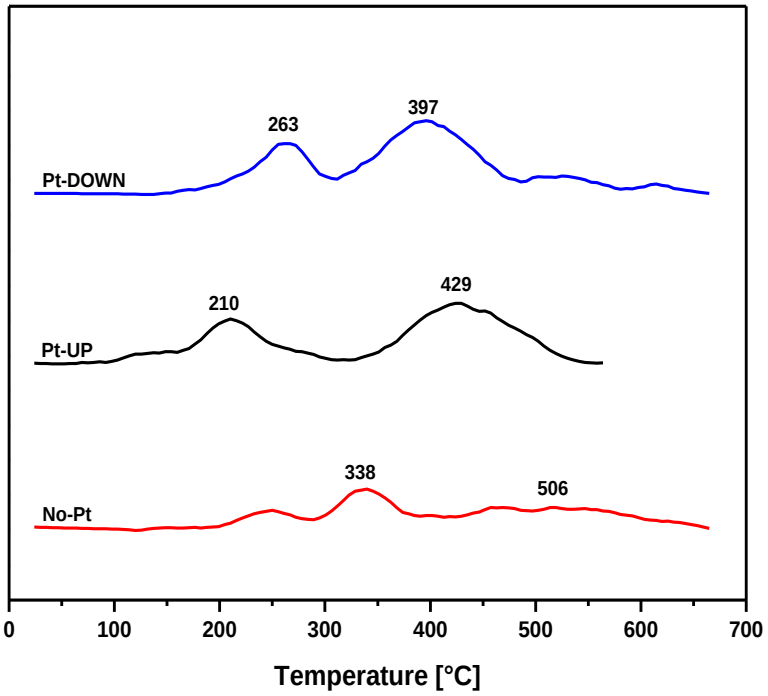

Figure 4.10: Comparison between TPR profiles of 12 wt.% catalysts

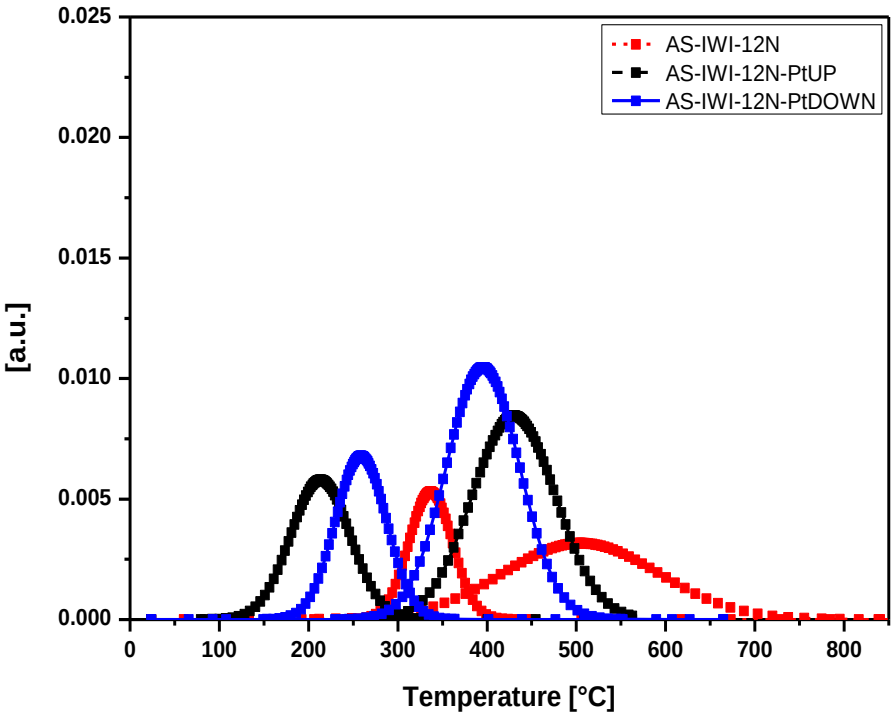

Figure 4.11: Comparison between the single reduction peaks, obtained after deconvolution (12 wt.% Co)

Figure 4.12 shows a comparison between deconvolution peaks of the three *PtDOWN* catalysts (AS-IWI-24N-0.1PtDOWN, AS-IWI-18N-0.1PtDOWN, AS-IWI-12N-0.1PtDOWN). The peak start does not seem influenced by the cobalt loading. The activation energy required to start the single reduction steps is only influenced by the deposition order and is completely insensitive to variations in cobalt loading. Once it is overcome, the peak starts to grow with a profile that depends on a number of factors as cobalt loading, particle size and distribution, Pt/Co ratio (Figure 4.13). It is worthwhile noticing that the two peaks of reduction are influenced in different manners. The first peak is well established in literature to occur readily and completely, so it can reflect the differences in cobalt loading. This does not stand true for the second step, which is known to be more difficult to occur and cluster size dependent. AS-IWI-18N-0.1PtDOWN peak seems to be higher than expected, almost following the AS-IWI-24N-0.1PtDOWN profile. This could be due to a combination of factors which make AS-IWI-18N-0.1PtDOWN more easily reducible. First, crystallite size, which decreases with cobalt loading, may be still not small enough to limit the sample reducibility. Furthermore, a higher Pt/Co ratio with respect to the AS-IWI-24N-0.1PtDOWN allows a better overall reducibility. In conclusion, for AS-IWI-18N-0.1PtDOWN the advantage of a higher Pt/Co ratio may be higher than the disadvantage of smaller crystallite size. Conversely, in AS-IWI-12N-0.1PtDOWN these two effects are balanced, as the area below the second peak is approximately half of the AS-IWI-24N-0.1PtDOWN, as expected.

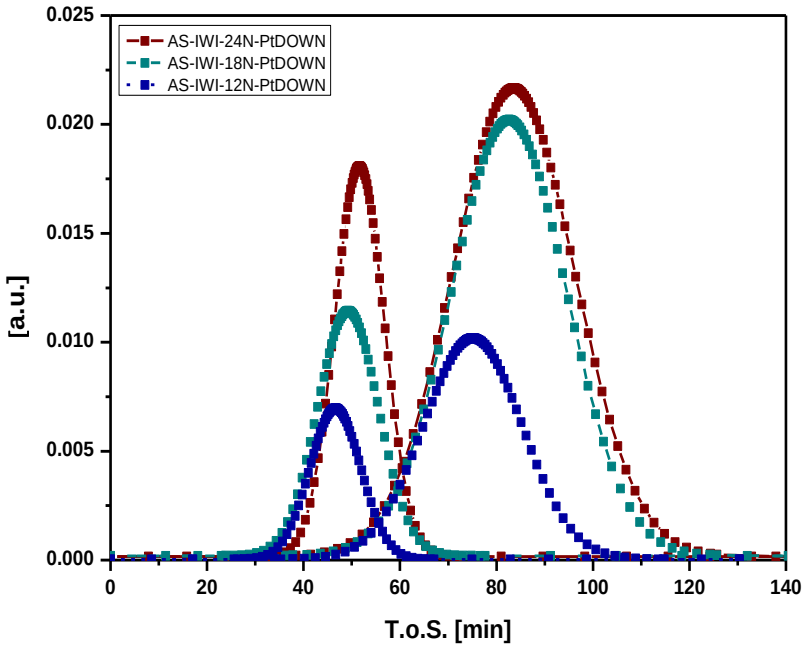

Figure 4.12: Deconvoluted reduction peaks for *DOWN-promotion* catalysts at every cobalt loading

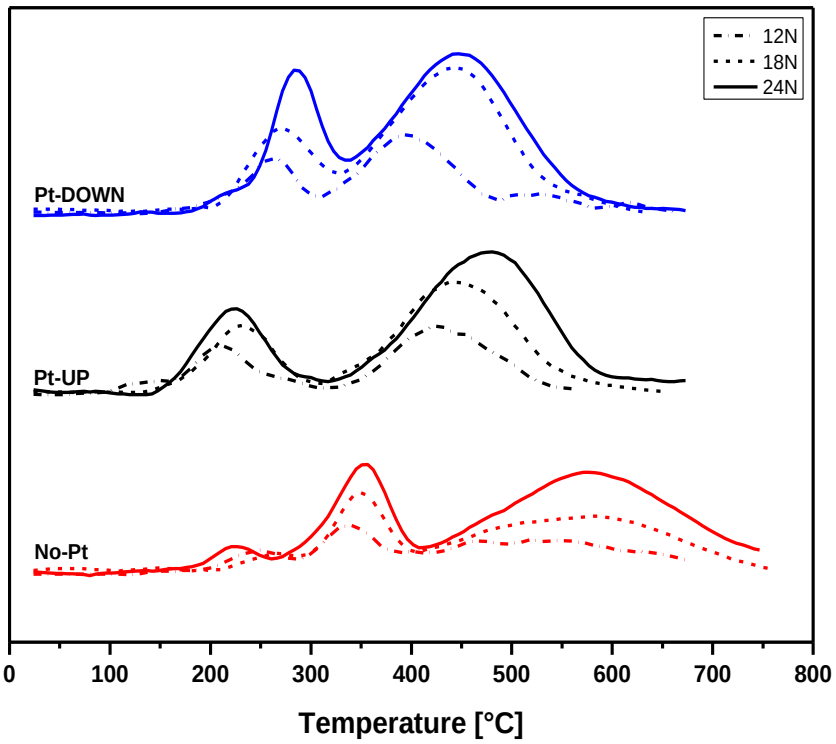

Figure 4.13: Overall comparison between TPR profiles for all the catalyst families

In TPR profiles a small first peak appears in the unpromoted samples at around 250 [°C], same temperature at which a 'left-shoulder' is noticeable on the first peak of the *PtDOWN* catalysts, especially at higher cobalt loading where the phenomenon is clearer. It is suggested in the literature that this peak/shoulder is not related to a stoichiometric reduction step but can be ascribed to the decomposition of cobalt-nitrates [5]. Since the samples have been prepared via *flash calcination*, both the unpromoted and *PtDOWN* catalysts did not undergo a complete calcination of the cobalt phase. Platinum, instead, is calcined by following the standard procedure (5[h] at 500 [°C]). Since for the *PtUP* catalyst platinum calcination occurs as the last step, it also helps to achieve a complete cobalt calcination.

To verify this assumption, samples were calcined by following standard procedure to ensure the absence of a peak around 250 [°C], as in Figure 4.14. In addition, TPD analyses, carried out in an inert environment (100% He), validated this hypothesis showing that the release of nitrogen monoxide, linked to nitrate decomposition, occurs at these temperatures for AS-IWI-24N and AS-IWI-24N-0.1PtDOWN (Figure 4.15).

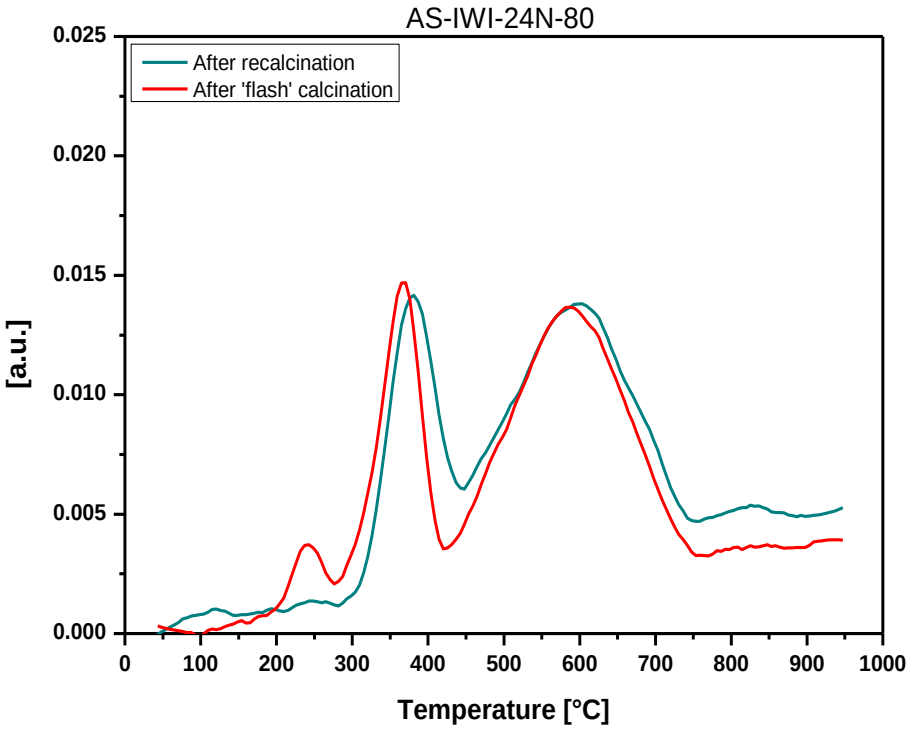

Figure 4.14: Effect of calcination procedure on TPR profile

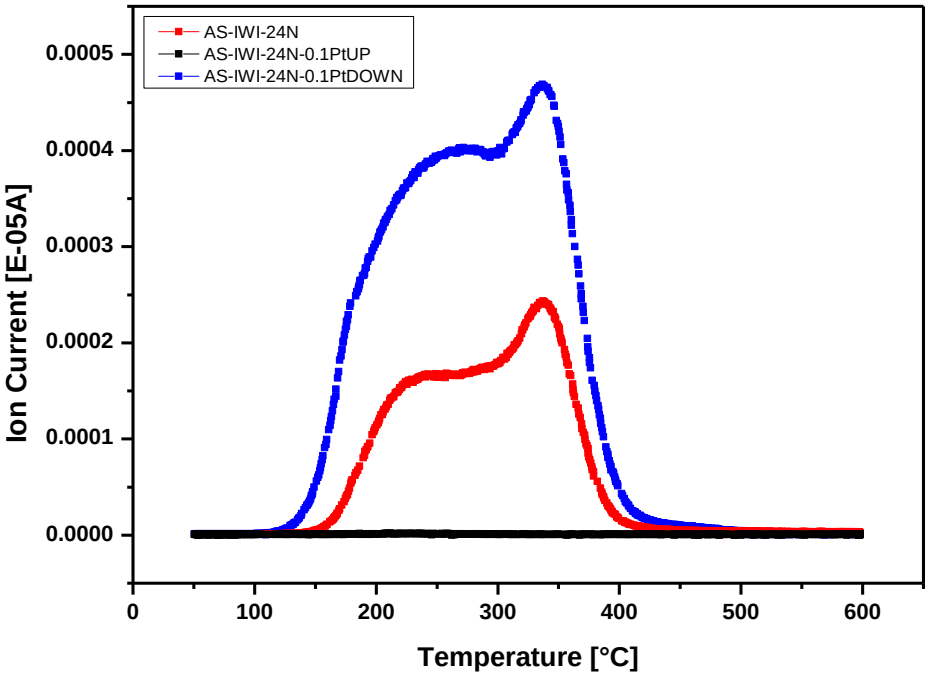

Figure 4.15: Nitrogen monoxide signal in TPD analysis

4.3 Catalytic tests at atmospheric pressure

Activity tests were performed to analyze and compare the catalytic performances of the different catalysts and try to understand, if present, the role of platinum deposition order.

Low pressure testing consists of two parts: catalyst activation and reaction. Catalyst activation treatment was reduction in H_2 (50 [Ncc/min]) for 13 [h] and 30 [min] at 400 [°C]. Standard reaction conditions used were 1 [atm], H_2/CO = 2.05, 240 [°C] and a $GHSV_{(H2+CO)}$ of 5104 [Ncc/g_{cat}/min]). The outlet composition was analyzed via micro-GC. Further details are provided in Chapter 3.

4.3.1 CO conversion

For all the three catalyst families, promoted samples show higher activities with respect to the corresponding unpromoted, in agreement with the lower reduction temperatures observed in TPR analyses.

The influence of Pt deposition order increases when increasing the cobalt loading: in particular, AS-IWI-24N-0.1PtDOWN shows significantly higher activity than the other two 24 wt.% cobalt catalysts (Figure 4.17). A number of factors can be thought to influence this behavior. First, reducibility was shown to be higher in *PtDOWN* catalysts, but not enough to justify the huge improvement in performances. It may be that the cobalt layer has a protective effect towards the noble metal previously deposited on the support, thus allowing it to act as a promoter during reaction. However, the debate on platinum being active also during reaction is still ongoing in the literature, as noble metal promotion does not seem to significantly influence catalytic activity as such [6-7]. Furthermore, a role of the average crystallite diameter of the reduced catalyst cannot be excluded, since it was highlighted from *Cook* et al. [1] that remarkable changes in crystallite size may occur during reduction. To investigate this aspect, in situ XRD analyses are carried out at conditions closer to the ones adopted during catalyst activation (400 [°C] for 17 [h]); this way, the cobalt phases detected are likely to be the ones actually present on the reduced catalyst. Figure 4.4 and Figure 4.16 show that a consistent fraction of cobalt oxide still has to be reduced on the unpromoted catalyst, thus resulting in lower activity; on the other hand, *PtDOWN* has the highest amount of Co^0. This suggests the higher capability of this catalyst to reduce even the smallest CoO crystallites, shifting the Co^0 size distribution towards lower values. The crystallite diameter

obtained for the *PtDOWN* lays in the optimal range 6 ÷ 10 [nm] reported in the literature [8-9], providing additional clarification for the enhanced activity.

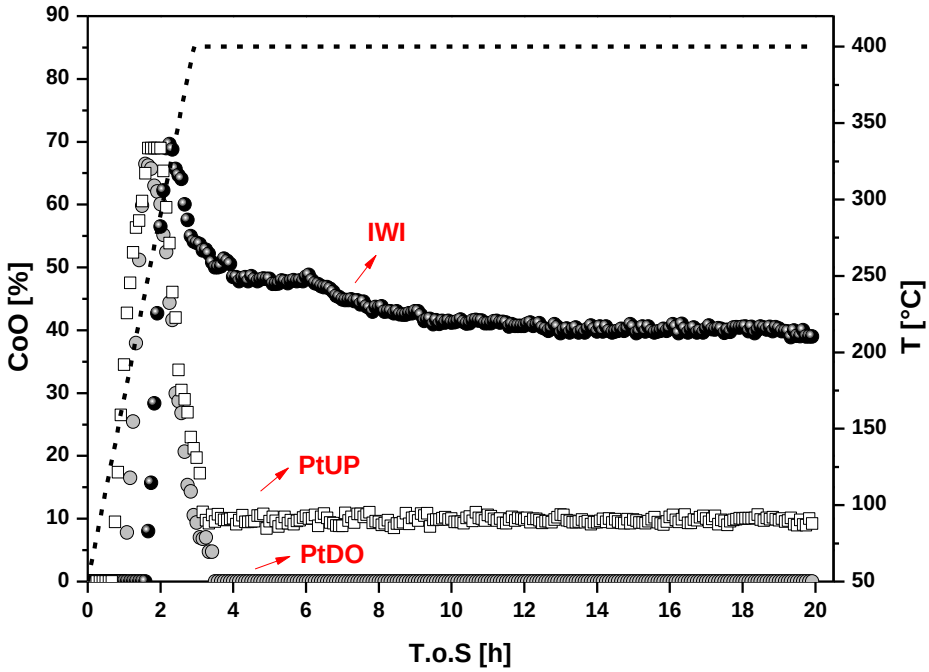

Figure 4.16: CoO fraction detected by in situ XRD performed at University of Cape Town with catalysts coming from the same batch. "IWI" is the unpromoted catalyst

It is interesting to notice that the difference between the two NM deposition orders decrease when reducing the cobalt loading (Table 4.3). The thinning of the cobalt layer as well as increased Pt/Co ratio and smaller particle size are suggested to reduce the influence of platinum deposition order. It is difficult to unequivocally determine which aspect plays the major role, as they cannot be divided. In particular, the 12 wt.% promoted catalysts show almost identical activity. This may be ascribed both to the above mentioned factors and to the low temperatures required for their reduction to occur. In fact, despite a remarkable difference among the two (Figure 4.10), the reduction temperatures are very close to the one employed during catalyst activation (400 [°C]); this may suggest complete reduction for both samples prior to the reaction phase, which is reflected in equal activities.

The results obtained for the Pt-promoted 18 wt.% samples reflect an intermediate situation between the ones discussed for two families, 24 wt.% and 12 wt.%.

A further observation concerns the values of CO conversion relative to the unpromoted catalysts (Figure 4.17). From a mere proportion, an intermediate activity value of AS-IWI-18N between AS-IWI-24N and AS-IWI-12N should be expected. However, AS-IWI-18N shows more similar values to the ones obtained in the most cobalt loaded configuration. It may seem to take advantage from a crystallite size which is not too small to prevent reduction but small enough to improve catalytic performances.

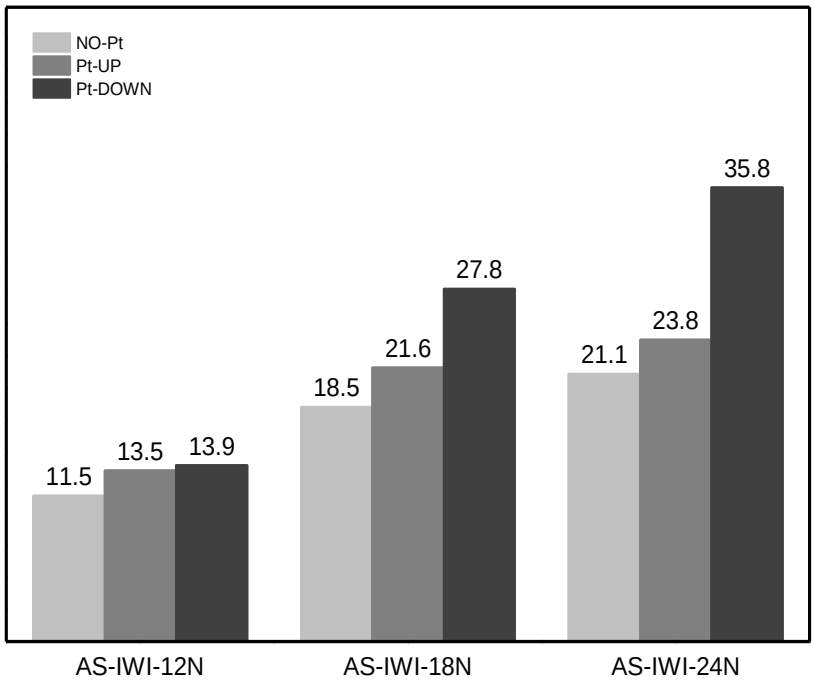

Figure 4.17: CO conversion [%]

Table 4.3: Variation between the promoted catalysts with respect to the unpromoted at different cobalt loadings

Catalyst Family	PtUP	PtDOWN
AS-IWI-12N	+17.4%	+20.8%
AS-IWI-18N	+16.8%	+50.3%
AS-IWI-24N	+12.8%	+69.7%

4.3.2 CH_4 selectivity

Even though in real Fischer-Tropsch conditions (30 [bar] and 210 [°C]) methane selectivity are kept very low, at atmospheric pressure CH_4 accounts for almost half of the global selectivity thus being one of the most important parameters. For all the three families, the highest methane selectivity is obtained with a promoted catalyst even if no consistent trends can be detected (Figure 4.18). As observed by *Jacobs et al.* [10], platinum is known to have an hydrogenating effect also during FT reaction as it may facilitate hydrogen dissociation thus favoring chain termination reactions. However, the influence on methane selectivity does not seem to be very high. It has been reported in literature that methane formation may follow two different paths on Co catalysts -11]. One is methanation, where hydrogen reacts with active carbon or methylene; the second one is the conventional FT polymerization that may occur through carbide mechanism. Especially at low pressure conditions, methanation is expected to account for the majority of methane yield thus limiting the influence on chain termination rate [12].

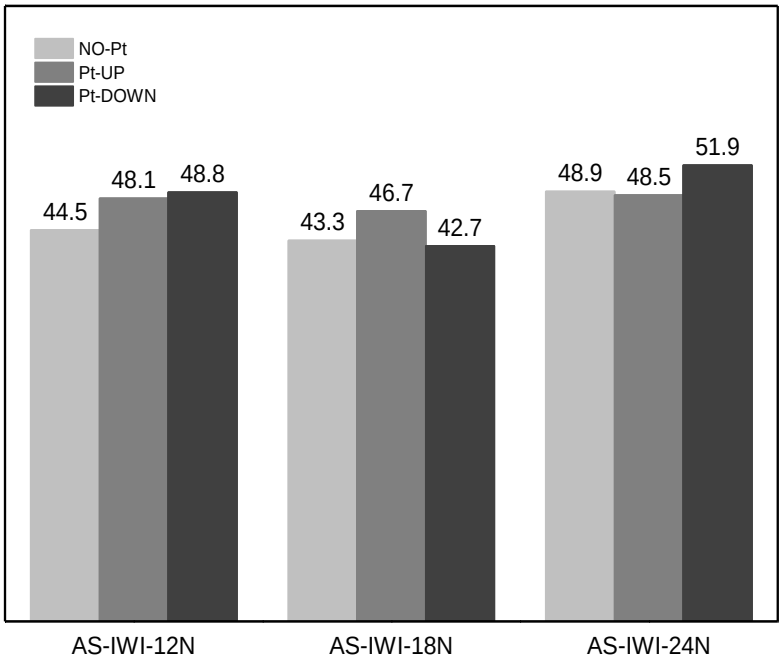

Figure 4.18: CH_4 selectivity [%]

4.3.3 CO_2 selectivity

CO_2 selectivity provides important information about the activity towards *Water-Gas Shift*, considered as a parasitical reaction with respect to FTS.

For each family, promoted catalysts show higher CO_2 selectivity values (Figure 4.19). Since water, produced during FT reaction, is a reactant in the WGS, higher CO conversions contribute to an increase in WGS (Figure 4.20). This explains the higher difference between the promoted catalysts of the *24N-family*, as AS-IWI-24N-0.1PtDOWN showed a remarkable increase in CO conversion.

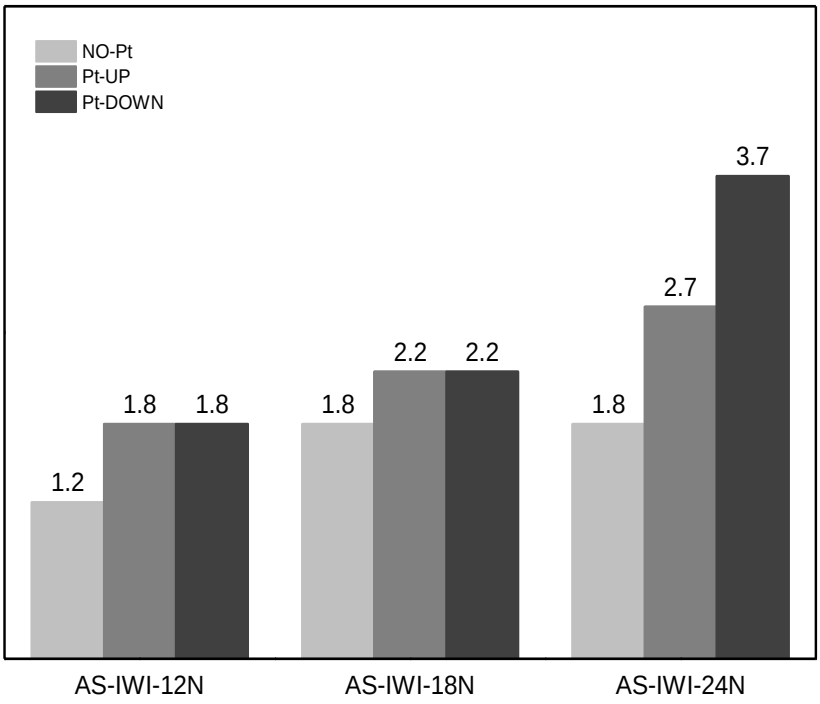

Figure 4.19: CO_2 selectivity [%]

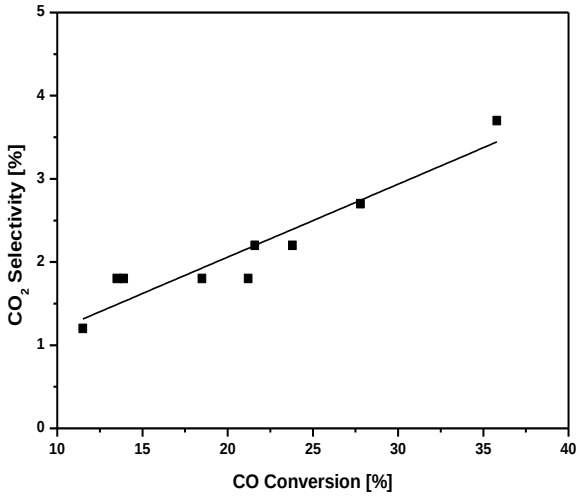

Figure 4.20: CO_2 selectivity as a function of CO conversion

4.3.4 C_2 selectivity

The results shown in Figure 4.21 are the overall C_2 selectivity, sum of C_2 olefin and paraffin. No particular differences or interesting trends can be highlighted. This is not surprising as usually C_2 species are involved in complex readsorption mechanisms (see Chapter 1).

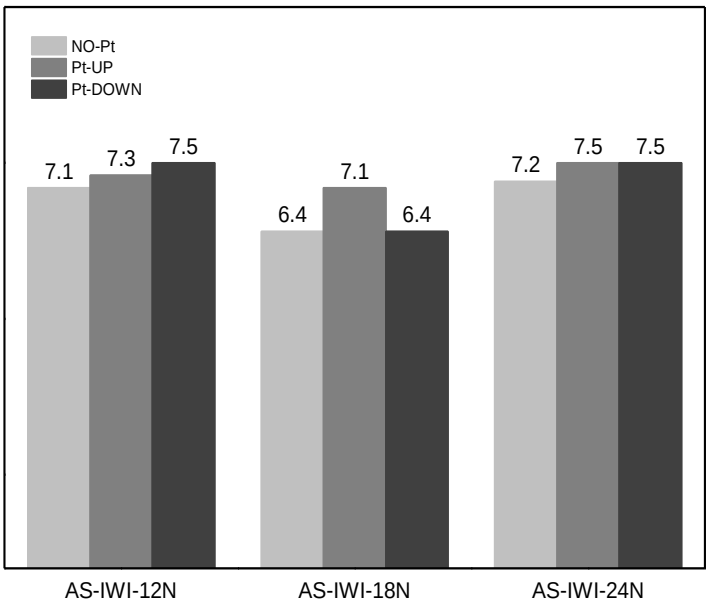

Figure 4.21: C_2 Selectivity [%]

4.3.5 C_3 selectivity

Promoter effect becomes more evident with C_3 species (Figure 4.22 and Figure 4.23), which are not deviating from the product distribution and are present in significant amounts of paraffins and olefins at atmospheric pressure conditions. Promoted catalysts seem to favor paraffin formation while olefins are formed in larger amounts on the unpromoted catalysts. This is even clearer considering the olefin to paraffin ratio (Figure 4.24), where Pt effect is significant.

It is worth recalling that Pt loading is always 0.1 wt.% for all the promoted catalysts. Due to the increased Pt/Co ratio, the promotion effect is more evident at lower cobalt loadings, where promoted catalysts show higher hydrogenating activity with respect to the corresponding unpromoted.

For what concerns Pt promoted catalysts, the difference in trends reflects the one observed for Co conversion (Figure 4.17). Higher activities correspond to an increased hydrogenating behavior, which reflects in a more paraffinic C_3 mixture.

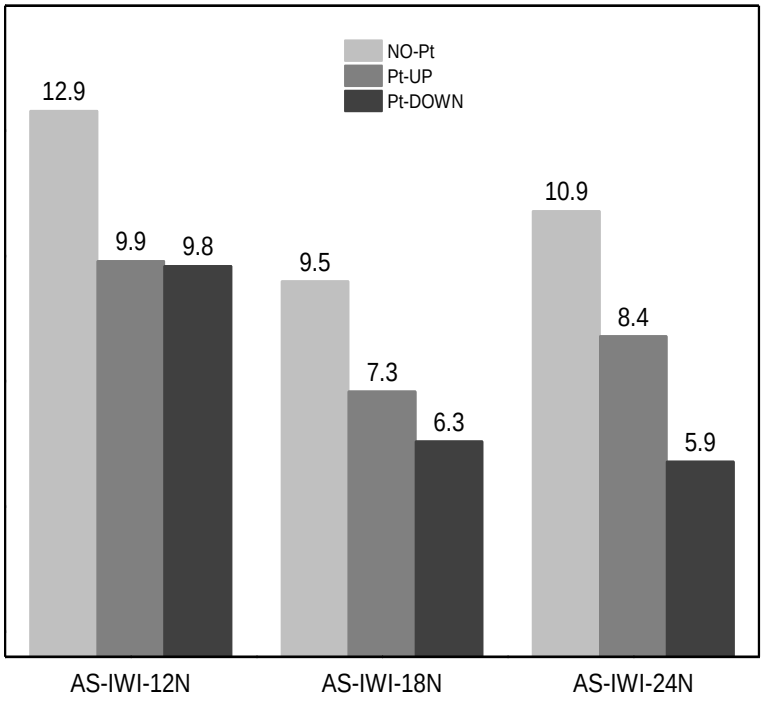

Figure 4.22: C_3-olefin selectivity [%]

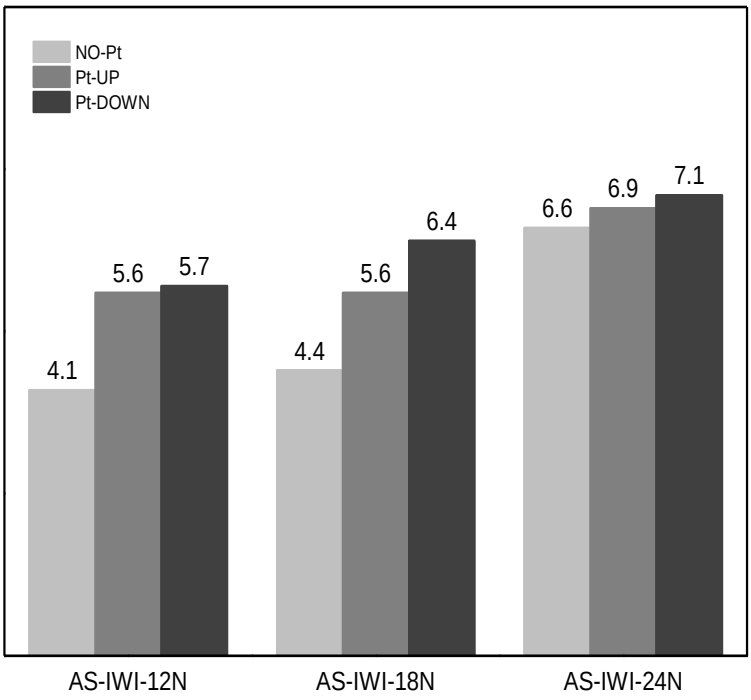

Figure 4.23: C_3-paraffin selectivity [%]

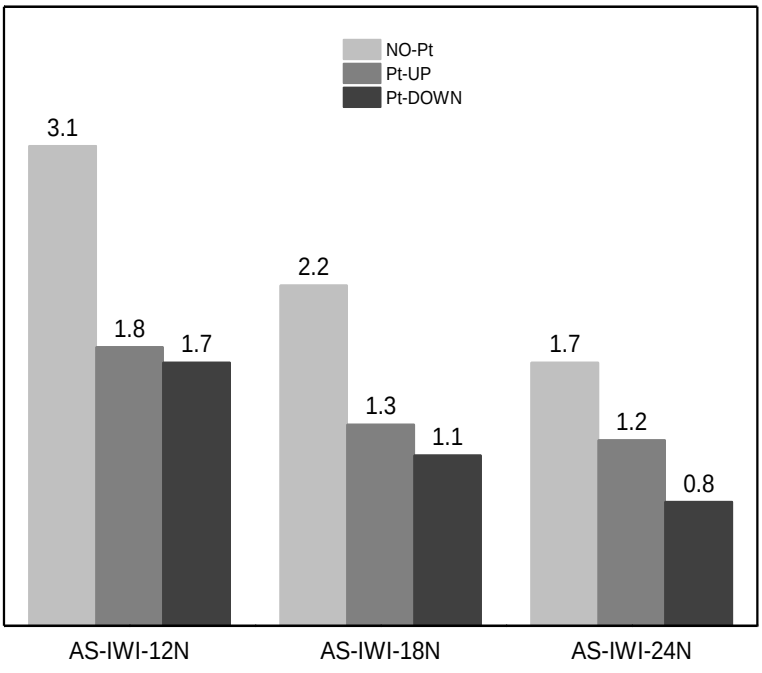

Figure 4.24: Olefins to paraffins ratio for C_3 fraction

Bibliography Chapter 4

[1] K. M. Cook, H. D. Perez, C. H. Bartholomew, and W. C. Hecker, "Effect of promoter deposition order on platinum-, ruthenium-, or rhenium-promoted cobalt Fischer-Tropsch catalysts," *Appl. Catal. A Gen.*, vol. 482, pp. 275–286, 2014.

[2] G. Jacobs, T. K. Das, Y. Zhang, J. Li, G. Racoillet, and B. H. Davis, "Fischer-Tropsch synthesis: Support, loading, and promoter effects on the reducibility of cobalt catalysts," *Appl. Catal. A Gen.*, vol. 233, no. 1–2, pp. 263–281, 2002.

[3] L. Fratalocchi, C. G. Visconti, L. Lietti, N. Fischer, and M. Claeys, "Tailoring the properties of a cobalt based Fischer Tropsch catalyst supported on stabilized γ-Al2O3 through the addition of diethylene glycol in the Co-impregnating solution," *Press*, 2016.

[4] D. Nabaho, J. W. Niemantsverdriet, M. Claeys, and E. Van Steen, "Hydrogen spillover in the Fischer-Tropsch synthesis: An analysis of platinum as a promoter for cobalt-alumina catalysts," *Catal. Today*, vol. 261, pp. 17–27, 2016.

[5] F. Diehl and A. Y. Khodakov, "Promotion of Cobalt Fischer-Tropsch Catalysts with Noble Metals: a Review," *Oil Gas Sci. Technol. …*, vol. 64, no. 1, pp. 11–24, 2009.

[6] B. Y. F. Morales and B. M. Weckhuysen, "Promotion Effects in Co-based Fischer – Tropsch Catalysis," *R. Soc. Chem.*, vol. 19, no. 1, pp. 1–40, 2006.

[7] S. Vada, A. Hoff, E. Ådnanes, D. Schanke, and A. Holmen, "Fischer-Tropsch synthesis on supported cobalt catalysts promoted by platinum and rhenium," *Top. Catal.*, vol. 2, no. 1–4, pp. 155–162, 1995.

[8] G. L. Bezemer, J. H. Bitter, H. P. C. E. Kuipers, H. Oosterbeek, J. E. Holewijn, X. Xu, F. Kapteijn, a J. Van Dillen, and K. P. De Jong, "Cobalt Particle Size Effects in the Fischer − Tropsch Reaction Studied with Carbon Nanofiber Supported Catalysts," *Am. Chem. Soc.*, vol. 128, no. 12, pp. 3956–3964, 2006.

[9] N. Fischer, E. Van Steen, and M. Claeys, "Structure sensitivity of the Fischer-Tropsch activity and selectivity on alumina supported cobalt catalysts," *J. Catal.*, vol. 299, no. March, pp. 67–80, 2013.

[10] W. Ma, G. Jacobs, R. A. Keogh, D. B. Bukur, and B. H. Davis, "Fischer-Tropsch synthesis: Effect of Pd, Pt, Re, and Ru noble metal promoters on the activity and selectivity of a 25%Co/Al2O3 catalyst," *Appl. Catal. A Gen.*, vol. 437–438, pp. 1–9, 2012.

[11] W. H. Lee and C. H. Bartholomew, "Multiple reaction states in CO hydrogenation on alumina-supported cobalt catalysts," *Journal of Catalysis*, vol. 120, no. 1. pp. 256–271, 1989.

[12] W. Ma, G. Jacobs, R. Keogh, C. H. Yen, J. L. S. Klettlinger, and B. H. Davis, "Fischer-Tropsch synthesis: Effect of Pt promoter on activity, selectivities to hydrocarbons and oxygenates, and kinetic parameters over 15%Co/Al2O3," *ACS Symp. Ser.*, vol. 1084, pp. 127–153, 2011.

Chapter 5 – Unconventional Co/Pt/γ-alumina Catalysts: Characterization, Performances and Validity of Low-Pressure Screening Tests

After a thorough analysis on the effects of Pt deposition order on Co-based catalysts prepared via conventional impregnation of cobalt nitrates, this chapter focuses on a novel preparation method, based on the addition of diethylene glycol (DEG) in the impregnating solution. Subsequently, the same analysis, carried out in Chapter 4, on the effect of platinum is applied on these novel catalysts.

Before entering into the details of the treatment, it is necessary provide the reader with a brief recap of the literature, presented more in detail in Chapter 2, dealing with cobalt particle size and precursors. The objective is to explain the reasons that have led us into the investigation of different catalyst preparation methods.

It is commonly accepted among researchers that nano-sized cobalt metal particles are the active species during FT synthesis [1] . High concentrations of such species on the catalyst surface are known to favor the FT reaction rate. Hence, smaller and well dispersed metal cobalt crystallites should display a higher activity per unit mass of catalytic active material [2]. To achieve these conditions, the active phase is usually supported on highly porous materials, like γ-Al_2O_3, which provide wide surface areas on which the active phase can be dispersed.

Conventional alumina supported Co-based catalysts are prepared via impregnation with a cobalt nitrate aqueous solution, followed by a low temperature drying and a high temperature calcination [3]. During the last step, Co nitrates are converted into Co_3O_4 species, which are then reduced to metallic cobalt during catalyst activation. This preparation method usually yields quite large cobalt crystallites (20 [nm]), which are not well dispersed on the support [4]. Moreover, it has been observed [5-6] that impregnation of γ-Al_2O_3 or SiO_2 with cobalt nitrate may generate cobalt clusters, i.e. regions with typical diameters of 100-400 [nm] with cobalt crystallites and regions without. All this results in a limited metallic surface and thus low activity per unit mass of catalyst.

It is acknowledged among scientists that FT synthesis becomes structure insensitive with crystallite sizes above 10 [nm]. On the other hand, when dealing with highly dispersed catalysts, a decrease in

the average cobalt particle size below 6 [nm] usually leads to an abrupt activity loss [7]. In order to decouple the possible link of strong support interaction to the activity loss, *Bezemer et al.* [8] studied the effect of Co^0 particle size by testing, both at atmospheric pressure and at 35 [bar], samples supported on a non-interacting substrate, made of carbon nanofibers. The authors observed in both cases a volcano-like curve for the *Cobalt Time Yield* (CTY) as a function of Co^0 crystallite size: maxima of the curves were around 6 [nm] and 8 [nm] at low and high pressure, respectively.

As discussed in Chapter 2, as *Bezemer et al.* [8] did, also many other authors investigated the effect of cobalt particle size on catalyst activity, at different conditions and with different supports. The general conclusion is that the optimal Co-based FT catalysts should have high Co-loading, around 20-30 wt. % and high Co dispersion, which corresponds to an average crystallite size in the range 6-10 [nm], depending on process conditions.

Several attempts have been made in finding a method to synthetize catalysts with both high dispersion and cobalt loading, not only in the FT research but also in other industrial processes, such as methanol synthesis [9] and hydrodesulphurization [10]. For all these reactions, highly dispersed materials have been prepared following the so-called *combustion synthesis method* [11]. It consists of adding an organic compound into the impregnation solution containing the precursor of the active phase. During calcination, an exothermic reaction occurs between metal salts, which act as oxidizer and the added organic compound, which acts as fuel in the oxidation process. The shift from a slow, endothermic decomposition of the cobalt nitrates alone to a fast, exothermic decomposition of the latter in the presence of the organic compound brings several advantages. In particular, the combustion phenomenon suppresses the agglomeration of Co_3O_4 species, thus delivering high metal dispersion on the catalyst surface [12] and high concentration of structural defects , which are beneficial for the catalyst activity.

As of today, the literature is scarce about these new preparation methods, and most of the papers refer to cobalt catalysts supported on SiO_2 ([4], [12], [13], [14], [15]), which, compared to γ-Al_2O_3, is a rather weakly interacting support.

In light of this, we decided to investigate how this innovative preparation method, applied on such a strongly interacting support as γ-Al_2O_3, affects both the properties and the performance of the FT cobalt catalyst. Subsequently, we studied the effect of platinum deposition order on this novel catalyst, both in terms of characterization and catalytic test. During the investigation, the results of the catalytic tests carried out at low pressure have been compared to the ones obtained by our research group at industrially relevant conditions, on the high pressure Fischer-Tropsch rig: those

results are reported in previous Master theses [16-17] as well as in a journal article [18], currently submitted.

5.1 Catalyst preparation

Three different batches of catalyst have been prepared to perform the investigation at issue. All the catalysts are supported on stabilized γ-Al_2O_3 (see Chapter 4). The amount of DEG is reported as *0.5GL* in the catalyst nomenclature: it corresponds to the *cobalt nitrate-to-DEG* molar ratio in the impregnating solution. The Co and Pt loads are 24 wt.% and 0.1 wt.% respectively.

5.1.1 AS-IWI-24N-0.5GL

As the Co-loading of the stabilized γ-Al_2O_3 (AS) is about 5.7 wt.%, the remaining cobalt is deposited in four identical impregnation steps, with an aqueous solution of cobalt nitrate ($Co(NO_3)_2 \cdot 6H_2O$, *Sigma Aldrich*, ≥ 98.0%) and diethylene glycol (DEG, *Sigma Aldrich*, ≥ 99.0%), in a molar ratio of 0.5. Each impregnation step is followed by drying in static air at 120 [°C] for 2 [h], and calcination in static air at 400 [°C] for 4 [h] (heating rate: 2 [°C/min]).

5.1.2 AS-IWI-24N-0.5GL-0.1PtUP

In the *UP* configuration, the promoter deposition occurs once the unpromoted sample is prepared. After the four impregnation steps of cobalt nitrate with DEG on the stabilized γ-Al_2O_3, an additional step follows: the aqueous solution of platinum salts ($Pt(NH_3)_2(NO_2)_2$, *Sigma Aldrich*) is impregnated on the catalyst, which then undergoes drying in static air at 120 [°C] for 2 [h] and calcination in static air at 500 [°C] for 5 [h]. The nomenclature UP stands for a sequential deposition of the noble metal promoter (Pt) which occurs after all the cobalt impregnation steps.

5.1.3 AS-IWI-24N-0.5GL-0.1PtDOWN

In the *DOWN* configuration, the deposition of 0.1 wt.% platinum is made directly on the stabilized support: after impregnation, drying in static air at 120 [°C] for 2 [h] and calcination at 500 [°C] for 5 [h] follow. The deposition of 24 wt.% cobalt occurs afterwards, according to the same method described for the unpromoted sample. The nomenclature DOWN stands for a deposition of the promoter "underneath" the active cobalt.

5.2 Effect of DEG addition in the impregnating solution

The first part of our study deals with the effect on catalyst properties and performances when adding DEG to the impregnating solution. The comparison basis is the unpromoted catalyst prepared by simple impregnation of cobalt nitrates, i.e. the AS-IWI-24N (see Chapter 4).
The two catalysts, AS-IWI-24N and AS-IWI-24N-0.5GL, are identical to the catalysts Co/Al_2O_3(s) and Co-DEG/Al2O3(s) respectively, reported by *Fratalocchi et al.* [18] in their novel paper.
Briefly, we named the first sample as "conventional catalyst" and the second as "DEG-catalyst".

5.2.1 Catalyst characterization

The different characterization analyses employed to identify the morphological and structural features of the synthetized catalysts are the following:

- Thermogravimetric analyses (*TG/DTA*), used to study the phenomena occurring during the calcination step in presence of DEG;
- ICP-MS (*Inductively Coupled Plasma Mass Spectrometry*), used to identify and quantify the various species present on the catalyst surface;
- BET (*Brauner-Emmet-Teller*), used to determine the surface area, the pore volume and the pore diameter;

- Ex-situ XRD (*X-Ray Diffraction*), used to identify the average Co_3O_4 crystallite diameter after calcination;
- TPR (*Temperature programmed reduction*), used to determine the temperature of the reduction peaks linked to different cobalt phases present on the catalyst

The second calcination step of the AS-IWI-24N-0.5GL catalyst was initially monitored by the TG/DTA instrument, in order to make sure that the expected combustion reaction actually occurred. Figure 5.1 shows the results obtained:

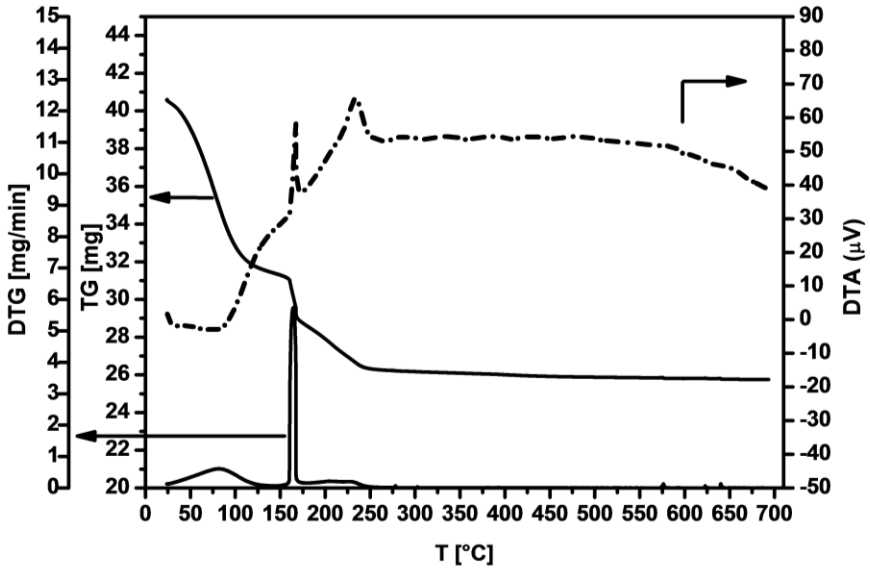

Figure 5.1: AS-IWI-24N-0.5GL: TG/DTA and DTG profiles [18]

The DTA curve displays some inflections in the temperature range 25 ÷ 120 [°C], matched with a quite significant weight loss: the occurring phenomenon is ascribed to the endothermic loss of water. At higher temperatures, the two intense peaks appear in the range 150 ÷ 260 [°C], which indicate the presence of exothermic reactions, also matched with a weight loss of about 35%. These reactions are most likely to correspond to the combustion process between cobalt nitrates and DEG, which act as oxidizer and fuel respectively. A less pronounced 2% weight loss, which occurs in the wider temperature range 260 ÷ 700°C, is probably due to the combustion of residual DEG in air.
Therefore, Figure 5.1 is clear evidence that in the presence of DEG, the decomposition of cobalt nitrates, which is typically endothermic [19], becomes an exothermic process.

The results of BET and ICP-MS analyses for the two catalysts are reported below:

Table 5.1: Textural properties of the calcined catalyst (a= BET analysis; b= ICP-MS analysis) [18]

	Surface area[a] [m^2/g]	Pore volume[a] [cm^3/g]	Nominal Co wt.%	Actual Co[b] wt.%
AS-IWI-24N	84.4	0.22	23.00	21.27 ± 0.35
AS-IWI-24N-0.5GL	87.5	0.21	23.00	23.15 ± 0.42

The surface area of the sample prepared with DEG is slightly higher than that of the conventional sample; in contrast, the pore volume remains substantially the same. The nominal cobalt loading of the two catalysts, which includes the 5.7 wt.% cobalt impregnated to stabilize the support, is in good agreement with the values obtained by the ICP-MS experiments. Such results may indicate that no loss of active phase has occurred during the exothermic calcination of the sample prepared with DEG.

The XRD spectra and the crystallite diameters obtained via Rietveld refinement of the spectra are shown in Figure 5.2 and Table 5.2 respectively.

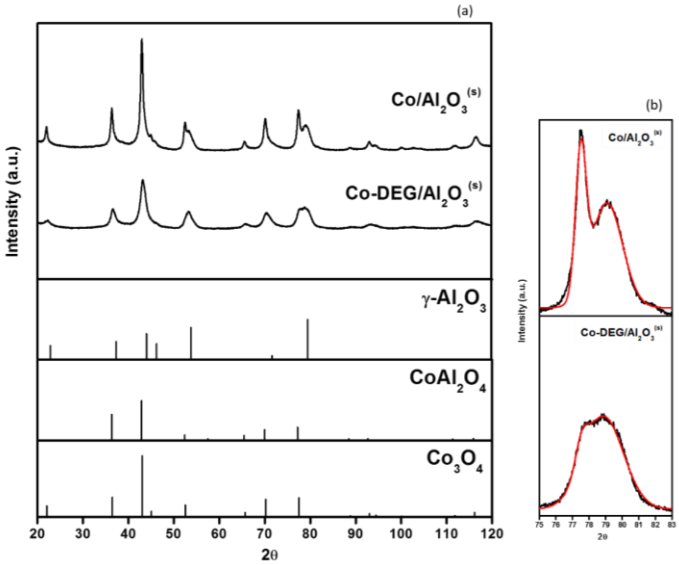

Figure 5.2: (a) XRD patterns of the calcined Co/Al_2O_3(s) and Co-DEG/Al_2O_3(s) catalysts. Reference patterns of γ-Al_2O_3, $CoAl_2O_4$ and Co_3O_4 phases are also shown. (b) Details of the XRD patterns of Co/Al_2O_3(s) (top) and Co-DEG/Al_2O_3(s) (bottom) catalysts [18]

Table 5.2: Co phases detected on the calcined catalysts analyzed via XRD and average crystallite size obtained via Rietveld refinement of the corresponding XRD spectra [18]

	After calcination				
	γ-Al_2O_3 [%]	Co_3O_4 [%]	$CoAl_2O_4$ [%]	dCo_3O_4 [nm]	$dCoAl_2O_4$ [nm]
Co/Al_2O_3(s)	62.2	25.5	12.3	21	4
Co-DEG/Al_2O_3(s)	62.6	26.0	11.4	11	2

The crystalline phases detected are Co_3O_4, $CoAl_2O_4$ and γ-Al_2O_3. No peaks of different cobalt phases, like $Co(OH)_2$ or CoO, could be identified. Although the catalysts were prepared from the same batch of alumina, the average crystallite size of the cobalt-alumina complex for the conventional catalyst (4 [nm]) is slightly higher than that of the DEG-catalyst (2 [nm]). This suggests that the combustion phenomena occurring during calcination may affect the rearrangement of the $CoAl_2O_4$ particles on the support surface. Different average Co_3O_4 crystallite size have been also obtained, 21 [nm] in the conventional catalyst and 11 [nm] in the DEG-catalyst respectively. As it is evident from Figure 5.2, the larger Co_3O_4 crystallites of the conventional catalyst results in thinner and more intense peaks; on the other hand, the DEG-catalyst shows broader and less intense peaks, which correspond to the small Co_3O_4 crystallites. This is particularly evident in the 2θ range of 75 ÷ 83°, where the Co_3O_4 distinctive peak (2θ = 77.5°) is close to that representing the γ-Al_2O_3 phase (2θ = 79.4°). While for the DEG-catalyst the two peaks tend to overlap, in the conventional catalyst the sharper Co_3O_4 peak permits discrimination.

In Table 5.3, additional in-situ XRD (available at the *University of Cape Town* (UCT)) analyses performed [18] after catalyst reduction provide additional information on average cobalt dimensions for the intermediate oxide (CoO) and the metallic phase (Co^0).

Table 5.3: Average crystallite size obtained via Rietveld refinement of the corresponding XRD spectra [18]

	After reduction		
	dCoO [nm]	dCo^0 [nm]	$dCoAl_2O_4$ [nm]
Co/Al_2O_3(s)	6	14	7
Co-DEG/Al_2O_3(s)	4	7	7

Also in the reduced form, the cobalt particle size is lower for the DEG-catalyst, corroborating the beneficial effect of glycol addition on catalyst dispersion.

After the investigation of the morphological features, TPR analyses have been performed to investigate the reducibility of the two catalysts. The analyses were carried out in-situ on the low pressure lab scale rig (see details in Chapter 3), employed also for the catalytic tests. The result for the calcined conventional catalyst is displayed in Figure 5.3:

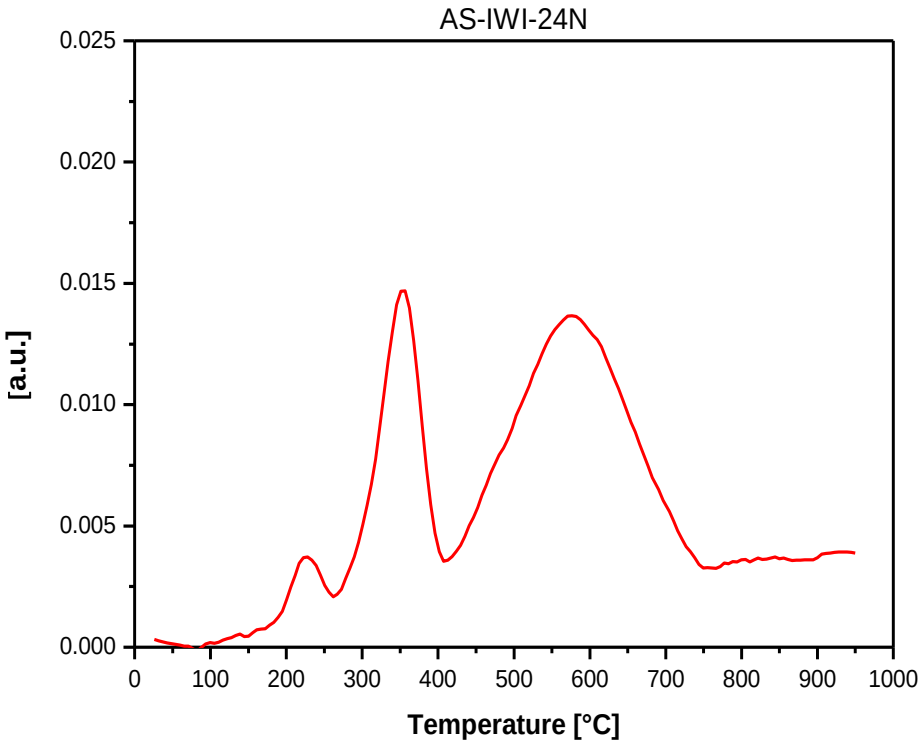

Figure 5.3: TPR profile of the conventional catalyst

The TPR profile shows three distinctive H_2-consumption peaks. The first one at low temperatures (230 [°C]) is ascribed to the reductive decomposition of residual cobalt nitrates on the catalyst surface, in agreement with the literature [2,17] and our previous analyses (see Chapter 4). The second peak at 350 [°C] is regarded as the first reduction step from Co_3O_4 to CoO, while the peak corresponding to the second reduction step from CoO to Co^0, the cobalt metallic phase active in FTS, is at higher temperatures, 575 [°C]. After the third peak the profile seems to rise again but does not close at 950 [°C], that is the final temperature of the experiment. However, leaving the system at the final temperature under the same gas flow, we could see the closure of a fourth peak.

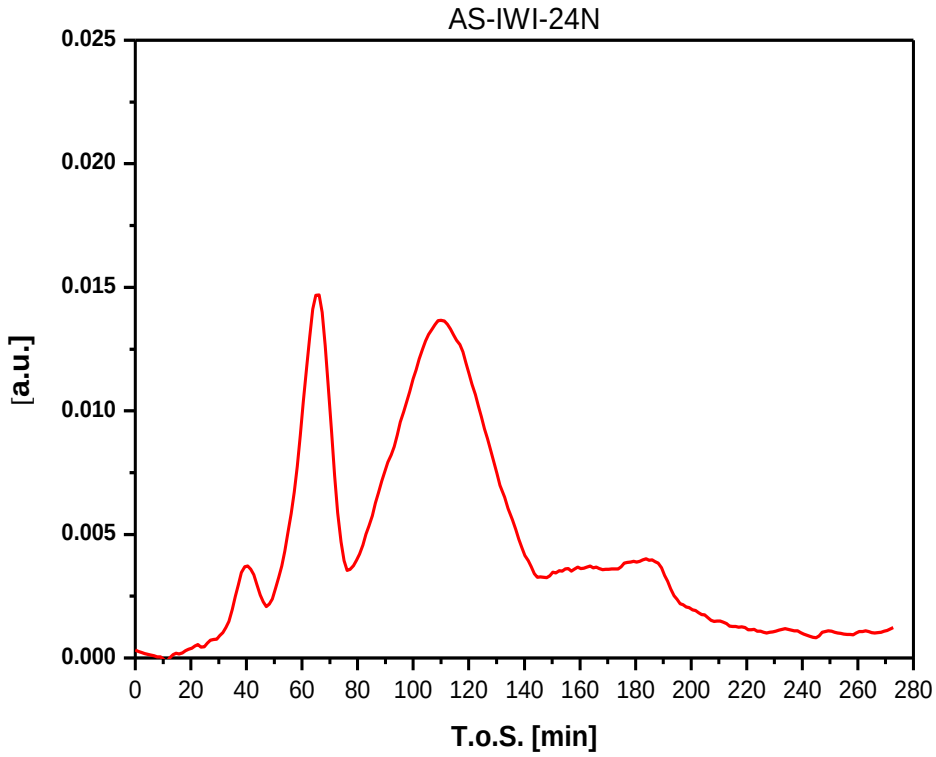

Figure 5.4: H_2 consumption as a function of the T.o.S. (*Time on Stream*) for the conventional catalyst

According to the literature [3], this last broad peak is associated with the reduction of the cobalt species in close interaction with the support, whose formation is not totally clear. In particular, this peak may be associated either to the reduction of the cobalt-alumina complexes which stabilize the support or to the reduction of the cobalt-alumina mixed spinels formed at high temperatures during the TPR analysis [21].

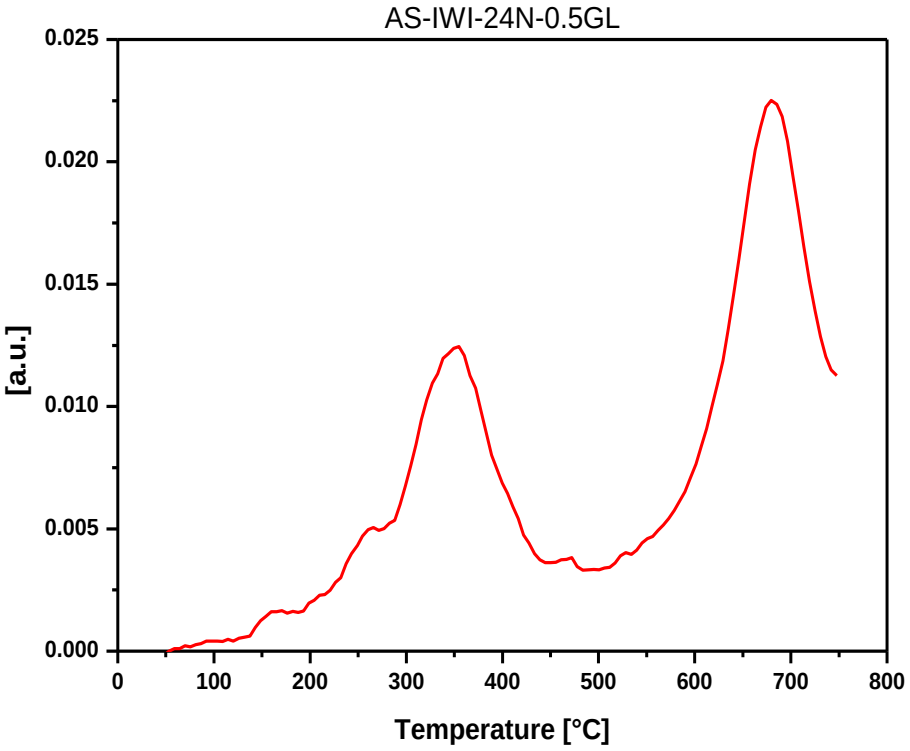

Figure 5.5: TPR profile of the DEG-catalyst

Contrary to the conventional catalyst, the TPR profile of the DEG-catalyst (Figure 5.5) shows a lower number of peaks. In particular, the peaks referred to the reduction of the residual cobalt nitrates is merged with the first reduction step of the Co_3O_4, resulting in a first wider peak, whose maximum is at 352 [°C]; the maximum for the second reduction step occurs at 679 [°C].

In comparison with the conventional catalyst, the first reduction step occurs at almost the same temperature (352 vs 350 [°C]) while the second one occurs at significantly higher temperatures (679 vs 577 [°C]). This suggests that the DEG-catalyst is significantly harder to reduce than the conventional one. In fact, according to *Nabaho et al.* [21], the most crucial step during catalyst activation is the reduction of the CoO species, which suffer strong interactions with the support; so, the more difficult reducibility of a catalyst is associated with higher reduction temperatures of the $CoO \rightarrow Co^0$ step. The lower reducibility of the DEG-catalyst, compared to that of the conventional catalyst, can be ascribed to the difference in particle size (Figure 5.6): the smaller the cobalt particles, the stronger the cobalt-support interactions and the lower the reducibility. Therefore, from these TPR results we can confirm that the combustion process occurring during calcination for the

DEG-catalyst has led beneficial effects, in terms of cobalt dispersion (limited Co_3O_4 agglomeration), but also unfavorable ones, as small crystallites are significantly difficult to be reduced.

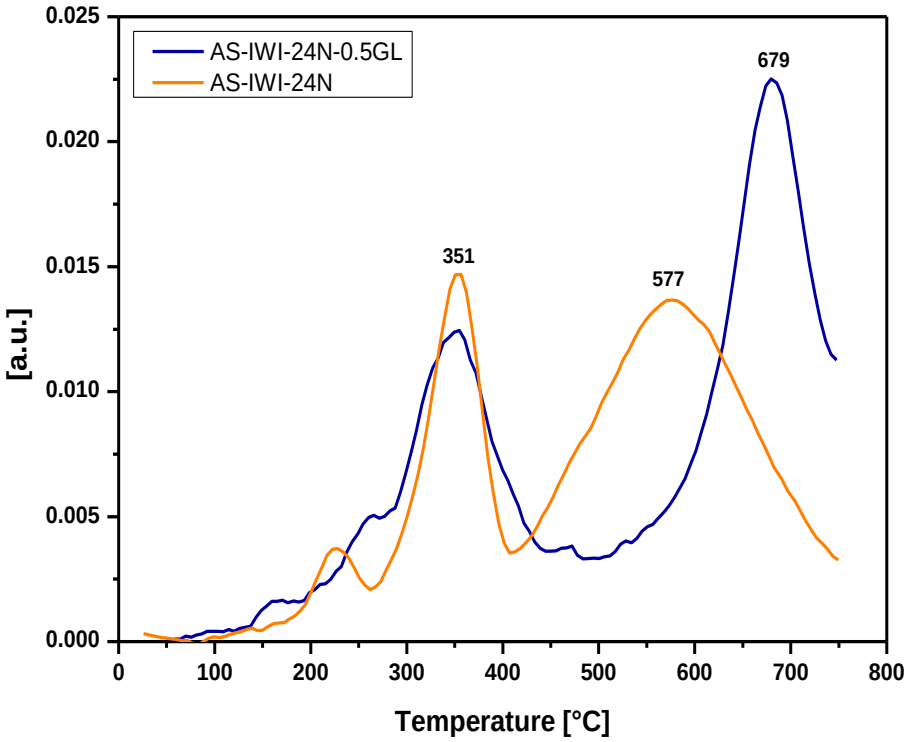

Figure 5.6: Comparison of TPR profiles for the conventional and the DEG-catalyst

5.2.2 Catalytic tests at ambient pressure

In order to gain insight into the relationship between reducibility and activity, catalytic tests on the two catalysts have been performed on the lab scale rig operating at ambient pressure. Briefly, the catalytic test consists of two main stages: catalyst activation, lasting 13.5 [h] at 400 [°C] under a flow of pure H_2 (50 [Ncc/min]), and reaction, at 240 [°C], flowing syngas (42.5 [Ncc/min], $H_2/CO \approx 2$) diluted in pure N_2 (7.46 [Ncc/min]). Downstream of the reactor, the reaction products are analysed in a gas chromatograph (see details in Chapter 3). The standard operating conditions are reported in Table 5.4.

Table 5.4: Standard operating conditions of a low pressure catalyst test

Standard conditions	
T [°C]	240
P [atm]	1
$GHSV_{syn}$ [$Ncc/g_{cat}/h$]	5104
H_2/CO [mol/mol]	2.05

Figure 5.7 compares the performances between the conventional and the DEG-catalyst in terms of CO conversion, methane selectivity and selectivity towards CO_2.

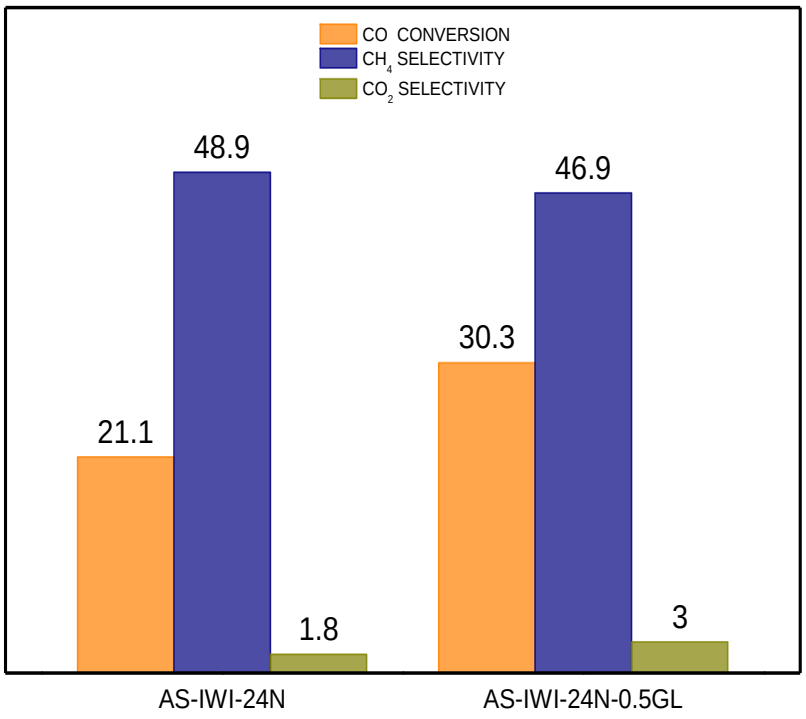

Figure 5.7: Comparison of performances for the conventional and the DEG-catalyst

The DEG-catalyst shows a higher activity than that of the conventional catalyst. This is in contrast with the TPR profiles, where the conventional catalyst showed a better reducibility. Apparently, even though the DEG-catalyst is hardly reducible, its higher dispersion seems to favor the activity,

as shown by the higher CO conversion. Therefore, in this case the good dispersion appears to overcome the limited reducibility, leading to a more active catalyst.

Methane selectivity is very similar between the two samples. This result is in agreement with *Bezemer et al.* [8], who investigated methane selectivity as a function of the particle size and found a structure insensitivity for diameters higher than 5 [nm].

Conversely, CO_2 selectivity is higher for the DEG-catalyst. Higher CO_2 selectivity is the result of a greater WGS (*Water Gas Shift*) activity, which is a side-reaction in the FT kinetic mechanism. Given the greater activity of the DEG-catalyst, the amount of water produced is higher and thus the WGS is more favored.

We can state, in conclusion, that the addition of an organic compound, namely DEG, in the impregnating solution has limited Co_3O_4 agglomeration, which usually occurs in conventional catalysts. This leads to a well-dispersed catalyst. Yet, at the expense of a high dispersion, a low reducibility has followed as small cobalt crystallites suffered the strong interactions with the γ-Al_2O_3 support. Nevertheless, in terms of activity, the high dispersion has prevailed on the limited reducibility, finally leaving a more active catalyst. Therefore, it has been confirmed, even with strongly interacting supports as γ-Al_2O_3, the "combustion synthesis method" represents an efficient tool for the synthesis of highly active FT catalysts.

5.3 Effect of Pt deposition order in DEG-catalysts

The experiments described in the previous paragraph confirmed that even with strongly interacting supports as γ-Al_2O_3, the "combustion synthesis method" represents an efficient tool for the synthesis of highly active FT catalysts. However, the limited reducibility achieved is a major drawback of this method of preparation. It is acknowledged that catalysts with small Co_3O_4 crystallites are more difficult to reduce [22]. For conventional catalysts, i.e. samples prepared by impregnating γ-Al_2O_3 with an aqueous solution of cobalt nitrate salts, *Zsoldos et al.* [23] reported an improved reducibility when Co was combined with small amounts of Pt. The same authors observed, and it was confirmed in more recent studies [2-17], that Pt addition enhances the reducibility of the small cobalt crystallites which suffered strong interactions with the support, leaving a higher concentration of Co^0 particles on the catalyst surface.

Consequently, we investigated the effect of Pt addition on the catalysts prepared via the "combustion synthesis method", with the objective of coupling high reducibility with high dispersion for an even more active catalyst. In particular, we studied the effect of Pt deposition order on morphological features, reducibility and activity of the DEG-catalyst.

Three catalysts have been prepared: AS-IWI-24N-0.5GL, AS-IWI-24N-0.5GL-0.1PtUP and AS-IWI-24N-0.5GL-0.1PtDOWN. Details on the preparation are reported above in this Chapter. Synthetically, we named the three catalysts as *NoPt* (i.e. the unpromoted DEG-catalyst), *PtUP* and *PtDOWN* catalyst, respectively.

5.3.1 Catalyst characterization

In-situ XRD analyses were carried out on the three catalysts, both in calcined and reduced form. The crystallite diameters for the Co3O4 and Co0 phase are reported in Table 5.5:

Table 5.5: Average crystallite size obtained via Rietveld refinement of the corresponding XRD spectra: (a) calcined catalyst, (b) reduced catalyst

	dCo_3O_4 (a) [nm]	**dCo^0 (b) [nm]**
AS-IWI-24N-0.5GL	10.2	9
AS-IWI-24N-0.5GL-0.1PtUP	10.3	6.4
AS-IWI-24N-0.5GL-0.1PtDOWN	9	5.4

While on calcined catalysts there is no direct influence of platinum on the crystallite diameter, after reduction the average Co^0 particle size for the Pt-promoted catalysts is significantly smaller than that of the unpromoted. Apparently, platinum's capability of reducing small and dispersed Co_3O_4 particles has shifted the particle size distribution towards smaller values, thus resulting in a lower average Co^0 particle size.

For what concerns catalyst reducibility, the result of the TPR analyses carried out for the three calcined catalysts are reported in Figure 5.8.

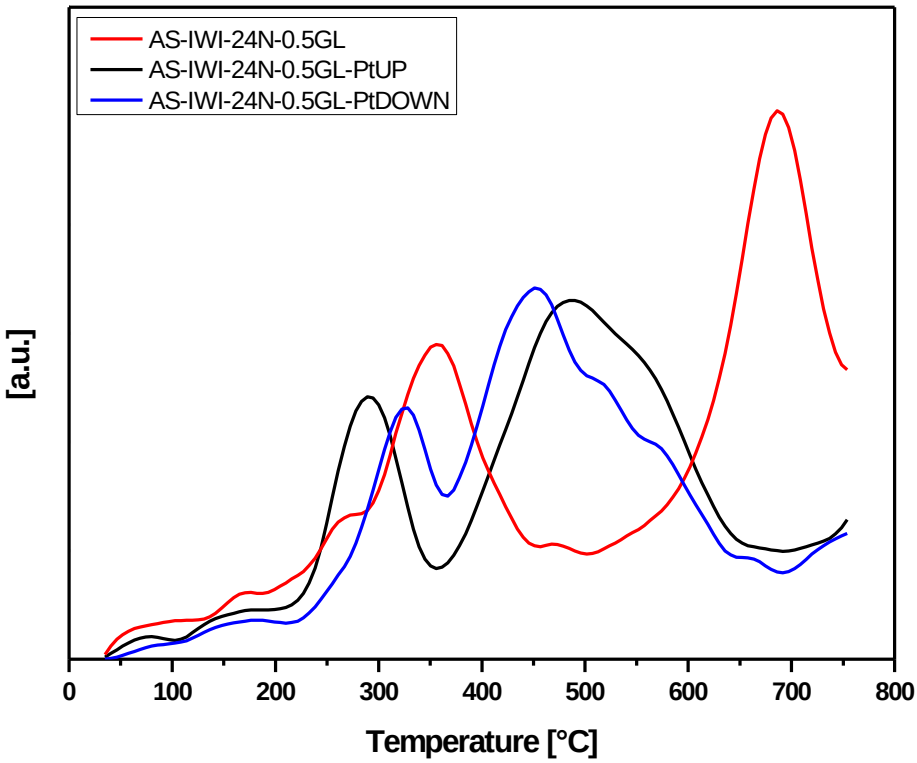

Figure 5.8: Effect of Pt deposition order in the TPR profiles

For both the promoted catalysts, the reduction peaks are shifted towards lower temperatures, compared to those of the unpromoted; the Pt promotion on catalyst reducibility is recognised in the literature [24].

Comparing the different Pt deposition orders, the *PtUP* catalyst shows a lower temperature for the first reduction step, from Co_3O_4 to CoO, compared to that of the *PtDOWN* catalyst (305 vs 325 [°C]). This behavior, observed also in the catalysts described in Chapter 4, was ascribed to the fact the Pt, deposited at the last step, would be more easily reached from H_2 thus favoring the transition $Co_3O_4 \rightarrow CoO$.

The most beneficial effect of Pt promotion is correlated to the second reduction step, from CoO to Co^0, which is delayed in the unpromoted catalyst due to the strong interactions between CoO species and the support; while the peak of the unpromoted is observed at 685 [°C], *PtUP* and *PtDOWN* catalysts shows anticipated peaks at 460 and 455 [°C], respectively. The slightly anticipated peak of the *PtDOWN* catalyst, with respect to that of the *PtUP* catalyst, may be ascribed to the enhanced H_2 spillover mechanism, activated by the Pt atoms bonded with the support and

probably present in a greater number in the *Pt-DOWN* configuration. However, with such small Co_3O_4 crystallites as detected in the XRD measurements, it is unlikely to think of a creation of a cobalt layer on the catalyst surface, over which would be deposited all the platinum, in the *PtUP* configuration. It appears more reasonable that also in the latter configuration some platinum would deposit on the support, triggering the H_2 spillover mechanism which is responsible of the enhanced reducibility [21]. As a consequence, the difference in temperature of the second reduction step is not very significant between the two deposition orders.

5.3.2 Catalyst testing at ambient pressure

The three samples have been tested in the lab scale rig operating at ambient pressure. The standard operating conditions used during the experiments are reported in Table 5.4.

Figure 5.9 shows the activity and selectivity results at standard conditions. The advantage of Pt addition in terms of catalyst activity is substantial. In particular, when depositing platinum after the last impregnation step of the cobalt, i.e. in the *PtUP* configuration, a 22.7% activity increase is observed; when depositing platinum directly on the support (*PtDOWN*), the activity increases by 29%. These results are in agreement with the TPR analyses, which showed better reducibilities for the promoted samples, when compared to that of the unpromoted: the lowest reduction temperatures for the $CoO \rightarrow Co^0$ step is coupled with the highest activity for the *PtDOWN* catalyst. Also, the Co^0 crystallite size for the Pt-promoted catalysts (Table 5.5) is very close to the optimal dimension of 6 [nm] found by *Bezemer et al.* [8] in the atmospheric tests: this aspect is also reflected in a higher activity for the Pt-promoted DEG-catalysts.

The results obtained confirm the effectiveness of platinum promotion even on well-dispersed systems, like the DEG-catalyst. The increased activity observed for the *PtUP* configuration suggests that the high dispersion still allows an efficient deposition of the promoter.

All the three catalysts display high methane selectivities, confirming both the significant influence of methanation reaction and the low chain growth probability (α) at the investigated conditions of high temperature and atmospheric pressure.

CO_2 selectivity is fairly in agreement with the catalyst activity results: the promoted samples that are more active than the unpromoted also show an increase in WGS activity by 60% and 53% respectively.

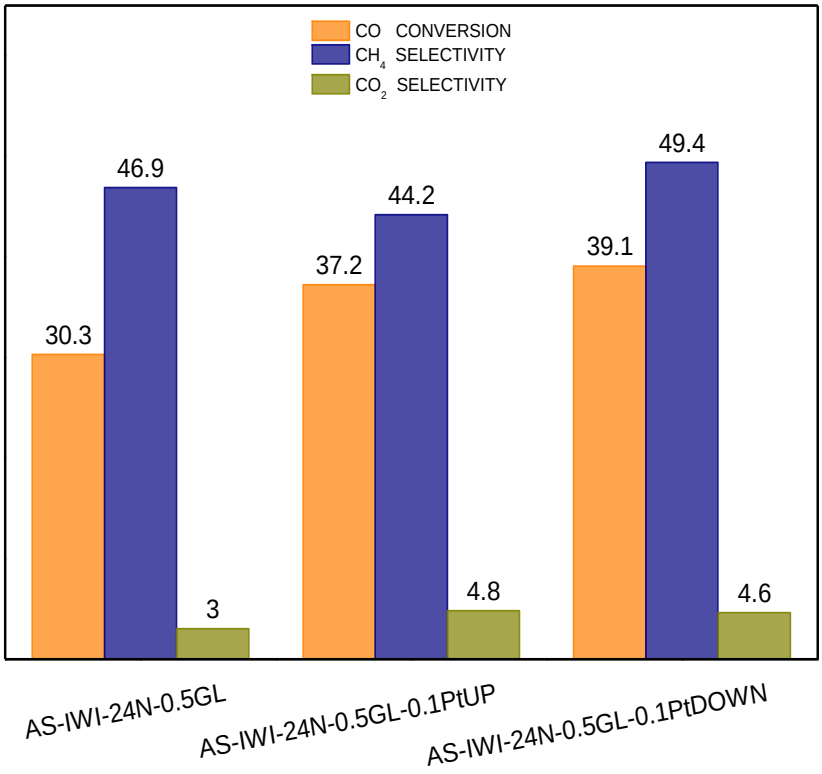

Figure 5.9: Catalyst performances at standard conditions

5.3.2.1 Effect of process variables

Throughout the catalytic testing, the three catalysts have been tested also at different operating conditions from the standard ones. Especially, three temperatures, two syngas ratios and three GHSV (*Gas Hourly Space Velocity*) have been investigated. The experiments at different conditions were carried out by changing one variable at a time and always returning to standard conditions before changing the next variable; this was made to prevent alterations of the results owing to catalyst deactivation. The different operating conditions are reported in Table 5.6.

Table 5.6: Investigated process variables

Temperature	H2/CO inlet ratio	GHSV
240	2.05	5104
230	2.50	6500
220	\	7500

Temperature

Temperature effect on the three catalyst is reported in Table 5.7. For each catalyst the observed trend respects the ones found at industrially relevant FT conditions. Being the FT reaction free of equilibrium limitations, the kinetics play a major role: decreasing the temperature, the kinetic constant decreases and so does the reaction rate.

As said above, CO_2 selectivity is strictly related to the CO conversion: hence, at lower temperature also the CO_2 yield is smaller. Also, at industrially relevant FT conditions, lower temperatures increase the chain growth probability (see Chapter 1), favoring the formation of heavier products. At ambient pressure, however, the product distribution is narrower as it lays in the range $C_1 \div C_6$; nevertheless, the same trend is still observed.

At higher temperatures the system is more hydrogenating and methane selectivity increases.

Table 5.7: Temperature effect on catalyst performances

Catalyst	T [°C]	CO Conversion [%]	CH_4 Selectivity [%]	CO_2 Selectivity [%]
AS-IWI-24N-0.5GL	220	15,4	29,2	1,3
	230	22,3	37,0	1,8
	240	30,3	46,9	3,0
AS-IWI-24N-0.5GL-0.1PtUP	220	19,1	27,3	1,8
	230	27,3	35,0	2,8
	240	37,2	44,2	4,8
AS-IWI-24N-0.5GL-0.1PtDOWN	220	20,1	28,0	1,4
	230	28,4	37,4	2,4
	240	39,1	49,4	4,6

H_2/CO inlet ratio

The effects of the different syngas ratio are displayed in Table 5.8. Increasing the H_2 concentration in the feed over the stoichiometric value needed for the FT reaction, the limiting reactant becomes CO and thus its conversion increases. Moreover, the system becomes more hydrogenating and the H_2/CO ratio approaches that required for the methanation reaction ($H_2/CO = 3$): as a result, methane selectivity increases and the product distribution shifts towards lighter products. For what concerns the WGS activity, molecular hydrogen is a product of the reaction so its higher concentration shifts the equilibrium towards the reactants; consequently, at higher H_2/CO inlet ratios, the selectivity to CO_2 decreases, even though CO conversion increases.

The results obtained well represent the behaviors described above; *PtDOWN* appears as the most hydrogenating catalyst, with a 55.9% methane selectivity at a syngas ratio of 2.5. The unpromoted and the *PtUP* catalysts follow with 51.9% and 50.2%, respectively.

Table 5.8: Effect of the syngas ratio on catalyst performances

Day	Catalyst	T [°C]	CO Conversion [%]	CH_4 Selectivity [%]	CO_2 Selectivity [%]
2	AS-IWI-24N-0.5GL-70	2,05	26,4	46,5	2,6
		2,50	28,7	51,9	2,3
1	AS-IWI-24N-0.5GL-0.1PtUP-71	2,05	36,3	44,3	4,3
		2,50	39,7	50,2	4,0
1	AS-IWI-24N-0.5GL-0.1PtDOWN-73	2,05	38,2	49,3	4,5
		2,50	42,5	55,9	4,1

GHSV (Gas Hourly Space Velocity)

The effects of the different residence times are reported in Table 5.9. At the GHSV increases, the residence time in the reactor decreases: consequently, CO conversion decreases. As an example, for the unpromoted catalyst, increasing the GHSV from 5104 to 7500 [$Ncc/g_{cat}/h$] the CO conversion decreases by 30.5%. On the other hand, methane selectivity remains rather constant changing the residence time in the reactor. As the H_2/CO ratio is kept at standard conditions, CO_2 selectivity shows the same trend as that of the CO conversion.

Table 5.9: GHSV effect on catalyst performances

Day	Catalyst	GHSV [Ncc/g_{cat}/h]	CO Conversion [%]	CH_4 Selectivity [%]	CO_2 Selectivity [%]
1	AS-IWI-24N-0.5GL-70	5104	29,5	47,8	2,8
		6500	23,5	47,7	2,3
		7500	20,5	48,1	2,1
2	AS-IWI-24N-0.5GL-0.1PtDOWN-73	5104	34,6	47,4	4,2
		6500	28,3	47,6	3,4
		7500	25,3	47,0	2,9
2	AS-IWI-24N-0.5GL-0.1PtUP-71	5104	32,1	43,6	4,4
		6500	26,5	44,0	3,6
		7500	22,5	44,7	3,2

5.4 Comparison of performances at low pressure (LP) and high pressure (HP)

5.4.1 Advantages of low pressure operations

The principal objective of CO hydrogenation studies run at low pressure in the LCCP (*Laboratory of Catalysis and Catalytic Processes*) laboratories, it the screening of highly active Co-based catalysts for Fischer-Tropsch synthesis. Part of this thesis work is, therefore, dedicated to verifying the compatibility of the results obtained at low pressures with those obtained at high pressure. The need of developing the LP (*Low Pressure*) rig, in parallel with the already existing facility operated at industrially relevant FTS conditions (P = 25 [bar]), originates principally from the necessity of simplifying and accelerating the test procedure of the catalysts studied.

The HP (*High Pressure*) rig is more burdensome, in all aspects, than the corresponding LP rig. Furthermore, a stricter approach must be taken during operations as the much severer conditions of the system make it sensitive to small alterations of the operative variables. Also, for what concerns catalyst use and gas flows, the HP rig is more demanding: the catalytic bed consists of 2 [g] of catalyst diluted in 8 [g] of α- Al_2O_3 and reactant flows of about 10 [Nl/h] are employed. The reactor

and the product collection tanks are made of high pressure resistant INOX steel. Moreover, the safety system installed for monitoring and regulating the process variables is more complex and expensive than that installed on the BP rig.

The major problem associated to the HP rig lays in the operating times needed to perform the experiments. The leak test itself lasts 24 [h] and is carried out in an inert environment at 5 [bar] more, at least, than the operating pressure during reaction. After the leak test follows catalyst activation in pure H_2, at 400 [°C] for 17 [h]. Overall, this operation requires 25 [h] because the system is slowly brought to 400 [°C], with a first ramp from ambient temperature to 300 [°C] (2 [°C/min]), flowing H_2 diluted in N_2, followed by a second from 300 [°C] to the reduction temperature (2 [°C/min]), halving the N_2 sent during the first ramp. Once the system is at 400 [°C], N_2 flow is gradually lowered to zero. After catalyst activation, the temperature is reduced to 180 [°C] in 3 [h] and the H_2 feed is slowly substituted with highly diluted syngas (syngas/N_2).

Subsequently follows plant pressurization, a very delicate phase because the pressure has to be slowly increased, being careful to avoid stagnation zones into the reactor; the whole operation takes 6 [h].

Once the reaction pressure is reached, the system has to be brought to the reaction temperature (T = 200 ÷ 240 [°C]). Aiming to avoid sudden changes in temperature, the heating is done with a slow ramp (0.03 [°C/min]) from 180 [°C] to the reaction temperature. The diluted syngas stream is gradually concentrated by reducing N_2 flow in 7 [h]. Once the reaction conditions are reached, it takes from 48 to 72 [h] to the system to reach stationary conditions.

The low pressure rig, on the other hand, allows to obtain valid results within 24 [h], from the reactor loading to the rig shut down (see Chapter 3). Stationary conditions are usually reached within 1 [h] and the light species produced allow fast gas analyses, with experimental results every 4 [min], generating dense conversion and selectivity profiles as a function of the *Time on Stream* (T.o.S.). Hence, time lapses needed to test a catalyst are very short. This allows fast screening of a large number of samples at the same time in which a single catalyst would be tested on the HP rig. In fact, for a first estimate of the activity of a new catalyst, it is sufficient to compare the results obtained on the LP rig with the ones of a reference sample tested at the same conditions.

In principle, if a new sample passes the screening test at low pressure, showing promising results, it is then thoroughly studied on the HP rig: in this way, time and resources are saved for time-consuming tests at HP on poorly active catalyst.

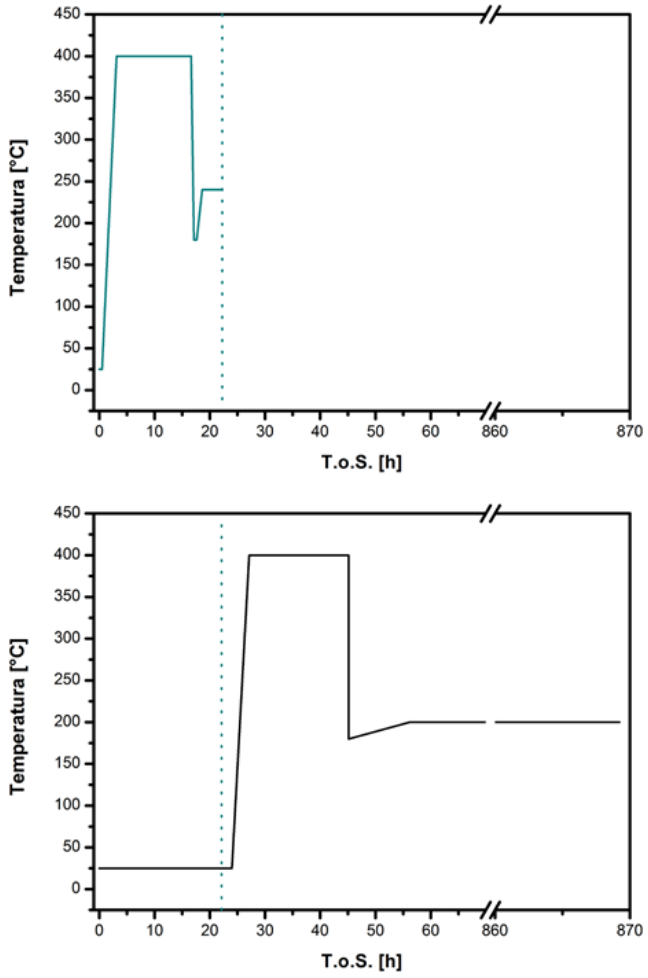

Figure 5.10: Temperature profiles for the LP (top) and HP (bottom) processes, from start to shutdown of the rigs

5.4.2 Validity of the Low Pressure (LP) tests

Previous studies [17] performed in the LCCP laboratories validated the activity results of the LP tests against the data collected on the HP rig. The effect of Pt deposition order on conventional Co-based catalysts, prepared via impregnation of stabilized alumina with a solution of cobalt nitrate salts, was studied both at LP and at HP; a good correlation in terms of catalyst activity was found between the experimental data obtained on the two rigs (Figure 5.1). In particular, the relative trend between the three catalysts is respected not only in qualitative, but also in quantitative terms: the CO conversion values appear close between LP and HP for the same catalyst.

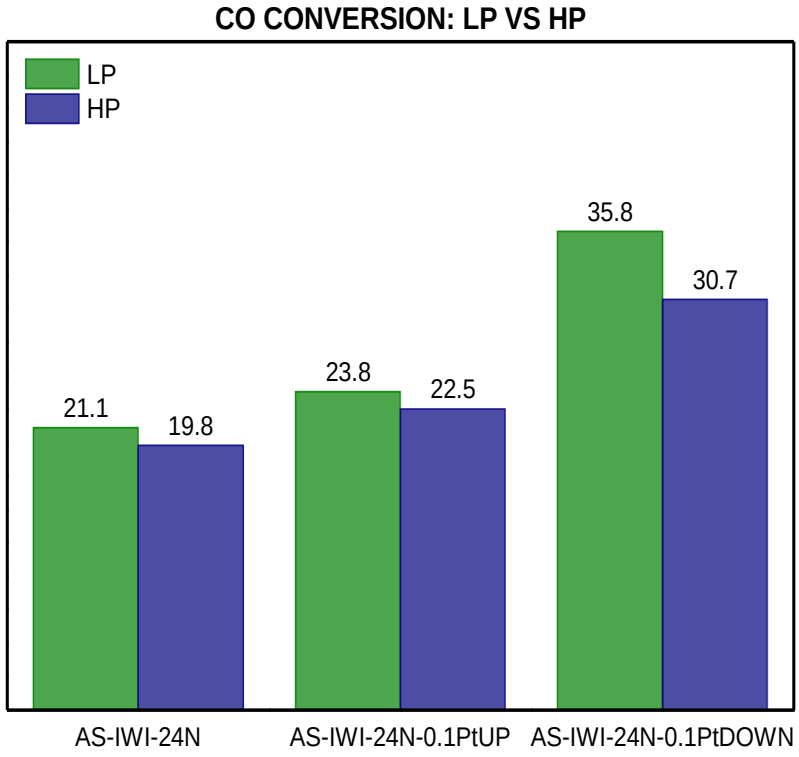

Figure 5.11: CO conversion at LP and HP for conventional catalysts [17]

Two are the plausible explanations for the quantitative relationship between the results obtained at LP and HP. The first ascribes this behavior to the importance of methanation reaction in the LP experiments. It is suggested that the high activity towards methane formation might compensate the FT activity loss due to low pressure operation. Methanation consumes CO in parallel with the CO consumed by the FT reaction [25]; this results in an overall higher conversion, which unfortunately cannot be directly associated to a high FT activity.

The second explanation is based on the different selectivities obtained on the two rigs. While light gaseous hydrocarbons are typically formed at LP, on the HP rig the main products obtained are long chain hydrocarbons (waxes) in liquid phase at process conditions. As gas diffusivities are higher, by some orders of magnitude, to liquid diffusivities, it is reasonable to assume the absence of intraparticle diffusion limitations in the LP experiments, which ensures higher reactant availability to the active site.

Anyways, regardless of the quantitative results, the first goal of this investigation is to find, at least, a qualitative activity relationship between the two processes. The same relative activity order, at LP

and HP, obtained for the three catalysts shown in Figure 5.11, corroborates the efficacy of the LP catalyst screening prior to the HP tests. However, for what concerns product selectivities the higher complexity of the reaction environment at high pressure does not allow any valuable comparison between the two processes [17].

5.4.3 Experimental results

The activity results of the LP tests for the catalysts studied in this chapter are recapped in Figure 5.12, where they are compared with the experimental data collected on the HP rig. Data at HP for AS-IWI-24N and AS-IWI-24N-0.5GL are taken from *Fratalocchi et al.* [18], whereas data at HP for the Pt-promoted catalysts (AS-IWI-24N-0.5GL-0.1PtUP and AS-IWI-24N-0.5GL-0.1PtDOWN) are taken from a recent thesis work [16].

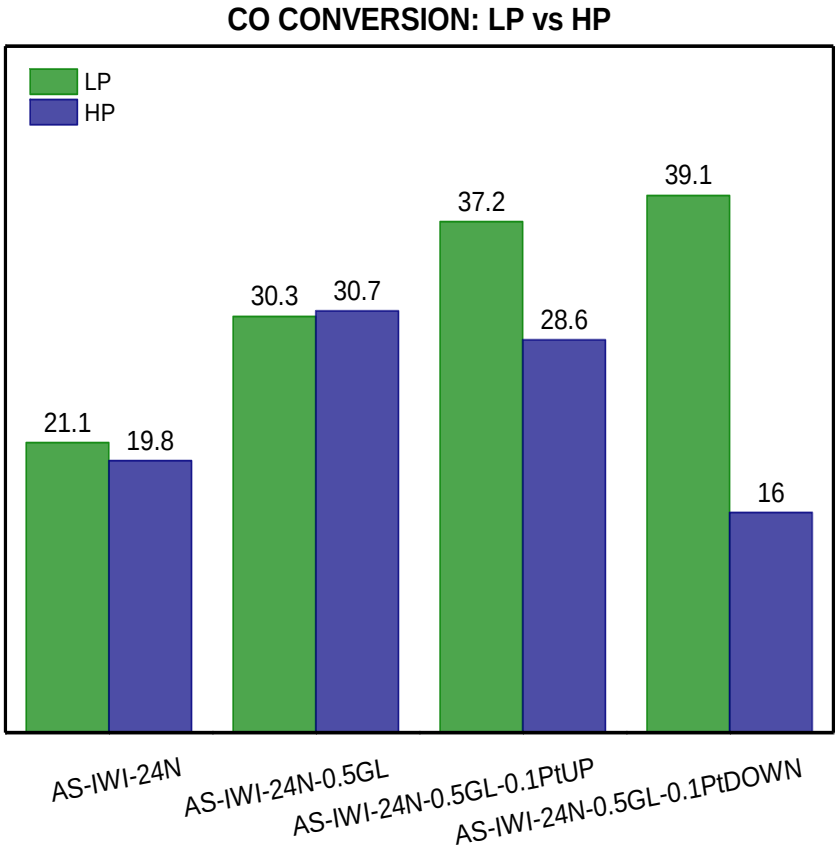

Figure 5.12: CO conversion for unconventional catalysts tested at LP and HP

Also at industrially relevant FT conditions the unpromoted DEG-catalyst shows better performances than the conventional catalyst. Despite a more difficult reduction, the higher dispersion in the DEG-catalyst brought the most beneficial effect, leaving a more active catalyst. The reason for the lower activity at HP of the conventional catalyst can be ascribed to its large Co^0 crystallite diameter, that is about 14 [nm], about twice the one of the DEG-catalyst (Table 5.3). Such high crystallite diameters, well above the optimal range 8 ÷ 10 [nm] found at HP [8, 26], mark a low degree of dispersion of the active phase, which in turn prejudices catalyst activity. As already underlined in the comparison of performances at LP, it is now corroborated at HP that, despite a poor reducibility, the higher degree of dispersion makes the unpromoted DEG-catalyst more active than the corresponding conventional catalyst.

When it comes to Pt promotion of the DEG-catalyst, the trend is no more respected between LP and HP tests. If tests at atmospheric pressure reflected the beneficial effects of Pt-promotion on DEG-catalysts both on dispersion and reducibility, with activities in the order *NoPt* < *PtUP* < *PtDOWN*, when tested at industrially relevant FT conditions the order is reversed, with the *PtDOWN* catalyst being by far the least active.

This reversed trend can be ascribed to differences in Co^0 particle size (Table 5.5) between the unpromoted and the Pt-promoted catalysts and to different operating conditions for the experiments (25 [bar] vs atmospheric pressure). While the unpromoted DEG-catalyst displays an average Co^0 crystallite diameter (9 [nm]) close to the optimal range observed in the literature [8, 26] at conditions favoring the chain growth (C_{5+} selectivity > 80%), the values found for the *PtUP* (6.4 [nm]) and the *PtDOWN* catalyst (5.4 [nm]) are both below. In particular, the latter shows a dramatic activity loss, in agreement with its very small Co^0 crystallite size: 16% carbon monoxide conversion against 30.7% observed with the DEG-catalyst. Henceforth, Co^0 particle size is confirmed as the main reason for the different trends observed at atmospheric pressure and at industrially relevant FT condition.

To summarize, on the one hand the activity results obtained at LP for conventional catalysts were corroborated at HP [17], on the other hand significant discrepancies were observed in our investigation on well-dispersed catalysts. Therefore, we can state that LP catalytic testing is a useful and time-saving screening tool whose results, however, have to be examined very carefully. In fact, promising performances observed at LP may not always end up in highly active catalysts at real Fischer-Tropsch conditions.

Bibliography Chapter 5

[1] E. Iglesia, "Design, synthesis, and use of cobalt-based Fischer-Tropsch synthesis catalysts," *Appl. Catal. A Gen.*, vol. 161, pp. 59–78, 1997.

[2] M. De Beer, A. Kunene, D. Nabaho, M. Claeys, and E. Van Steen, "Technical and economic aspects of promotion of cobalt-based Fischer-Tropsch catalysts by noble metals – a review," vol. 114, no. October 2013, pp. 14–16, 2014.

[3] A. Y. Khodakov, W. Chu, and P. Fongarland, "Advances in the development of novel cobalt Fischer-Tropsch catalysts for synthesis of long-chain hydrocarbons and clean fuels," *Chem. Rev.*, vol. 107, no. 5, pp. 1692–1744, 2007.

[4] L. Shi, Y. Jin, C. Xing, C. Zeng, T. Kawabata, K. Imai, K. Matsuda, Y. Tan, and N. Tsubaki, "Studies on surface impregnation combustion method to prepare supported Co/SiO 2 catalysts and its application for Fischer-Tropsch synthesis," *Appl. Catal. A Gen.*, vol. 435–436, pp. 217–224, 2012.

[5] A. Feller, M. Claeys, and E. van Steen, "Cobalt Cluster Effects in Zirconium Promoted Co/SiO2 Fischer–Tropsch Catalysts," *J. Catal.*, vol. 185, no. 1, pp. 120–130, 1999.

[6] S. Stors??ter, B. T??tdal, J. C. Walmsley, B. S. Tanem, and A. Holmen, "Characterization of alumina-, silica-, and titania-supported cobalt Fischer-Tropsch catalysts," *J. Catal.*, vol. 236, no. 1, pp. 139–152, 2005.

[7] J. P. den Breejen, J. R. A. Sietsma, H. Friedrich, J. H. Bitter, and K. P. de Jong, "Design of supported cobalt catalysts with maximum activity for the Fischer-Tropsch synthesis," *J. Catal.*, vol. 270, no. 1, pp. 146–152, 2010.

[8] G. L. Bezemer, J. H. Bitter, H. P. C. E. Kuipers, H. Oosterbeek, J. E. Holewijn, X. Xu, F. Kapteijn, a J. Van Dillen, and K. P. De Jong, "Cobalt Particle Size Effects in the Fischer − Tropsch Reaction Studied with Carbon Nanofiber Supported Catalysts," *Am. Chem. Soc.*, vol. 128, no. 12, pp. 3956–3964, 2006.

[9] X. Guo, D. Mao, G. Lu, S. Wang, and G. Wu, "Glycine-nitrate combustion synthesis of CuO-ZnO-ZrO2 catalysts for methanol synthesis from CO2 hydrogenation," *J. Catal.*, vol. 271, no. 2, pp. 178–185, 2010.

[10] G. Kishan, L. Coulier, V. H. J. de Beer, J. a. R. van Veen, and J. W. Niemantsverdriet, "Preparation of highly active NiW hydrotreating model catalysts with 1,2-

cyclohexanediamine-N,N,N′N′-tetraacetic acid (CyDTA) as a chelating agent," *R. Soc. Chem.*, no. 13, pp. 1103–1104, 2000.

[11] S. L. Gonzàlez-Cortés, T. C. Xiao, S. M. A. Rodulfo-Baechler, and M. L. H. Green, "Impact of the urea-matrix combustion method on the HDS performance of Ni-MoS2/??-Al2O3 catalysts," *J. Mol. Catal. A Chem.*, vol. 240, no. 1–2, pp. 214–225, 2005.

[12] N. Koizumi, Y. Ibi, D. Hongo, Y. Hamabe, S. Suzuki, Y. Hayasaka, T. Shindo, and M. Yamada, "Mechanistic aspects of the role of chelating agents in enhancing Fischer-Tropsch synthesis activity of Co/SiO 2 catalyst: Importance of specific interaction of Co with chelate complex during calcination," *J. Catal.*, vol. 289, pp. 151–163, 2012.

[13] S. Ho, "Effects of Ethanol Impregnation on the Properties of Thoria-Promoted Co / SiO 2 Catalyst," *J. Catal.*, vol. 168, pp. 51–59, 1997.

[14] L. A. Richard, P. Moreau, S. Rugmini, and F. Daly, "Fischer-Tropsch performance correlated to catalyst structure: Trends in activity and stability for a silica-supported cobalt catalyst," *Appl. Catal. A Gen.*, vol. 464–465, pp. 200–206, 2013.

[15] N. Koizumi, Y. Hayasaka, Y. Ibi, S. Suzuki, T. Shindo, and M. Yamada, "Enhancing the fischer-tropsch synthesis activity of co-based catalysts by adding ZrO x to the SiO2 support and chelating ligands to the co-precursor," *Catal. Letters*, vol. 141, no. 8, pp. 1207–1214, 2011.

[16] S. Perfetti and G. Zanchi, "Analisi di reattività di catalizzatori Co/γ – Al2O3 attivi nella sintesi di Fischer-Tropsch," Master Thesis, Politecnico di Milano, 2016.

[17] L. Pirovano and A. Quarantotto, "Studio dell'effetto dell'ordine di deposizione del promotore nella sintesi di catalizzatori Fischer - Tropsch Co/γ-Al2O3 e validità dei test di screening di attività condotti a bassa pressione," Master Thesis, Politecnico di Milano, 2015.

[18] L. Fratalocchi, C. G. Visconti, L. Lietti, N. Fischer, and M. Claeys, "Tailoring the properties of a cobalt based Fischer Tropsch catalyst supported on stabilized γ-Al2O3 through the addition of diethylene glycol in the Co-impregnating solution," *Press*, 2016.

[19] J. S. Girardon, A. S. Lermontov, L. Gengembre, P. A. Chernavskii, A. Griboval-Constant, and A. Y. Khodakov, "Effect of cobalt precursor and pretreatment conditions on the structure and catalytic performance of cobalt silica-supported Fischer-Tropsch catalysts," *J. Catal.*, vol. 230, no. 2, pp. 339–352, 2005.

[20] F. Diehl and A. Y. Khodakov, "Promotion of Cobalt Fischer-Tropsch Catalysts with Noble Metals: a Review," *Oil Gas Sci. Technol. …*, vol. 64, no. 1, pp. 11–24, 2009.

[21] D. Nabaho, J. W. Niemantsverdriet, M. Claeys, and E. Van Steen, "Hydrogen spillover in the Fischer-Tropsch synthesis: An analysis of platinum as a promoter for cobalt-alumina catalysts," *Catal. Today*, vol. 261, pp. 17–27, 2016.

[22] A. Y. Khodakov, J. Lynch, D. Bazin, B. Rebours, N. Zanier, B. Moisson, and P. Chaumette, "Reducibility of cobalt species in silica-supported FT catalysts," *J. Catal.*, vol. 168, pp. 16–25, 1997.

[23] Z. Zsoldos, T. Hoffer, and L. Guczi, "Structure and catalytic activity of alumina-supported platinum-cobalt bimetallic catalysts. 1. Characterization by x-ray photoelectron spectroscopy," *J. Phys. Chem.*, vol. 95, no. 2, pp. 798–801, 1991.

[24] W. Chu, P. A. Chernavskii, L. Gengembre, G. A. Pankina, P. Fongarland, and A. Y. Khodakov, "Cobalt species in promoted cobalt alumina-supported Fischer-Tropsch catalysts," *J. Catal.*, vol. 252, no. 2, pp. 215–230, 2007.

[25] W. Ma, G. Jacobs, R. Keogh, C. H. Yen, J. L. S. Klettlinger, and B. H. Davis, "Fischer-Tropsch synthesis: Effect of Pt promoter on activity, selectivities to hydrocarbons and oxygenates, and kinetic parameters over 15%Co/Al 2O3," *ACS Symp. Ser.*, vol. 1084, pp. 127–153, 2011.

[26] N. Fischer, E. Van Steen, and M. Claeys, "Structure sensitivity of the Fischer-Tropsch activity and selectivity on alumina supported cobalt catalysts," *J. Catal.*, vol. 299, no. March, pp. 67–80, 2013.

Conclusions

Experiments carried out on 0.1 wt.% Pt-promoted cobalt based catalysts provided valuable information on the effect of noble metal deposition order in morphological properties, reducibility and activity of Fischer-Tropsch catalysts.

Platinum promotion, regardless of its deposition order, favored reducibility as shown by the temperatures of the reduction peaks shifted towards lower values than those observed with the unpromoted catalysts. Characterization and testing showed that Pt, deposited directly on the stabilized support (*PtDOWN*), brings the most beneficial effects: the enhanced H_2 spillover mechanism, via surface migration, improved the reducibility of the smallest and strongly support-interacting CoO particles thus increasing the number of active sites on the catalyst surface and, consequently, the activity.

The effect of Pt deposition order was further investigated in catalysts prepared with different cobalt loadings (12, 18, 24 wt.%). Interestingly, the same trends were observed regardless of the quantity of active phase: Pt deposited as the last stage favored the first reduction step, from Co_3O_4 to CoO, while the second step ($CoO \rightarrow Co^0$) occurs readily when Pt is directly deposited on the support. One the one hand, it is suggested that in the *PtUP* configuration the noble metal is more exposed to the hydrogen flux, thus facilitating its dissociation (i.e. the slow step of the reduction); on the other hand, when the promoter is deposited directly on the support, the intimate contact between the latter and the noble metal favors hydrogen mobility via surface migration, thus facilitating the second step to occur.

As a proper Co^0 dispersion is crucial for the activity of Fischer-Tropsch catalysts, unconventional catalysts were prepared aiming at this objective. The addition of diethylene glycol (DEG) to the impregnating solution turned the calcination process from endothermic, as it was for conventional catalysts, to exothermic, thus spreading the cobalt particles on the catalyst support. The higher Co^0 dispersion prevailed on the more difficult reducibility of the small Co_3O_4 particles thus leading to a more active catalyst.

Platinum promotion was also studied for unconventional catalysts (DEG-catalysts). Even on such highly dispersed systems the addition of small amounts of noble metal showed beneficial effects,

both in terms of reducibility and activity. The same trend regarding Pt deposition order as in conventional catalysts was observed: the first peak occurred readily in the PtUP configuration while *PtDOWN* favored the second reduction step.

As a consequence of the improved reducibility, Pt promotion shifted the Co^0 crystallite size distribution towards smaller values, thus resulting in enhanced catalytic performances at ambient pressure (LP). However, when tested at real Fischer-Tropsch conditions (HP) the same Pt-promoted catalysts showed a considerable activity loss, when compared to the unpromoted DEG-catalyst. This discrepancy was ascribed to the different optimal range of Co^0 particle diameters for catalyst activity at LP and at HP. In particular, the very small crystallites observed for the Pt-promoted DEG-catalysts have dimensions close to the LP optimal size (6 [nm]), which is shifted to higher values at HP (8-10 [nm]). This explained the discrepancies in activity observed in our investigation on well-dispersed catalysts.

Consequently, LP catalyst testing holds its validity as a time-saving screening tool whose outcomes, however, have to be prudently inspected. In fact, promising performances observed at LP may not always end up in highly active catalysts at industrially relevant Fischer-Tropsch conditions.